Evaluating NO_x Fate and Organic Nitrate Chemistry from α-Pinene Oxidation Using Stable Oxygen and Nitrogen Isotopes~~Evaluating Nitrogen Oxide and α-pinene Oxidation Chemistry: Insights from Oxygen and Nitrogen Stable Isotopes~~

Wendell W. Walters[1,2], Masayuki Takeuchi[3,a], Danielle E. Blum[4], Gamze Eris[5], David Tanner[6], Weiqi Xu[5,7], Jean Rivera-Rios[5,b], Fobang Liu[5,8], Tianchang Xu[5], Greg Huey[6], Justin B. Min[6], Rodney Weber[6], Nga L. Ng [3,5,6], and Meredith G. Hastings[2,9]

[1]Department of Chemistry and Biochemistry, University of South Carolina, 631 Sumter St, Columbia, SC 29208, USA
[2]Institute at Brown for Environment and Society, Brown University, 85 Waterman St, Providence, RI 02912, USA
[3]School of Civil and Environmental Engineering, Georgia Institute of Technology, 311 Ferst Drive NW, Atlanta, GA 30332, USA
[4]Department of Chemistry, Brown University, 324 Brook Street, Providence, RI 02912, USA
[5]School of Chemical and Biomolecular Engineering, Georgia Institute of Technology, 311 Ferst Drive NW, Atlanta, GA 30332, USA
[6]School of Earth and Atmospheric Sciences, Georgia Institute of Technology, 311 Ferst Drive NW, Atlanta, GA 30332, USA
[7]State Key Laboratory of Atmospheric Boundary Layer Physics and Atmospheric Chemistry, Institute of Atmospheric Physics, Chinese Academy of Sciences, Beijing, 100029, China
[8]Department of Environmental Science and Engineering, Xi'an Jiaotong University, Xi'an, Shaanxi, 710049, China
[9]Department of Earth, Environmental, and Planetary Sciences, Brown University, 324 Brook Street, Box 1846, Providence, RI 02912, USA

Correspondence to: Wendell W. Walters (wendellw@mailbox.sc.edu)

[a]Now at Department of Mechanical Engineering, University of Colorado Boulder, 1111 Engineering Dr, Boulder, CO, 80309, USA
[b]Now at Department of Chemistry and Chemical Biology, Rutgers University, 123 Bevier Rd, Piscataway, NJ, 08854, USA

Abstract. The oxidation of biogenic volatile organic compounds (BVOCs) such as α-pinene in the presence of nitrogen oxides (NO_x = NO + NO_2) initiates complex photochemical processes that produce organic nitrates ($RONO_2$) and influence atmospheric oxidation capacity, air quality, and the fate of reactive nitrogen. However, tracking the chemical fate of $RONO_2$ remains challenging as it includes pathways such as renoxification, aerosol partitioning, deposition, and/or hydrolysis to nitric acid (HNO_3). Stable oxygen ($\Delta^{17}O$, $\delta^{18}O$) and nitrogen ($\delta^{15}N$) isotope measurements can provide a unique tool to probe these processes, as NO_y species can exhibit distinct isotopic signatures due to characteristic oxygen-transfer dynamics and isotope fractionation. Here, we present chamber experiments of α-pinene oxidation in the presence of NO_x under a range of oxidant and photochemical conditions, reporting the $\Delta^{17}O$, $\delta^{18}O$, and $\delta^{15}N$ values of simultaneously collected NO_2, HNO_3, and particulate nitrate (pNO_3), the latter of which derived predominantly from $RONO_2$ in the conducted experiments. A strong linear relationship between $\delta^{18}O$ and $\Delta^{17}O$ across all NO_y species (r = 0.992; p < 0.01) supports a two-endmember mixing

model, in which oxygen atoms are transferred from isotopically distinct sources that include ozone (O_3) with high $\delta^{18}O/\Delta^{17}O$ and peroxy/hydroxyl radicals ($RO_2/HO_2/OH$) with lower values. Nitrogen isotope fractionation, quantified as the difference in $\delta^{15}N$ values ($\Delta\delta^{15}N$), revealed consistently positive $\Delta\delta^{15}N(HNO_3 - NO_2)$ values (+28.9 ± 13.4 ‰ in daytime experiments; +22.2 ± 1.4 ‰ at night) and negative $\Delta\delta^{15}N(pNO_3\text{-}NO_2)$ values (–13.6 ± 5.8 ‰ in daytime experiments). This reflected distinct formation pathways and isotope effects including NO_x photochemical cycling, thermal dinitrogen pentoxide (N_2O_5)–nitrate radical (NO_3)–NO_2 equilibrium, and HNO_3 production mechanisms. Box model simulations based on $\Delta^{17}O$ values as a constraint were conducted using a newly developed gas-phase mechanism, which reproduced $\Delta^{17}O(NO_2)$ and $\Delta^{17}O(pNO_3)$ (compared to simulated $\Delta^{17}O(RONO_2)$) accurately, with an average model bias of 0.9 ± 2.4 ‰ (R^2 = 0.98) and -1.4 ±2.4 ‰ (R^2 = 0.55 and R^2 = 0.97 when excluding one outlier), respectively. We further empirically derived important isotopic parameters such as the $\Delta^{17}O$ value transferred from O_3 through comparison of model-simulated oxygen atom source contributions with observed $\Delta^{17}O$ values for NO_2 and pNO_3 across experiments. This yielded best-fit slopes of 39.4 ± 0.6 ‰ for NO_x photochemical cycling and 41.7 ± 1.2 ‰ for $RONO_2$ formation, consistent with near-surface observations of $\Delta^{17}O$ in the terminal oxygen atom of O_3. Despite the agreement with NO_2 and $RONO_2$, accurately simulating $\Delta^{17}O(HNO_3)$ proved challenging. Sensitivity tests revealed that model biases likely stemmed from a combination of factors including background HNO_3 chamber blanks affecting low-NO_x experiments, missing N_2O_5 heterogeneous hydrolysis under nighttime conditions, and an overestimation in the $\Delta^{17}O(HNO_3)$ mass balance resulting from the NO_2 + OH reaction, which was improved by adjusting the contribution from $(2/3)\Delta^{17}O(NO_2)$ to $(1/2)\Delta^{17}O(NO_2)$. These adjustments reduced the average model bias in $\Delta^{17}O(HNO_3)$ from 6.7 ± 3.3 ‰ (R^2 = 0.39) in the base mechanism to 1.6 ± 1.3 ‰ (R^2 = 0.48) in the modified mechanism. These findings demonstrate the utility of $\Delta^{17}O$ and $\delta^{15}N$ for disentangling nitrate formation mechanisms, while also highlighting critical gaps in our understanding of the isotope dynamics involving HNO_3 formation. Future experimental work targeting isolated HNO_3 pathways is essential to refine isotopic mass-balance assumptions and nitrogen isotope fractionation.~~The chemical interaction between nitrogen oxides (NO_x = NO + NO_2) and α-pinene plays a critical role in air quality and climate. However, uncertainties remain regarding their coupling in NO_x loss, renoxification, and oxidation chemistry. To address these gaps, we conducted controlled chamber experiments, analyzing nitric acid (HNO_3), NO_3, and particulate nitrate (pNO_3) for their oxygen and nitrogen stable isotope variations ($\Delta^{17}O$, $\delta^{18}O$, and $\delta^{15}N$). A strong linear relationship between $\delta^{18}O$ and $\Delta^{17}O$ across experiments revealed contributions of oxygen from ozone (O_3) and atmospheric oxygen (O_2) in forming reactive radicals. The $\delta^{15}N$ values followed the order $\delta^{15}N(pNO_3) < NO_2 < HNO_3$, reflecting isotope fractionation during NO_x oxidation. A new chemical mechanism accurately predicted aerosol precursor decay and simulated $\Delta^{17}O$ and $\delta^{15}N$ values. Simulations showed NO_x–photochemical cycling and pNO_3 formation, primarily from organic nitrate, with $\Delta^{17}O(NO_2)$ simulations achieving a root mean square error (RMSE) of 1.7 ‰. Improved $\delta^{15}N(NO_2)$ and pNO_3 simulations used a nitrogen isotope fractionation factor ($^{15}\alpha$) of 0.997 for NO_2 + OH reactions. However, modeling $\Delta^{17}O$ and $\delta^{15}N$ of HNO_3 proved challenging, likely due to sampling artifacts. This study provides insights into $\Delta^{17}O$ transfer dynamics, nitrogen isotope fractionation, and the role of NO_x–BVOC chemistry in air quality, highlighting the potential of $\Delta^{17}O$ and $\delta^{15}N$ as tools for evaluating complex atmospheric processes.~~

1 ~~I~~Introduction

The oxidation of biogenic volatile organic compounds (BVOCs) in the presence of nitrogen oxides (NO_x = NO + NO_2) plays a central role in atmospheric chemistry, linking anthropogenic emissions to the formation of ozone (O_3), secondary organic aerosols (SOA), and the cycling of reactive nitrogen (Hoyle et al., 2011; Ng et al., 2017; Romer et al., 2016; Sato et al., 2022; Takeuchi and Ng, 2019; Xu et al., 2015b, 2020; Zare et al., 2018). A key product of this interaction is organic nitrate ($RONO_2$), which can be produced both during daytime and nighttime oxidation reactions involving monoterpenes (Ng et al., 2017). The $RONO_2$ product can act either as a temporary NO_x reservoir or a permanent sink, depending on its atmospheric fate (Fisher et al., 2016).~~(Alexander et al., 2020)~~ Once formed, gas-phase $RONO_2$ can either photolyze or oxidize, leading to the release of NO_x ("renoxification"), partition into the particle phase, resulting in particulate $RONO_2$ ($pRONO_2$) (Beaver et al., 2012; Browne et al., 2014; Browne and Cohen, 2012; Fisher et al., 2016; Wang et al., 2023), and/or undergo dry and wet deposition, leading to the removal of reactive nitrogen from the atmosphere. Hydrolysis has emerged as an important pathway that directly converts $RONO_2$ into HNO_3, which acts as a permanent sink of NO_x, but the efficiency of this process remains challenging to constrain. Model investigations have suggested a lifetime of $RONO_2$ with respect to hydrolysis on the order of a few hours (Fisher et al., 2016; Zare et al., 2018). Experimental measurements have indicated a complex picture, in which not all monoterpene-derived $RONO_2$ hydrolyze, and that the lifetime of α-pinene derived $RONO_2$ due to hydrolysis ranges on the order of minutes to hours and even days (Rindelaub et al., 2015; Takeuchi and Ng, 2019; Wang et al., 2021). ~~(Romer et al., 2016; Takeuchi and Ng, 2019)(Day et al., 2010; Rindelaub et al., 2016; Takeuchi and Ng, 2019; Wang et al., 2021; Zare et al., 2018)~~Due to these complexities, the contributions of $RONO_2$ to HNO_3 and particulate nitrate (pNO_3) budgets remain poorly constrained. These uncertainties hinder our ability to predict NO_x lifetime and oxidant budgets, particularly in regions where high BVOC emissions coincide with anthropogenic NO_x such as forested areas near urban locations. Here, we develop new tools aimed at tracking $RONO_2$ contributions to HNO_3 and pNO_3 budgets using stable isotope measurements ($\Delta^{17}O$, $\delta^{18}O$, $\delta^{15}N$) in controlled α-pinene + NO_x chamber experiments, providing mechanistic insights into $RONO_2$ formation and loss pathways.~~The oxidation of biogenic volatile organic compounds (BVOCs) in the presence of nitrogen oxides (NO_x = NO + NO_2) constitutes an important mechanism of coupled biogenic-anthropogenic interactions. This interplay bears significant consequences for air quality, climate, global reactive nitrogen budget, and secondary organic aerosols (SOA) (Hoyle et al., 2011; Ng et al., 2017; Romer et al., 2016; Sato et al., 2022; Takeuchi and Ng, 2019; Xu et al., 2015b, 2020; Zare et al., 2018). Monoterpenes ($C_{10}H_{16}$) are a major class of BVOCs that, upon oxidation, can lead to significant organic nitrate and SOA formation both during daytime and nighttime (Aschmann et al., 2002; Bates et al., 2022; Bell et al., 2022; Fry et al., 2014;~~

~~Hallquist et al., 1999; Nah et al., 2016; Nozière et al., 1999; Rindelaub et al., 2015). (Beaver et al., 2012; Fisher et al., 2016; Fry et al., 2014; Wang et al., 2023)(Fisher et al., 2016; Zare et al., 2018)(Rindelaub et al., 2016; Takeuchi and Ng, 2019)~~

~~However, significant gaps exist in our comprehension of monoterpene and NO_x coupled chemistry, including the fate of organic nitrogen and its influence on NO_x and oxidant budgets. Once formed, gas-phase organic nitrogen can either photolyze or oxidize, leading to the release of NO_x ("renoxification"), partition into the particle phase, resulting in particulate organic nitrogen production (Beaver et al., 2012; Browne et al., 2014; Browne and Cohen, 2012; Fisher et al., 2016; Wang et al., 2023), and/or undergo dry and wet deposition, leading to the removal of reactive nitrogen from the atmosphere. An important loss process for organic nitrate is hydrolysis in the particle phase, leading to the production of nitric acid (HNO_3) (Day et al., 2010; Rindelaub et al., 2016; Russell et al., 2011; Takeuchi and Ng, 2019; Wang et al., 2021; Zare et al., 2018). Understanding the fates of organic nitrogen and the feedback in oxidation chemistry arising from BVOC/NO_x interactions is critical for accurately assessing their roles in NO_x loss and recycling, O_3 formation, and SOA generation.~~

~~To address these fundamental uncertainties and advance our understanding, it is imperative to employ methodologies that can be used to deduce the reaction mechanisms governing the formation and fate of organic nitrogen.~~ The natural variations of stable oxygen and nitrogen isotopes in various reactive nitrogen (NO_y = NO_x + HNO_3 + ~~alkyl nitrate (~~$RONO_2$~~)~~ + peroxy nitrate (RO_2NO_2) + etc.) molecules offer a powerful diagnostic tool to investigate NO_x and oxidation chemistry~~may be a promising analytical tool to enhance our insight into the intricate connections between NO_x and BVOC chemistry and their implications for atmospheric composition~~ (Michalski et al., 2012; Walters et al., 2018). ~~Stable isotope approaches offer novel avenues to probe and refine our understanding of complex atmospheric processes, unravel the dynamics of BVOC/NO_x interactions, and ultimately contribute to formulating informed air quality management strategies.~~ Stable isotope constraints may also serve as quantitative tracers to distinguish daytime (e.g., RO_2 + NO) versus nighttime (e.g., NO_3 + BVOC) $RONO_2$ production, quantify the extent of $RONO_2$ hydrolysis to HNO_3, and constrain the relative contributions of organic versus inorganic pathways to the pNO_3 budget.

Variations in oxygen (O) isotope ratios (i.e., $^{18}O/^{16}O$ and $^{17}O/^{16}O$), commonly quantified using isotope delta notation ($\Delta^{17}O$ and $\delta^{18}O$), offer a powerful proxy for assessing oxidation pathways involving NO_x photochemical cycling and nitrate formation (Albertin et al., 2021; Alexander et al., 2020; Michalski et al., 2003; Morin et al., 2011; Walters et al., 2024b). This is owing to distinct $\Delta^{17}O$ and $\delta^{18}O$ values exhibited by key atmospheric oxidants, which are proportionally transferred to NO_x during oxidation in the atmosphere (Hastings et al., 2003; Michalski et al., 2003). For instance, tropospheric O_3 has an elevated $\Delta^{17}O$ with a mean value near 26 ‰, and the transferable terminal oxygen atom of O_3 (O_3^{term}) exhibiting a $\Delta^{17}O$ of 39~~.3~~ ± 2 ‰ and elevated $\delta^{18}O$ near 126 ± 12 ‰ based on recent near-surface observations (Ishino et al., 2017; Vicars and Savarino, 2014). In contrast, other atmospheric oxidants such as RO_2/HO_2 and OH have $\Delta^{17}O$ values assumed to be ~~at or~~ near 0 ‰ (Lyons, 2001;

Walters et al., 2024a). The $\delta^{18}O$ values of RO_2/HO_2 and OH have not been directly determined but are anticipated to be lower than the $\delta^{18}O(O_3^{term})$ (Michalski et al., 2012).

~~The $\Delta^{17}O$ isotopic differences provide quantitative measures to evaluate NO_x photochemical cycling and nitrate formation processes. Notably, $\Delta^{17}O$ has been frequently utilized to assess atmospheric nitrate formation pathways, as different pathways yield distinct $\Delta^{17}O$ values based on oxygen isotope mass balance assumptions (Alexander et al., 2020; Michalski et al., 2003; Morin et al., 2011; Walters et al., 2024b). More recent advancements include the first reliable *in situ* measurements of $\delta^{18}O(NO_2)$ and $\Delta^{17}O(NO_2)$, which enable an evaluation of NO_2 formation pathways (i.e., $NO + O_3$ vs $NO + RO_2/HO_2$) (Albertin et al., 2021; Walters et al., 2018, 2024b). Further, we have recently developed a chemical mechanism that can explicitly model $\Delta^{17}O$ of numerous NO_y components, termed InCorporating Oxygen Isotopes of Oxidized Reactive Nitrogen (ICOIN) based on the Regional Atmospheric Chemistry Mechanism, Version 2 mechanism (RACM2) (Walters et al., 2024a). These new tools offer exciting opportunities for probing NO oxidation branching ratios, assessing organic nitrogen yields from $NO + RO_2$ reactions under various NO_x/BVOC conditions, and evaluating nitric acid formation mechanisms including both inorganic and organic reaction pathways.~~ The $\Delta^{17}O$ isotopic composition provides a quantitative framework to evaluate NO_x photochemical cycling and the formation pathways of nitrate-containing species. This tracer has been widely used to assess NO_x oxidation and secondary product formation, as different atmospheric reactions impart distinct $\Delta^{17}O$ signatures based on mass-balance relationships (Alexander et al., 2020; Michalski et al., 2003; Morin et al., 2011; Walters et al., 2024b) (Table 1). For instance, mass-balance calculations predict that $\Delta^{17}O$ should differ between HNO_3 produced via the daytime NO_2 + OH reaction and that derived from the hydrolysis of daytime formed $RONO_2$, where the $\Delta^{17}O$ of the nitrooxy ($-NO_3$) functional group reflects a combination of NO + RO_2 oxidation. These differences make $\Delta^{17}O$ a potentially powerful diagnostic tool for quantifying $RONO_2$ contributions to HNO_3 formation. Moreover, substantial $\Delta^{17}O$ differences are expected between $RONO_2$ formed through daytime RO_2 + NO reactions and those formed via nighttime NO_3 + BVOC reactions. Thus, $\Delta^{17}O$ could also be a useful tool for distinguishing between daytime and nighttime formation pathways of $RONO_2$, potentially aiding in our ability to accurately predict the atmospheric burden of $RONO_2$. Despite major advances in applying $\Delta^{17}O$ to constrain atmospheric nitrogen oxidation chemistry, a significant limitation remains: most $\Delta^{17}O$ pathway estimates rely on theoretical mass-balance assumptions that have only been empirically validated for a limited number of reactions (e.g., $NO + O_3$ and $NO_2 + O_3$) (Berhanu et al., 2012; Savarino et al., 2008). Further, we have yet to have measured the $\Delta^{17}O$ of $RONO_2$ directly. Expanding direct $\Delta^{17}O$ measurements of key NO_y compounds under various oxidant conditions is critical for testing these assumptions.

Table 1. Expected $\Delta^{17}O$ values for reactive nitrogen species formed via different oxidation pathways based on oxygen isotope mass-balance. Each pathway is expressed as a weighted average of the $\Delta^{17}O$ values of precursor oxidants, based on the proposed reaction mechanism. Species include NO_2, HNO_3, and $RONO_2$.

Formation Pathway	Expected $\Delta^{17}O$
NO_2	

$NO_3 + O_3$[a]	1/2 ($\Delta^{17}O(NO)$) + 1/2 ($\Delta^{17}O(O_3^{term})$)
$NO + RO_2$[b]	1/2($\Delta^{17}O(NO)$) + 1/2 ($\Delta^{17}O(RO_2)$)
$NO + HO_2$[c]	1/2 ($\Delta^{17}O(NO)$) + 1/2($\Delta^{17}O(HO_2)$)
HNO_3	
$NO_2 + OH$	2/3($\Delta^{17}O(NO_2)$) + 1/3($\Delta^{17}O(OH)$)
$NO_3 + HC$[d]	$\Delta^{17}O(NO_3)$
$NO + HO_2$[b]	1/3($\Delta^{17}O(NO)$)+2/3($\Delta^{17}O(HO_2)$)
$N_2O_5 + H_2O$ (aq)	5/6($\Delta^{17}O(N_2O_5)$)+1/6($\Delta^{17}O(H_2O)$)
$N_2O_5 + Cl^-$ (aq)	5/6($\Delta^{17}O(N_2O_5)$)+1/6($\Delta^{17}O(O_3^{term})$)
$NO_2 + H_2O$ (aq)	2/3($\Delta^{17}O(NO_2)$) + 1/3($\Delta^{17}O(H_2O)$)
$NO_3 + H_2O$ (aq)	$\Delta^{17}O(NO_3)$
$RONO_2 + H_2O$ (aq)	$\Delta^{17}O(RONO_2)$)
$RONO_2^{*-}$	
$NO + RO_2$[b]	1/3($\Delta^{17}O(NO)$)+2/3($\Delta^{17}O(RO_2)$)
$NO_3 + BVOC$	$\Delta^{17}O(NO_3)$

[a]O_3^{term} = terminal oxygen in ozone

[b]RO_2 = organic peroxy radical

[c]HO_2 = hydroperoxyl radical

[d]HC = hydrocarbon

*$\Delta^{17}O$ calculated from the nitrooxy (-NO_3) functional group.

The stable nitrogen (N) isotope ratio variations ($\delta^{15}N$) of NO_x and atmospheric nitrate have ~~conventionally~~ long served as a valuable proxy for evaluating precursor emission sources, because of the preserved N mass between the precursor and oxidized end-products (Elliott et al., 2019; Hastings et al., 2013). However, it is essential to consider that NO_x photochemical cycling and atmospheric nitrate formation processes can also induce significant mass-dependent fractionation effects (Freyer et al., 1993; Li et al., 2020; Walters et al., 2016; Walters and Michalski, 2015, 2016a). Field $\delta^{15}N$ observations of NO_2 and nitrate have demonstrated the potential of these fractionation effects to offer additional valuable information concerning NO_x photochemical cycling and atmospheric nitrate formation (Albertin et al., 2021; Bekker et al., 2023; Li et al., 2021; Walters et

al., 2018). Recently, a novel chemical mechanism was devised to model the nitrogen isotope fractionation associated with NO_x chemistry, called incorporating ^{15}N into the Regional Atmospheric Chemistry Mechanism (i_NRACM) (Fang et al., 2021). Leveraging these advancements, we may utilize $\delta^{15}N$ to gather supplementary quantitative insights into BVOC/NO_x interactions and their impact on ~~organic nitrogen fates~~$RONO_2$ and contributions to HNO_3 formation. Importantly, nitrogen isotope fractionation may lead to distinct $\delta^{15}N$ values in HNO_3 and $RONO_2$ due to differences in their formation pathways. If characterized, these $\delta^{15}N$ signatures could offer an additional tracer for quantifying $RONO_2$ contributions to the overall HNO_3 budget. While strides have been made in understanding $\delta^{15}N$ fractionation during NO_y oxidation and equilibrium partitioning (Freyer et al., 1993; Li et al., 2020; Walters et al., 2016; Walters and Michalski, 2015), the specific nitrogen fractionation factors associated with HNO_3 and $RONO_2$ formation remain poorly constrained. Targeted laboratory and field studies are needed to directly measure these values and validate their use as diagnostic tools in atmospheric reactive nitrogen chemistry.

This study presents the first simultaneous measurements of $\Delta^{17}O$, $\delta^{18}O$, and $\delta^{15}N$ in key NO_y species that included NO_2, HNO_3, and $RONO_2$ that were generated under controlled laboratory conditions involving α-pinene oxidation. By varying oxidant regimes to probe distinct RO_2 fates, we aimed to (1) determine the $\Delta^{17}O$ and $\delta^{15}N$ values of simultaneously collected HNO_3, NO_2, and $RONO_2$ under a range of atmospheric oxidation conditions; (2) evaluate the validity of oxygen isotope mass-balance assumptions used in the formation of NO_2, HNO_3, and $RONO_2$; (3) characterize nitrogen isotope fractionation patterns across NO_y species; and (4) assess whether stable isotope measurements can provide meaningful constraints on the fate of $RONO_2$ in the atmosphere. Further, by incorporating recent isotope modeling frameworks (Walters et al., 2024a) we simulated the $\Delta^{17}O$ values of various NO_y components and compared them against observations, yielding insights into the oxidative formation and $\Delta^{17}O$ transfer dynamics during NO_y oxidation.

~~This study presents the first $\Delta^{17}O$, $\delta^{18}O$, and $\delta^{15}N$ values of several simultaneously collected NO_y species, including NO_2, HNO_3, and pNO_3, from controlled laboratory experiments involving α pinene, the most abundant monoterpene. These experiments were conducted under diverse oxidant conditions to investigate distinct RO_2 fates, enabling a comprehensive evaluation of the impact of BVOC/NO_x interactions on atmospheric oxidant budgets, organic nitrogen fates, and NO_x loss and/or recycling. The $\Delta^{17}O$ and $\delta^{15}N$ of the various NO_y components were simulated utilizing recently developed isotope mechanism frameworks (Fang et al., 2021; Walters et al., 2024a), yielding invaluable insights into the formation mechanisms and fates of NO_x, HNO_3, and organic nitrogen under varying oxidant conditions. Additionally, this approach tremendously aids in our understanding of $\Delta^{17}O$ transfer dynamics as well as $\delta^{15}N$ fractionation patterns associated with NO_x oxidation chemistry.~~

2 Methods

2.1 Chamber Experiments

Photochemical and nighttime oxidation chamber experiments were conducted involving α-pinene, NO_x, and oxidant precursors at the Georgia Institute of Technology Environmental Chamber Facility that houses two 12 m^3 Teflon reactors (Boyd et al., 2015). A total of six different initial experimental conditions were targeted, including five photochemical and one nighttime condition as previously reported (Blum et al., 2023) (Table ~~1~~2). The experiments varied in their precursor concentrations and oxidant types, which were utilized to probe different α-pinene oxidation reactions involving OH, O_3, and ~~nitrate radical (~~NO_3~~)~~ and ~~alkylperoxy radical (~~RO_2~~)~~ fates. Replicates were conducted in two of the targeted experimental conditions. The conducted chamber experiments follow ~~well-established~~previous laboratory protocols ~~and experimental conditions~~ (Boyd et al., 2015; Nah et al., 2016; Takeuchi and Ng, 2019; Tuet et al., 2017). Briefly, photochemical experiments were conducted by injecting dry ammonium sulfate seed aerosol and precursor (i.e., α-pinene (99 % Sigma-Aldrich)), NO (Matheson), hydrogen peroxide (H_2O_2), or nitrous acid (HONO)) into the chamber, where either H_2O_2 or HONO was used as an OH precursor to simulate different extents of RO_2+NO pathway. Once the levels of precursors stabilized, the chamber lights were turned on, signifying the start of the photochemical experiments. The procedure used to generate HONO (e.g., the reaction of sodium nitrite with sulfuric acid) also leads to the generation of significant NO and NO_2 as a reaction by-product (Kroll et al., 2005; Tuet et al., 2017). For simulated nighttime conditions, dry ammonium sulfate seed aerosol and α-pinene were injected into the chamber, followed by flowing dinitrogen pentoxide (N_2O_5) for fifteen minutes (Boyd et al., 2015; Takeuchi and Ng, 2019). The N_2O_5 injection corresponded to the start of the nighttime experiments. The N_2O_5 was generated by reacting NO_2 from a gas cylinder (Matheson) with O_3 in a flow tube prior to the introduction to the chamber at a ratio of 2:1 to minimalize O_3 concentrations in the chamber to avoid ozonolysis. All experiments were conducted at a relative humidity (RH) and temperature of 30 % and 22 °C, respectively. Before each experiment, the chamber was flushed with zero air and irradiated for at least 24 hours.

Table 2~~1~~. Summary of measured NO_y precursor concentrations and targeted H_2O_2 concentrations for the chamber experiments. All experiments were conducted using dry ammonium sulfate seed at a fixed temperature (22 °C) and relative humidity (30 %). ~~**The experiments were conducted using two different chambers designated as A and B.**~~

Experiment	α-pinene (ppb)	NO_y (ppb)	Oxidant (ppb)
1	298	NO^a = 55.3 ~~$HNO_3{}^d$ = 5.1~~	H_2O_2 = 9,000
1R	297	NO^a = 49.5 ~~$HNO_3{}^d$ = 3.5~~	H_2O_2 = 9,000
2	290	NO^a = 112 ~~$HNO_3{}^d$ = 3.18~~	H_2O_2 = 6,000

3	286	NO[a] = 338 ~~HNO_3[d] = 4.77~~	H_2O_2 = 6,000
4	293	NO[a] = 615 ~~HNO_3[d] = 5.74~~	H_2O_2 = 4,500
4R	316	NO[a] = 655 ~~HNO_3[d] = 5.51~~	H_2O_2 = 4,500
5	306	HONO[b] = 210 NO[b] = 320 NO_2[b] = 460 ~~HNO_3[d] = 9.08~~	N/A
6	100	NO_2[ea], NO_3[ea], N_2O_5[ea], HNO_3[ea], O_3 = ~~de~~[ea] ~~HNO_3 = 10.0~~	N/A

~~[a]The starting NO was assumed to have a $\Delta^{17}O$ = 0‰ and $\delta^{15}N$ = 70.0‰~~

~~[b]The starting HONO, NO, and NO_2 were assumed to have $\Delta^{17}O$ = 0‰ and $\delta^{15}N$ = 5.9‰~~

~~[e]The chamber HNO_3 "blank" was assumed to have $\Delta^{17}O$ = 26‰ and $\delta^{15}N$ = 35‰.~~

~~de~~[ea]The emission rate of NO_2, NO_3, N_2O_5, HNO_3, and O_3 into the chamber for a 20 minute injection period were modeled based on a flow tube simulation of the reaction of NO_2 with O_3 with a residence time of 70 s. ~~The initial NO_2 was assumed~~ measured ~~to have a $\Delta^{17}O$ = 0‰ and $\delta^{15}N$ = 40.5‰~~

Continuous online measurements of NO, NO_2, and O_3 were conducted using chemiluminescence (Teledyne 200EU), cavity-attenuated phase shift (CAPS), and an O_3 monitor (Teledyne T400). A chemical ionization mass spectrometer (CIMS) was used for various NO_y measurements including HONO and HNO_3 (Huey et al., 1998). The α-pinene decay was monitored using gas-chromatography flame ionization detector (GC-FID; Agilent 7890A). Gaseous ~~O~~organic nitrate were monitored using a filter inlet for gases and AEROsols (FIGAERO) coupled to a high-resolution time-of-flight iodide chemical ionization mass spectrometer (HR-ToF-I-CIMS) with particles collected on a Teflon filter (Lopez-Hilfiker et al., 2014; Nah et al., 2016; Takeuchi et al., 2022; Takeuchi and Ng, 2019; Wang et al., 2023). Aerosol composition was measured using a high-resolution time-of-flight aerosol mass spectrometer (HR-ToF-AMS) that included measurement of non-refractory organics (Org), sulfate (SO_4), nitrate (NO_3), and ammonium (NH_4) (DeCarlo et al., 2006; Farmer et al., 2010). Water-soluble aerosol components were also measured using a particle-into-liquid sampler (PILS) coupled to ion chromatography (IC) (Orsini et al., 2003). This method differs from the HR-ToF-AMS measurements, which quantify total aerosol composition, including both water-soluble and water-insoluble components. For example, nitrate measured by the AMS represents total pNO_3, whereas nitrate measured by the PILS-IC system corresponds only to the water-soluble fraction of pNO_3.

Collections of various NO_y gaseous and aerosol components, including HNO_3, NO_2, and pNO_3 were conducted using a modified version of the ChemComb Speciation Cartridge (CCSC) with an extended denuder body for offline concentration and isotope composition analysis (Blum et al., 2020, 2023). Briefly, the CCSC collections began when the aerosol mass spectrometer data indicated the nitrate and secondary organic aerosol mass concentrations had peaked. The CCSC samples were collected at 8 L min^{-1} for up to 4 h. To maintain the chamber integrity, zero-air was used to dilute at 25 L min^{-1} once aerosol peak was reached and CCSC sample collection initiated. The CCSC denuder bodies were replaced one to four times depending on the concentration of NO_x in the chamber. For each experiment, a single filter was used in the CCSC. In addition to the chamber experiments, samples were collected directly from the NO_2 tank (Matheson), which was used in the generation of N_2O_5 for the nighttime oxidation experiments.

Honeycomb denuders were coated for the selective collection of HNO_3 (captured as nitrate (NO_3^-)) and NO_2 (captured as nitrite (NO_2^-)). A detailed description of the coating solutions, denuder preparation, and denuder extraction was previously described, and the pooled isotope reproducibility for both HNO_3 and NO_2 was ±1.7 ‰, ±1.8 ‰, and ±0.7 ‰, for $\delta^{15}N$, $\delta^{18}O$, and $\Delta^{17}O$ ~~(Blum et al., 2023)~~ for these chamber experiments (Blum et al., 2023). The collection of $PM_{2.5}$ was conducted using a quartz filter (Cytiva Whatman, Grade QM-A; 47 mm diameter) that was housed in the ChemComb filter cartridge positioned downstream of the denuders. Prior to use, filters were pre-combusted at 550 °C overnight and stored in an airtight container. Quartz filters were selected because they facilitate efficient water-based extraction of collected material and tolerate high-temperature pre-cleaning to remove organic contaminants. ~~Before use, the quartz fiber filters were placed in a furnace at 550 °C overnight and stored in an airtight container.~~ The filter samples were extracted in 20 mL of Milli-Q water (>18.2 MΩ) and allowed to leach for at least one week at room temperature. This method was conducted to enable hydrolysis of collected organic nitrate particles as previous studies have shown organic nitrate derived from α-pinene oxidation to hydrolyze to NO_3^- in water with a lifetime of 8.8 h at pH = 6.9 (Rindelaub et al., 2016) and 2.5 h at pH = 7.44 (Wang et al., 2021). Other types of organic nitrate, such as secondary nitrates, have been reported to be stable in water, especially at a neutral pH (Wang et al., 2021). The efficiency of our filter extraction technique for facilitating organic nitrate hydrolysis was evaluated using the online AMS and PILS data. After the filters were leached, the filters were removed, and the samples were shipped to Brown University where they were placed in a freezer until subsequent concentration and isotope analysis. For all sample media types, including denuders and filters, lab blanks were frequently taken. These blanks were prepared, handled, and analyzed the same way as all samples.

2.2 Concentration and Isotope Analysis

The denuder and filter extracts were analyzed for their NO_2^- and NO_3^- content using a standardized colorimetric technique (e.g., EPA Methods 353.2) or ion chromatography, as previously described (Blum et al., 2020, 2023). The limits of detection (LOD) were approximately 0.1 μmol L^{-1} and 0.3 μmol L^{-1} for NO_2^- and NO_3^- via colorimetric analysis and 3.0 μmol L^{-1} for

NO_2^- via ion chromatography. For all analyses, the average percent relative standard deviation was below 5 %. The NO_2^- and NO_3^- concentrations from denuder blank extractions used for NO_2 (n = 5) and HNO_3 (n = 5) collection were below detection limits. Significant blanks were observed in the quartz filter extracts (1.5 ± 0.2 μmol L^{-1}; n = 5), which we refer to hereinafter as a method blank.

The $\delta^{15}N$, $\delta^{18}O$, and $\Delta^{17}O$ isotope compositions were analyzed using the denitrifier method for NO_3^- samples (e.g., from HNO_3 denuder and aerosol filter extracts) following (Casciotti et al., 2002; Kaiser et al., 2007; Sigman et al., 2001) and the sodium azide/ in an acetic acid buffer method for NO_2^- samples (from NO_2 denuder extracts), following (McIlvin and Altabet, 2005; Walters and Hastings, 2023) (Casciotti et al., 2002; McIlvin and Altabet, 2005; Sigman et al., 2001; Walters and Hastings, 2023). Briefly, 20 nmol of NO_3^- or NO_2^- samples were converted to these methods produce N_2OO from NO_3^- and/or NO_2^-, which is extracted, purified, concentrated, and injected into a continuous flow isotope ratio mass spectrometer for $\delta^{15}N$ and $\delta^{18}O$ determination from m/z measurement at 44, 45, and 46. In a separate batch analysis, 50 nmol of NO_3^- or NO_2^- were converted to the generated N_2O, is decomposed to O_2 using a gold tube heated at 770 °C, and analyzed for $\Delta^{17}O$ determination from at m/z measurement at 32, 33, and 34 for $\Delta^{17}O$ determination (Kaiser et al., 2007; Walters and Hastings, 2023). To minimize potential memory effects from residual O_2 gold tube and headspace trapping system, samples were grouped and analyzed in separate batches based on their expected $\Delta^{17}O$ values. Specifically, NO_2 samples (high $\Delta^{17}O$), HNO_3 (moderate $\Delta^{17}O$), and pNO_3 (low $\Delta^{17}O$) were each analyzed in separatededicated batches. Analytical blanks associated with the conversion of NO_3^- and/or NO_2^- to N_2O or O_2 for subsequent IRMS analysis were assessed for each batch and were always below detection limit (~0.2 nmol). These blanks are not anticipated to affect the analytical precision of the reported isotope values. The samples were calibrated with respect to internationally recognized NO_3^- standards (IAEA-NO-3, USGS35, USGS34) or NO_2^- reference materials (RSIL-N7373 and RSIL-10219) (Böhlke et al., 2003, 2007). In line with the identical treatment principle, the reference materials are treated the same as samples, including matching concentrations, sample amounts, and reagent additions to ensure analytical consistency. The pooled standard deviations of the standards reference materials were ±0.1 ‰ and ±0.6 ‰ for $\delta^{15}N$ and $\delta^{18}O$ of the NO_3^- standards (n = 78) and ±0.3 ‰ and ±0.3 ‰ for $\delta^{15}N$ and $\delta^{18}O$ of the NO_2^- reference materials (n = 15), respectively. The $\Delta^{17}O$ had a pooled standard deviation of ±0.6 ‰ (n = 53) .

All isotope measurements were reported relative to reference standards using delta (δ) notation (Eq. 1):

$$\delta = \left(\frac{R_x}{R_{std}} \frac{{}^{x}R_{sample}}{{}^{x}R_{reference}} - 1\right) \quad \text{(Eq. 1)}$$

where x refers to the heavy isotope (i.e., ^{15}N, ^{18}O, or ^{17}O) and where R refers to theis the ratio of the abundance of the heavy to the light isotope (i.e., $^{15}N/^{14}N$, $^{18}O/^{16}O$, or $^{17}O/^{16}O$), x denotes the sample, and std is an abbreviation for standard (Sharp, 2017)for the sample or the reference material. The nitrogen and oxygen reference material includes atmospheric air and Vienna Standard Mean Ocean Water (VSMOW), respectively. Oxygen isotope mass-independence ($\Delta^{17}O$) was quantified using the

linear definition with a mass-dependent coefficient of 0.52, which is approximately representative of oxygen mass-dependent coefficients expected and observed in nature (Young et al., 2002) (Eq. 2):

$$\Delta^{17}O = \delta^{17}O - 0.52 \times \delta^{18}O \quad \text{(Eq. 2)}$$

The linear $\Delta^{17}O$ approximation is commonly used to describe large mass-independent ~~effects~~ fractionation such as those related to O_3 reactions, and this definition is commonly used in the atmospheric chemistry community to track the influence of O_3 oxidation and $\Delta^{17}O$ propagation into reactive components (Alexander et al., 2020; Kim et al., 2022; Michalski et al., 2003; Savarino et al., 2013).

2.3 Data Reduction and Corrections

Due to significant NO_3^- blanks found in the pNO_3 filter extracts (i.e., method blank), the measured nitrate isotope values ($\delta^{15}N$, $\delta^{18}O$, and $\Delta^{17}O$) were corrected using a mass-balance approach ~~based on mass-balance~~to isolate the isotopic composition of NO_3^- generated within the chamber experiments (Eq. 3-4):

$$\delta(\text{corrected}, pNO_3) = \frac{\delta(\text{measure}) - (f(\text{blank}) \times \delta(\text{blank}))}{1 - f(\text{blank})} \quad \text{(Eq. 3)}$$

$$f(\text{blank}, pNO_3) = \frac{[NO_3^-(\text{blank})]}{([NO_3^-(\text{blank})] + [NO_3^-(\text{sample})])} \quad \text{(Eq. 4)}$$

where $[NO_3^-]$, corresponds to the concentration of NO_3^- in either the blank or sample, and f(blank) ~~corresponds to the fraction of NO_3^- that corresponds to the blank~~corresponds to the NO_3^- method blank fraction. The quartz filter ~~extracts~~method blanks had measured $\delta^{15}N$, $\delta^{18}O$, and $\Delta^{17}O$ values of 1.6 ± 1.1 ‰, 16.6 ± 1.4 ‰, and 3.4 ± 0.5 ‰, respectively ($n = 3$). Blank corrections were made for all samples when f(blank) was less than 30 %. Samples with an f(blank) that exceeded 30 % were not reported for their isotope compositions, which included 1 out of 8 quartz filter extracts. The uncertainty in the blank corrected isotope deltas was calculated using a Monte-Carlo simulation for 10,000 iterations and assuming a normal distribution using Matlab. For the quality assurance criterion of an f(blank) < 30 %, the uncertainties were calculated to be less than 4.1 ‰, 1.4 ‰, and 0.9 ‰ for $\delta^{15}N$, $\delta^{18}O$, and $\Delta^{17}O$, respectively. These values are small compared to the observed ranges for pNO_3, which spanned 67.8 ‰ for $\delta^{15}N$, 29.3 ‰ for $\delta^{18}O$, and 10.4 ‰ for $\Delta^{17}O$, and thus do not significantly affect the interpretation of isotope patterns. These uncertainties reflect the standard deviation of the 10,000 Monte Carlo iterations for each pNO_3 sample, which account for uncertainty in both the sample and method blank concentrations and isotope values. These reported uncertainties for chamber-derived pNO_3 isotope values represent total propagated error after blank correction, not the raw instrumental precision.

2.4 Aerosol Nitrate Composition

The relative contribution of organic aerosol nitrate (pNO_3(Org)) to the total pNO_3 was determined from two approaches. First, the relative proportion of pNO_3(Org), was calculated based on NO^+ and NO_2^+ HR-ToF-AMS fragmentation as previously described (Farmer et al., 2010; Fry et al., 2009; Kiendler-Scharr et al., 2016; Xu et al., 2015a) (Eq. 5):

$$f(\mathrm{pNO_3, Org}) = \frac{(R_{obs} - R_{AN})(1+R_{ON})}{(R_{ON} - R_{AN})(1+R_{obs})} \quad \text{(Eq. 5)}$$

where $f(\mathrm{pNO_3}, \mathrm{Org})$ refers to the fraction of $\mathrm{pNO_3(Org)}$ to the total $\mathrm{pNO_3}$, R refers to $\mathrm{NO^+/NO_2^+}$ fragments, and obs, AN, and ON refers to the observed, ammonium nitrate, and organic nitrate, respectively. The R_{AN} was obtained from routine ionization efficiency calibration of the HR-ToF-AMS using 300 nm ammonium nitrate aerosols and was 1.37. The R_{ON} was calculated based on the measured R_{AN} and the ratio of R_{ON}/R_{AN} previously reported for similar conducted experiments (Takeuchi and Ng, 2019), resulting in an R_{ON} of 2.70 ± 0.29 and 3.86 ± 0.34 for photochemical and nighttime oxidation experiments, respectively. The second method for qualitatively determining $f(\mathrm{pNO_3}, \mathrm{Org})$ involved evaluating the relative change in the molar ratio of $\mathrm{NH_4/SO_4}$, as an increase in $\mathrm{NH_4/SO_4}$ has been observed to be associated with inorganic $\mathrm{pNO_3}$ formation (Takeuchi and Ng, 2019).

2.5 Box Model Simulations

The chamber experiments were simulated using the Framework for 0-D Atmospheric Modeling (F0AM) box model (Wolfe et al., 2016). The conducted model simulations primarily focus on accurately representing initial precursor oxidation (i.e., NO_y, α-pinene) and simulation of Δ^{17}O observations. We chose not to include δ^{15}N model simulations in this study due to several key uncertainties. These include incomplete knowledge of the δ^{15}N values of all initial NO_y sources, limited constraints on isotope effects during NO_y oxidation and photolysis reactions, ~~and~~ the potential for unquantified, species-specific fractionation due to chamber wall interactions, and potential for chamber blanks with unknown δ^{15}N values. Given these limitations, δ^{15}N modeling will be deferred to future work focused specifically on nitrogen isotope dynamics.

The model was initiated for each experiment using the measured precursor concentrations for NO, $\mathrm{NO_2}$, HONO, and α-pinene before chamber lights were turned on or $\mathrm{N_2O_5}$ was injected and using the targeted $\mathrm{H_2O_2}$ concentrations. ~~Additionally, a "chamber blank" of $\mathrm{HNO_3}$, based on the CIMS measurements, was present before the start of the experiment (Fig. S1). To accurately reflect this condition in the model, an initial concentration of $\mathrm{HNO_3}$ was included in the experimental simulations based on the observed CIMS measurements (Table 1).~~ The pressure, temperature, and relative humidity were fixed at 1013 mbar, 295 K, and 30 %, respectively. The measured chamber light flux data was used. The model was run in two parts for the photochemical reactions, including from lights on to peak SOA mass concentration (part 1) and from aerosol decay and chamber dilution to the end of NO_y collections (part 2). For the nighttime experiments, the model simulations were conducted in three parts, including from the start of $\mathrm{N_2O_5}$ injection to the end of $\mathrm{N_2O_5}$ injection (part 1), from the end of $\mathrm{N_2O_5}$ injection to peak SOA mass concentrations (part 2) and from the decay of organic aerosol and chamber dilution to the end of NO_y collection (part 3). The $\mathrm{N_2O_5}$ injection was simulated by first modeling the $\mathrm{NO_2}$ reaction with $\mathrm{O_3}$ in the flow tube, considering a flow tube residence time of 70 s. The nighttime experiment was then simulated by allowing the flow tube products (i.e., $\mathrm{NO_2}$, $\mathrm{O_3}$, $\mathrm{NO_3}$, $\mathrm{HNO_3}$, and $\mathrm{N_2O_5}$) to emit into the chamber for 20 minutes (part 1). Next, the experiment was modeled without the flow tube emission to the start of aerosol decay and chamber dilution (part 2) and from aerosol decay and chamber dilution to

the end of NO_y collections (part 3). For both photochemical and nighttime experiments, the model simulations from the decay of organic aerosol to the end of NO_y collection included a chamber dilution rate constant (k_{dil}) of 3.47×10^{-5} s^{-1}, which was calculated based on the dilution flow rate (25 LPM) and chamber volume (12 m^3). Sensitivity tests were performed to assess the impact of the selected k_{dil} on model results by evaluating a range of ~~values from 1×10^{-5} s^{-1} to 1×10^{-4} s^{-1}. For both photochemical and nighttime experiments, the model simulations from the decay of organic aerosol to the end of NO_y collection included a chamber dilution rate of $k_{dil} = 8.00 \times 10^{-5}$ s^{-1}, which was determined based on accurately matching the decay of NO for the photochemical experiments with the highest levels of initial starting NO_y (i.e., Exp. 4, and 5).~~ k_{dil} values.

A new chemical mechanism was developed, termed NO_x-α-pinene (NO_x-API), to accurately model the oxidation of NO_x and α-pinene (Table S1-S6). This mechanism was developed due to difficulties in simulating the initial decay of the aerosol precursors including α-pinene, NO, NO_2, and HONO for the various experimental conditions using either the Regional Atmospheric Chemical Mechanism, v2 (RACM2) (Goliff et al., 2013) or the Master Chemical Mechanism v3.3.1 (Jenkin et al., 1997; Saunders et al., 2003). The NO_x-API mechanism focuses on simulating α-pinene and NO decay along with NO_x oxidation but does not intend to accurately simulate SOA production and later-generation chemistry. The mechanism has the inorganic reactions in RACM2, including 16 species and 45 reactions. It also incorporates 29 organic species and 61 reactions to detail organic chemistry up to one generation past pinonaldehyde formation as well as the formation of pinonaldehyde derived peroxyacetyl nitrate formation, with subsequent chemistry represented by a lumped approach. The α-pinene oxidation pathways involving OH, O_3, and NO_3, along with specific reactions of the resulting RO_2 with HO_2, NO, NO_3, and other RO_2 radicals, are also included. The photochemical oxidation of α-pinene largely follows the MCMv3.3.1 (Saunders et al., 2003), incorporating two hydroxyl-nitrate isomers from $OH/O_2/NO$, including one tertiary (ONITa) and one secondary (ONITb) and the formation of a tertiary pinene carbonyl nitrate (ONITc). Nighttime oxidation chemistry integrates a recent mechanism for organic nitrate formation, producing pinene nitrate hydroperoxide, including one tertiary (ONITOOHa) and one secondary (ONITOOHb) via HO_2 reactions and dimer/pinene dinitrate (PDN) through RO_2 interactions (Bates et al., 2022). The box-model simulation is a gas-phase mechanism that does not explicitly model heterogeneous reactions or aerosol chemistry, such as organic nitrate hydrolysis. The impact of heterogenous reactions are considered in the evaluation of the $\Delta^{17}O$ model simulation results compared to observations.

~~A new chemical mechanism was developed, termed University of South Carolina α-pinene (USC-API), to accurately model the oxidation of NO_x and α-pinene (Table S1-S2). This mechanism was developed due to difficulties in simulating the initial decay of the aerosol precursors including α-pinene, NO, NO_2, and HONO for the various experiment experimental conditions using either the Regional Atmospheric Chemical Mechanism, v2 (RACM2); (Goliff et al., 2013) or the Master Chemical Mechanism v3.3.1 (Jenkin et al., 1997; Saunders et al., 2003). The USC API mechanism focuses on simulating α-pinene and NO decay along with NO_x oxidation but does not intend to accurately simulate SOA production and later-generation chemistry. The mechanism includes the inorganic reactions included in RACM2, including 16 species and 45 reactions. It also~~

~~incorporates 29 organic species and 61 reactions to detail organic chemistry up to one generation past pinonaldehyde formation as well as the formation of pinonaldehyde derived peroxyacetyl nitrate formation, with subsequent chemistry represented by a lumped approach. The α-pinene oxidation pathways involving OH, O_3, and NO_x along with specific reactions of the resulting RO_2 with HO_2, NO, NO_3, and other RO_2 radicals, are included. The photochemical oxidation of α-pinene largely follows the MCMv3.3.1 (Saunders et al., 2003), incorporating two hydroxyl nitrate isomers from OH/O_2/NO, including one teritary (ONITa) and one secondary (ONITb) and the formation of a tertiary pinene carbonyl nitrate (ONITc). Nighttime oxidation chemistry integrates a recent mechanism for organic nitrate formation, producing pinene nitrate hydroperoxide, including one tertiary (ONITOOHa) and one secondary (ONITOOHb) via HO_2 reactions and dimer/pinene dinitrate (PDN) through RO_2 interactions (Bates et al., 2022). The box model simulation is a gas phase mechanism that does not explicitly model heterogeneous reactions or aerosol chemistry, such as organic nitrate hydrolysis. Product yields for organic nitrate were adjusted based on experimental isotope data, accounting for OH/O_2/NO and NO_3 pathways, which can be elucidated based on a comparison to $\Delta^{17}O$ (Walters et al., 2024b).~~

The $\Delta^{17}O$ of NO_y compounds were simulated using the newly developed ~~USC~~NO_x-API mechanism modified using the InCorporating Oxygen Isotopes of oxidized reactive Nitrogen in the Regional Atmospheric Chemistry Mechanism, Version 2 (ICOIN-RACM2) model framework (Walters et al., 2024a). Briefly, the model framework tracks the transfer and propagation of $\Delta^{17}O$ from O_3 into NO_y and O_x species. This mechanism tags the oxygen atoms transferred from O_3 into NO_y and O_x considering mass-balance and reaction stoichiometry and enables the offline calculation of $\Delta^{17}O$ based on the output of concentrations of various NO_y and HO_x isotopologues (Eq. 6):

$$\Delta^{17}O(X) = f(Q) \times \Delta^{17}O(O_3^{term}) \quad \text{(Eq. 6)}$$

where X refers to the various NO_y and O_x molecules and f(Q) is the ~~fractional number~~fraction of oxygen-atoms deriving from O_3^{term} for a particular molecule. The $\Delta^{17}O(O_3^{term})$ represents the $\Delta^{17}O$ value of the terminal and transferrable O atom of O_3, which was assumed to be 39 ± 2 ‰ based on recent near-surface collections of O_3 (Ishino et al., 2017; Vicars and Savarino, 2014) and O_3 generated from O_2/NO_x photochemical experiments conducted under normal temperature and pressure conditions (Michalski et al., 2014). ~~As a model sensitivity test, $\Delta^{17}O(O_3)$ was also estimated from the modeled $f(O)$ values and measured $\Delta^{17}O$ of the NO_y species. The initial $\Delta^{17}O(NO)$ and $\Delta^{17}O(NO_2)$ was set to 0‰, while the initial $\Delta^{17}O(HNO_3)$ from the "chamber blank" was set to 26‰, representing 2/3 O atoms derived from O_3. This value was not measured but assumed based on the measured $\Delta^{17}O(HNO_3)$ for Exp. 1 and 2, in which the HNO_3 "chamber blank" significantly contributed to the total produced experimental HNO_3, up to approximately 20% (Fig. S1).~~

All $\Delta^{17}O$ model simulations were conducted without considering chamber wall losses. The potential impact of wall loss was evaluated through sensitivity tests that involved comparing simulated $\Delta^{17}O$ values. The sensitivity tests included a no wall loss case, wall loss involving O_3, NO, NO_2, HNO_3, N_2O_5, and organic nitrate based on previous reports from chamber experiments (Morales et al., 2021; Wang et al., 2014), and an elevated wall loss scenario, in which the wall loss rate constants were increased by ×10 scenario to account for uncertainty since wall loss rates were not determined in this work (Table S7).

~~Additionally, $\delta^{15}N$ of NO_y molecules were also simulated by adapting the framework from the recently developed isotope variant of the RACM2 mechanism, termed i_NRACM: incorporating ^{15}N into the Regional Atmospheric Chemistry Mechanism (Fang et al., 2021). The model framework explicitly tracks the ^{15}N and ^{14}N abundance of various NO_y molecules and includes nitrogen isotope fractionation associated with NO_x oxidation. The $\delta^{15}N$ of various NO_y components is then calculated using a $^{15}N/^{14}N$ ratio of 0.003677 for air(Coplen et al., 1992). The $\delta^{15}N$ chamber simulations were initiated with starting concentrations for the nitrogen isotopologues depending on the initial NO_y source.~~ The $\delta^{15}N$ chamber simulations were initiated with starting concentrations for the nitrogen isotopologues depending on the initial NO_y source. ~~The $\delta^{15}N$ chamber simulations were initiated with starting concentrations for the nitrogen isotopologues depending on the initial NO_y source. For the nighttime oxidation experiments that used NO_2 as the initial NO_y source (Exp. 6), the starting $\delta^{15}N(NO_2)$ was set to -40.5 ‰, which was the measured value from the NO_2 source (Matheson NO_2 tank) (-40.5±0.5 ‰; n = 3). For the experiments that initialize experiments using NO (Exp. 1-4), a $\delta^{15}N(NO)$ value of -70.0±1.4 ‰ was assumed based on previous measurements from a commercially available tank of NO (Fibiger et al., 2014). Finally, for the HONO experiments (Exp. 5), a $\delta^{15}N(HONO)$ value of -5.9±0.5 ‰ was assumed based on the lab generation of HONO in a previous study, following a similar methodology as utilized in this study (Chai and Hastings, 2018).~~ ~~For the nighttime oxidation experiments that used NO_2 as the initial NO_y source (Exp. 6), the starting $\delta^{15}N(NO_2)$ was set to -40.5‰, which was the measured value from the NO_2 source (Matheson NO_2 tank) (-40.5±0.5‰; n = 3). For the experiments that initialize experiments using NO (Exp. 1-4), a $\delta^{15}N(NO)$ value of -70.0±1.4‰ was assumed based on previous measurements from a commercially available tank of NO (Fibiger et al., 2014). Finally, for the HONO experiments (Exp. 5), a $\delta^{15}N(HONO)$ value of -5.9±0.5‰ was assumed based on the lab generation of HONO in a previous study, following a similar methodology as utilized in this study (Chai and Hastings, 2018). Additionally, the "chamber blank" $\delta^{15}N(HNO_3)$ was set to -35‰, which was the average of the photochemical experiments using H_2O_2 and a high initial NO concentration (Exp. 4).~~

~~The base chemistry in all of the model simulations is identical and the tagging of the isotope tracers does not impact the model chemistry (Fang et al., 2021; Walters et al., 2024a). All model simulations were conducted without considering chamber wall losses. The potential impact of wall loss was evaluated through sensitivity tests that involved comparing simulated HNO_3~~

~~concentrations and $\Delta^{17}O$ values. The sensitivity tests included a no wall loss case, wall loss based on previous estimates (Wang et al.)(Morales et al., 2021; Wang et al., 2014), and a wall loss ×10 scenario to account for uncertainty since wall loss rates were not determined in this work (Table S1). All model simulations were conducted without considering chamber wall loss. Additionally, these are gas-phase mechanisms and do not explicitly model heterogeneous reactions or aerosol chemistry. Further, given the low relative humidity conditions and dry aerosol seed conditions, organic nitrate hydrolysis was not included in the initial model. The chemical mechanism performance in simulating $\Delta^{17}O$ and $\delta^{15}N$ values and thus oxidation chemistry was evaluated using the RMSE metric (Eq. 7):~~

~~$$RMSE = \sqrt{\frac{1}{n}\sum_{i=1}^{n}(\Delta^{17}O_o\delta_o - \Delta^{17}O_m\delta_m)^2} \quad \text{(Eq. 7)}$$~~

~~where $\Delta^{17}O\delta_o$ are the isotope observations, $\Delta^{17}O\delta_m$ are the model simulated values, and n is the number of observations. Adjustments to the model chemistry and/or oxygen isotope mass balance were conducted to reduce the RMSE values.~~

3. Results and Discussion

3.1 Isotope Observations

The $\Delta^{17}O$, $\delta^{18}O$ and $\delta^{15}N$ measurements of NO_y species offer insight into the oxidation pathways and sources contributing to their formation. In this study, we focus on interpreting the $\Delta^{17}O$, $\delta^{18}O$, and $\delta^{15}N$ of NO_2, HNO_3, and pNO_3 collected under a range of controlled experiments involving NO_x/α-pinene oxidation. These observations provide constraints on the relative importance of different oxidants (e.g., O_3, OH, RO_2) and reaction mechanisms, and they also allow us to test our understanding of oxygen isotope mass-balance assumptions, O-isotope transfer dynamics, and nitrogen isotope fractionation associated with NO_x oxidation. Below, we first discuss the observed patterns in oxygen isotopes ($\Delta^{17}O$ and $\delta^{18}O$), followed by an examination of nitrogen isotope ($\delta^{15}N$) trends, and their implications.

~~The $\Delta^{17}O$, $\delta^{18}O$ and $\delta^{15}N$ measurements of NO_y species offer insight into the oxidation pathways and sources contributing to their formation. In this study, we focus on interpreting the $\Delta^{17}O$, $\delta^{18}O$, and $\delta^{15}N$ of NO_2, HNO_3, and pNO_3 collected under a range of controlled chamber conditions. These observations provide constraints on the relative importance of different oxidants (e.g., O_3, OH, RO_2) and reaction mechanisms, and they also allow us to test our understanding of oxygen isotope mass-balance assumption, O-isotope transfer dynamics, and nitrogen isotope fractionation associated with NO_x oxidation. Below, we first discuss the observed patterns in oxygen isotopes ($\Delta^{17}O$ and $\delta^{18}O$), followed by an examination of nitrogen isotope ($\delta^{15}N$) trends and their implications.~~

3.1.1 $\Delta^{17}O$ and $\delta^{18}O$ of NO_y

The observations indicate a significant relationship between $\delta^{18}O$ and $\Delta^{17}O$ across NO_y species ($\delta^{18}O = 11.1(\pm1.0) + 2.42(\pm 0.04)\times\Delta^{17}O$; $r = 0.992$; $p < 0.01$) (Fig. 1A). The strong linear relationship between $\delta^{18}O$ and $\Delta^{17}O$ indicates that the oxygen isotopes of the various collected NO_y compounds derived from two dominant pools of O-sources, with high and low $\delta^{18}O$ and

$\Delta^{17}O$ values that were consistent across all experimental conditions. The observed $\Delta^{17}O$ and $\delta^{18}O$ values of NO_y species are anticipated to reflect a balance between oxygen atom transfer from O_3, which has high $\Delta^{17}O$ and $\delta^{18}O$ values, and oxygen atom transfer from RO_2, HO_2, OH, and H_2O which have lower $\Delta^{17}O$ and $\delta^{18}O$ values. Assuming a $\Delta^{17}O(O_3^{term})$ value of 39 ± 2 ‰ (Ishino et al., 2017; Vicars and Savarino, 2014), would indicate a $\delta^{18}O$ transferred from O_3^{term} to the NO_y products of 106 ± 5.0 ‰. Conversely, the low-$\Delta^{17}O$ oxidant endmember at a $\Delta^{17}O \approx 0$ ‰ implies an associated $\delta^{18}O$ value of approximately 11.1 ± 1.0 ‰. This value likely reflects oxygen transfer from oxidants such as RO_2, HO_2, and OH.

The derived low-end $\delta^{18}O$ oxidant value is consistent with a scenario in which these radicals are sourced from atmospheric O_2 ($\delta^{18}O \approx 23$ ‰; (Craig, 1957), but undergo isotopic fractionation during their formation and subsequent oxygen atom transfer to NO_y. Although the exact $\delta^{18}O$ enrichment factors for RO_2/HO_2 or OH formation and reaction are not well-constrained, a net isotope enrichment factor ~ -12 ‰ is plausible, particularly for unidirectional reactions involving ^{18}O fractionation (Walters and Michalski, 2016). Additionally, contributions from OH could further influence the low $\delta^{18}O$ endmember, especially if oxygen atom exchange with ambient water vapor occurs (Dubey et al., 1997). Altogether, the inferred $\delta^{18}O$ of 11.1 ‰ for the low-$\Delta^{17}O$ oxidant endmember likely represents a composite signal from multiple oxidants (RO_2, HO_2, OH) originating from O_2 and/or H_2O, modified by kinetic and equilibrium isotope effects. Despite these uncertainties, the consistent $\delta^{18}O$–$\Delta^{17}O$ trend across NO_y products supports a two-endmember mixing model governed by oxidants with distinct isotopic values.

The $\Delta^{17}O$ and $\delta^{18}O$ values increased in the order pNO_3 ($\bar{x} \pm \sigma$; $\Delta^{17}O$ = 10.0 ± 3.4 ‰; $\delta^{18}O$ = 35.0 ± 10.1 ‰; n = 7) < HNO_3 ($\Delta^{17}O$ = 16.7 ± 2.0 ‰; $\delta^{18}O$ = 50.2 ± 4.5 ‰; n = 20) < NO_2 ($\Delta^{17}O$ = 29.6 ± 12.8 ‰; $\delta^{18}O$ = 84.1 ± 29.6 ‰; n = 20). The $\Delta^{17}O$ and $\delta^{18}O$ of NO_2, HNO_3, and pNO_3 were sensitive to the types of experiments and thus oxidant conditions (Fig. 1B). For example, NO_2 samples collected during the photochemical experiments (i.e., Exp. 1-5) indicated that $\delta^{18}O(NO_2)$ and $\Delta^{17}O(NO_2)$ increased with the initial $[NO_y]$, the ratio of initial $[NO_y]$:[BVOC], and with decreasing initial $[H_2O_2]$. These sensitivities of $\delta^{18}O(NO_2)$ and $\Delta^{17}O(NO_2)$ reflect the balance between NO branching ratios involving O_3 versus RO_2/HO_2 (Albertin et al., 2021; Walters et al., 2018). Thus, the relative branching ratios of $NO+O_3$ and $NO+RO_2/HO_2$ changed with experimental photochemical conditions, favoring a greater proportion of $NO+O_3$ reactions for higher initial NO_y and lower $[H_2O_2]$ conditions. For the nighttime oxidation experiment (Exp. 6), the $\Delta^{17}O$ and $\delta^{18}O$ reflected the initial production of N_2O_5 from the oxidation of NO_2 (from a gas cylinder) with O_3. The expected $\Delta^{17}O$ and $\delta^{18}O$ values can be calculated assuming N_2O_5 equilibrium between NO_3 and NO_2 (i.e., $N_2O_5 \rightleftharpoons NO_2 + NO_3$) and using O isotope mass balance (Eq. 7):

$$\delta(NO_2) = \frac{1}{5}\left(\delta(O_3^{term})\right) + \frac{4}{5}\left(\delta(NO_2^{tank})\right) \quad \text{(Eq. 7)}$$

where δ refers to either $\Delta^{17}O$ or $\delta^{18}O$, O_3^{term} refers to the O-atom at the terminal end of O_3 and NO_2^{tank} refers to the NO_2 from the tank source with measured $\Delta^{17}O$ and $\delta^{18}O$ values of -0.1 ± 0.1 ‰ (n = 3) and 13.1 ± 0.2 ‰ (n = 3), respectively. Using the assumed $\Delta^{17}O(O_3^{term})$ of 39 ± 2 ‰, and the calculated $\delta^{18}O(O_3^{term})$ incorporated into NO_y (106 ± 5.0 ‰) we estimate the $\Delta^{17}O$

and $\delta^{18}O$ of NO_2 for the nighttime oxidation experiment to be 7.7 ± 0.4 ‰ and 31.7 ± 1.0 ‰, respectively, which was near their measured values from the nighttime chamber experiments of (7.2 ± 0.2 ‰) and (31.9 ± 0.7 ‰) (n = 3), respectively.

~~The observations indicate a There was a significant relationship between $\delta^{18}O$ and $\Delta^{17}O$ across NO_y species ($\delta^{18}O = (11.1\pm1.0) + (2.42\pm 0.04)\times\Delta^{17}O$; $r = 0.992$; $p < 0.01$) (Fig. 1). The strong linear relationship between $\delta^{18}O$ and $\Delta^{17}O$ indicates that the oxygen isotopes of the various collected NO_y compounds derived between two dominant pools of O sources, with high and low $\delta^{18}O$ and $\Delta^{17}O$ values that were consistent across all experimental conditions. The observed $\Delta^{17}O$ and $\delta^{18}O$ values of NO_y species are anticipated to reflect a balance between oxygen atom transfer from O_3, which has high $\Delta^{17}O$ and $\delta^{18}O$ values, and oxygen atom transfer from RO_2, HO_2, OH, and H_2O which have lower $\Delta^{17}O$ and $\delta^{18}O$ values. The high-end member $\delta^{18}O$ and $\Delta^{17}O$ source can reasonably be assumed to derive from O_3^{term}. Assuming a $\Delta^{17}O(O_3^{term})$ value of 39.3±2.0 ‰ (Ishino et al., 2017; Vicars and Savarino, 2014), would indicate a $\delta^{18}O$ transferred from O_3^{term} to the NO_y products of 106±5.0 ‰.(Craig, 1957)(Dubey et al., 1997) Assuming the low-end member O source to have a $\Delta^{17}O$ of 0 ‰, indicates a $\delta^{18}O$ value of 11.1±1.0 ‰ transferred into the NO_y products that could be reasonably be expected to derive from RO_2, HO_2, and OH radicals. The $\delta^{18}O$ of RO_2 and HO_2 has previously been assumed to be equal to that of O_2 (~ 23 ‰), based on oxygen mass balance considerations and the absence of experimentally determined enrichment factors for O_2 transfer during the formation of RO_2/HO_2 and subsequent NO oxidation to NO_2 (Michalski et al., 2012).The $\delta^{18}O$ of RO_2/HO_2 radicals has previously been suggested to be near $\delta^{18}O(O_2)$ (Michalski et al., 2012). The derived low-endmember $\delta^{18}O$ value of 11.1±1.0 ‰ may reflect contributions from atmospheric O_2 ($\delta^{18}O \approx 23‰$) that has undergone isotope fractionation during its incorporation to RO_2/HO_2 and subsequently to NO_2 during NO oxidation, leading to a lower $\delta^{18}O$ signature incorporated into NO_y. The $\delta^{18}O$ enrichment factors for these processes remains uncertain, as to the best of our knowledge, no direct experimental or theoretical constraints exist for the $^{18}O/^{16}O$ fractionation associated with RO_2/HO_2 formation and transfer into NO_y species. However, an enrichment factor on the order of ~ 10‰ is plausible for unidirectional radical transfer processes, consistent with similar magnitudes observed for reactions involving O transfer, such as NO + O_3, which has been theoretically calculated to be on the order of ~ 20‰ (Walters and Michalski, 2016). In addition, the low $\delta^{18}O$ value may reflect contributions from other oxidants, such as OH. Nonetheless, the consistent $\delta^{18}O$-$\Delta^{17}O$ relationship observed across NO_y species implies that two dominant O-containing pools are driving their formation in the conducted chamber experiments.Indeed, the derived $\delta^{18}O$ value of 11.8±1.0‰ is near the atmospheric $\delta^{18}O(O_2)$ value of 23.2 ‰ (Craig, 1957), which should be near the O_2 in the chamber that was from a zero-air generator. Slight differences between these values could be due to kinetic isotope effects associated RO_2/HO_2 reactions. In addition to RO_2/HO_2 radicals, the OH radical plays an important role in the photochemical formation of HNO_3 and would be expected to proportionally transfer its O atom to the HNO_3 product.~~

~~The $\Delta^{17}O$ and $\delta^{18}O$ values increased in the order pNO_3 < HNO_3 < NO_2. The $\Delta^{17}O$ and $\delta^{18}O$ of NO_2, HNO_3, and pNO_3 were sensitive to the types of experiments and their oxidant conditions. For example, NO_2 samples collected during the photochemical experiments (i.e., Exp. 1-5) indicated that $\delta^{18}O(NO_2)$ and $\Delta^{17}O(NO_2)$ increased with the initial [NO_y], the ratio of initial [NO_y]:[BVOC], and with decreasing initial [H_2O_2]. These sensitivities to $\delta^{18}O(NO_2)$ and $\Delta^{17}O(NO_2)$ reflect the~~

balance between NO branching ratios involving O_3 versus RO_2/HO_2 (Albertin et al., 2021; Walters et al., 2018). Thus, the relative branching ratios of NO+O_3 and NO+RO_2/HO_2 changed with experimental photochemical conditions, favoring a greater proportion of NO+O_3 reactions for higher initial NO_y and lower [H_2O_2] conditions. For the nighttime oxidation experiment (Exp. 6), the $\Delta^{17}O$ and $\delta^{18}O$ reflected the initial production of N_2O_5 from the oxidation of NO_2 (from a gas cylinder) with O_3. The expected $\Delta^{17}O$ and $\delta^{18}O$ values can be calculated assuming N_2O_5 equilibrium between NO_3 and NO_2 (i.e., $N_2O_5 \rightleftharpoons NO_2 + NO_3$) and using O isotope mass balance (Eq. 8):

$$\delta(NO_2) = \frac{1}{5}\left(\delta(O_3^{term})\right) + \frac{4}{5}\left(\delta(NO_2^{tank})\right) \quad \text{(Eq. 8)}$$

where δ refers to either $\Delta^{17}O$ or $\delta^{18}O$, O_3^{term} refers to the O atom at the terminal end of O_3 and NO_2^{tank} refers to the NO_2 from the tank source with measured $\Delta^{17}O$ and $\delta^{18}O$ values of −0.1±0.1 ‰ (n=3) and 13.1±0.2 ‰ (n=3), respectively. Using the assumed $\Delta^{17}O(O_3^{term})$ of 39.3 ± 2.0 ‰, and the calculated $\delta^{18}O(O_3^{term})$ incorporated into NO_y (106±5.0 ‰) we would estimate the $\Delta^{17}O$ and $\delta^{18}O$ of NO_2 for the nighttime oxidation experiment to be 7.7 ±0.4 ‰ and 31.7±1.0 ‰, respectively, which was near their measured values from the nighttime chamber experiments of (7.2±0.2 ‰) and (31.9±0.7 ‰) (n = 3), respectively.

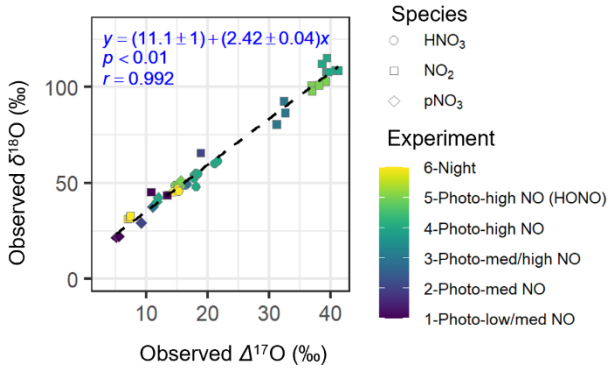

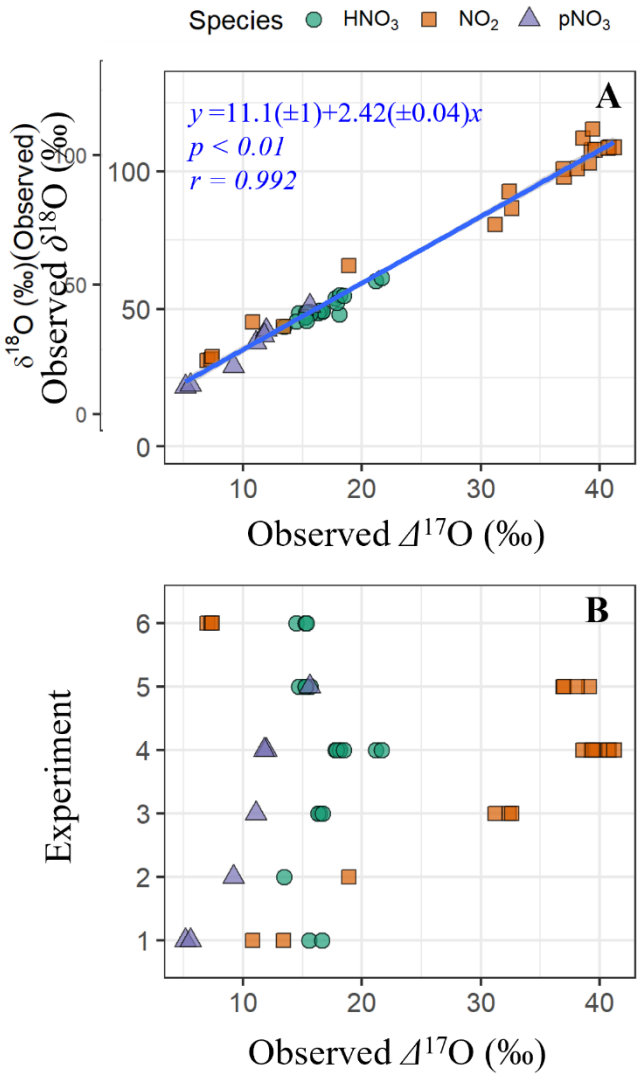

Fig. 1. The observed oxygen isotope delta values of various NO_y species (i.e., HNO_3, NO_2, and pNO_3) from the α-pinene/NO_y oxidation experiments. **including, (A) linear regression between $\delta^{18}O$ and $\Delta^{17}O$ and (B) $\Delta^{17}O$ values of NO_y species sorted by experiment.** ~~**A strong linear correlation (blue line) was observed between δ18O and Δ17O.**~~

3.1.2 $\delta^{15}N$ of NO_y

The observed $\delta^{15}N$ of all NO_y species exhibited a large range from -90.3 to -4.0 ‰ (n = 47) (Fig. 2A). This large range of $\delta^{15}N$ values were significantly influenced by the $\delta^{15}N$ values of the various initial NO_y sources that included tank-NO (Exp. 1-4), HONO (Exp. 5), and tank-NO_2 (Exp. 6). The experiments using tank-NO had the lowest $\delta^{15}N$ ($\bar{x} \pm \sigma$) of (-56.1 ± 21.3 ‰; n =

32), followed by tank-NO_2 of (-34.7 ± 12.2 ‰; n = 6), and the highest average was for the HONO experiments of (-7.8 ± 5.7 ‰; n = 9). The differences in the observed $\delta^{15}N$ values by NO_y source likely reflect the isotopic composition of the initial NO_y used in each experiment. The trend in observed $\delta^{15}N$ across experiments is consistent with either measured or literature-based reports of the $\delta^{15}N$ values of the initial NO_y species. For example, the $\delta^{15}N$ of laboratory generated HONO, prepared using a similar methodology as in this study, has been reported to be –5.9 ± 0.5 ‰ (Chai and Hastings, 2018). This value is relatively high compared to the $\delta^{15}N(NO_2)$ from tank-NO_2 used in these experiments that was measured to be -40.9 ± 0.2 ‰, which is higher than the $\delta^{15}N(NO)$ of tank-NO previously reported at -70.0 ± 1.4 ‰ (Fibiger et al., 2014). In addition to the source $\delta^{15}N$ effects, the experiments also indicate large $\delta^{15}N$ fractionation between the various NO_y species. Overall, $\delta^{15}N(HNO_3)$ averaged -25.9 ± 13.0 ‰ (n = 20), which was significantly higher than both $\delta^{15}N(NO_2)$ (-52.5 ± 25.2 ‰; n = 20) and $\delta^{15}N(pNO_3)$ (-72.6 ± 22.9 ‰; n = 7) based on a two-sample t-test ($p < 0.01$). While $\delta^{15}N(NO_2)$ values were higher than those of $\delta^{15}N(pNO_3)$, this difference was not statistically significant based on a two-sample t-test ($p > 0.05$). This trend suggests that the produced HNO_3 was generally associated with a positive nitrogen isotope enrichment factor ($^{15}\varepsilon$) favoring preferential incorporation of ^{15}N relative to NO_2, whereas pNO_3 formation involved a negative ε, favoring incorporation of ^{14}N.

We quantified the $\delta^{15}N$ enrichment of HNO_3 and pNO_3 relative to NO_2, as $\Delta\delta^{15}N$, (defined as $\delta^{15}N(product) - \delta^{15}N(NO_2)$) (Fig. 2B). Among the photochemical experiments initiated with NO and H_2O_2 (Exp 1-4), the average $\Delta\delta^{15}N(HNO_3–NO_2)$ was consistently high averaging 33.7 ± 7.1 ‰, while the HONO experiment (Exp. 5) had a much smaller enrichment value of 0.4 ± 1.7 ‰. This difference is somewhat surprising, given that both systems are expected to involve NO_2 + OH as a major pathway for HNO_3 production. The $^{15}\varepsilon$ associated with NO_2 + OH has yet to be directly measured but has been predicted in the literature with large differences in the suggested value. For example, the $^{15}\varepsilon$ for the NO_2+ OH has been suggested to be -3 ‰ based on the reduced masses of the transition complex (Freyer et al., 1993), while it has been predicted to be +40 ‰ in the i_NRACM mechanism based on the assumption that NO_2 and the excited HNO_3 intermediate formed during the NO_2 + OH reaction achieve isotopic equilibrium prior to collisional deactivation (Fang et al., 2021). The relatively low $\Delta\delta^{15}N(HNO_3–NO_2)$ observed in the HONO experiment is more consistent with the former, while the higher $\Delta\delta^{15}N(HNO_3–NO_2)$ values in the NO/H_2O_2 experiments support the latter interpretation. The cause of this discrepancy remains unclear but may reflect differences in reaction kinetics and environmental conditions. For example, in the HONO experiment, the aerosol formation peak (Fig. 3) and HNO_3 production (Fig. S1) occurred relatively rapidly compared to the NO/H_2O_2 experiments. This timing shift may potentially alter the influence of nitrogen isotope fractionation effects such as NO_x photochemical equilibrium. Additional isotope effects may also contribute, such as fractionation during HONO photolysis, unknown mass-dependent processes, or experimental artifacts including wall loss or residual background levels. Further investigation is needed to isolate and quantify the influence of these factors.

In the nighttime experiment (Exp. 6), $\Delta\delta^{15}N(HNO_3–NO_2)$ was also elevated with an average value of 22.2 ± 1.4 ‰. The cause of the nighttime ^{15}N enrichment in the generated HNO_3 relative to NO_2 is likely due to isotopic effects associated with the NO_2

+ $NO_3 \rightleftharpoons N_2O_5$ equilibrium, which has been predicted to have $^{15}\varepsilon$ of 25.5 ‰ at 300 K (Walters and Michalski, 2016b) falling near the observed value for the nighttime experiments (Fig. 2B). The $\Delta\delta^{15}N(pNO_3\text{–}NO_2)$ values were consistently negative, averaging –13.6 ± 5.8 ‰ across the photochemical experiments. This value suggests that pNO_3 formation involved reactions that preferentially favored ^{14}N. Before speculating on the cause of the low observed $\Delta\delta^{15}N(pNO_3\text{–}NO_2)$, it is essential to first determine the chemical composition of the produced pNO_3 and whether it originates primarily from inorganic or organic nitrate.

The observed $\delta^{15}N$ of all NO_y species exhibited a large range from -90.3 to -4.0 ‰ (n = 47) (Fig. 2A). This large range of $\delta^{15}N$ values were significantly influenced by the $\delta^{15}N$ values of the various initial NO_y sources that included tank NO (Exp. 1-4), HONO (Exp. 5), and tank NO_2 (Exp. 6) ($p < 0.01$). The experiments using tank NO had the lowest $\delta^{15}N$ ($\bar{x}\pm s$) of (-56.1±21.3 ‰; n = 32), followed by tank NO_2 of (-34.7±12.2 ‰; n = 6), and the highest average was for the HONO experiments of (-7.8±5.7 ‰; n = 9). (Chai and Hastings, 2018)(Fibiger et al., 2014)This trend of $\delta^{15}N$ values tracks with the initial measured or assumed $\delta^{15}N$ source value, in which $\delta^{15}N$ of the generated HONO (assumed to be -5.9±0.5 ‰) (Chai and Hastings, 2018) was higher than the measured NO_2 tank (-40.9±0.2 ‰; n = 3), and the NO tank (assumed to be -70.0 ±1.4 ‰) (Fibiger et al., 2014). This finding provides evidence that $\delta^{15}N$ can be used as a qualitative tracer to track NO_x emissions for sources with large differences in their emission $\delta^{15}N$ signatures. However, the experiments also demonstrate large $\delta^{15}N$ fractionation between the various NO_y species for each experiment and initial NO_y source. Overall, $\delta^{15}N(HNO_3)$ averaged -25.9±13.0 ‰ (n = 20) and was signficnatly higher than both $\delta^{15}N(NO_2)$ (-52.5 ±25.2 ‰; n = 20) and $\delta^{15}N(pNO_3)$ (-72.6±22.9 ‰; n = 7) based on a two-sample t test ($p < 0.01$). While $\delta^{15}N(NO_2)$ values were higher than those of $\delta^{15}N(pNO_3)$, this difference was not statistically significant based on a two-sample t test ($p > 0.05$). This trend suggests that the produced HNO_3 was generally associated with a positive isotope fractionation (ε) that favored the preferential formation of ^{15}N into HNO_3 relative to NO_2. This difference compared to HNO_3 provides support that the generated pNO_3 did not derive from HNO_3 and instead derived from another source such as organic nitrate. Conversely, the hydrolysis of pNO_3 is likely not a main contributor to HNO_3 due to their large $\delta^{15}N$ differences.

Overall, there were significant differences in the $\delta^{15}N$ of the various NO_y species ($p < 0.01$). Overall, $\delta^{15}N(HNO_3)$ that averaged -25.9±13.0‰ (n = 20) were higher than $\delta^{15}N(NO_2)$ that averaged -52.5 ±25.2‰ (n = 20), which were higher than $\delta^{15}N(pNO_3)$ that averaged -72.6±22.9‰ (n = 7). This trend suggests that the produced HNO_3 was associated with a positive isotope fractionation (ε) that favored the preferential formation of ^{15}N into HNO_3 relative to NO_2. We quantified the $\delta^{15}N$ enrichement of HNO_3 and pNO_3 relative to NO_2, as $\Delta\delta^{15}N$, (defined as $\delta^{15}N(product) - \delta^{15}N(NO_2)$) (Fig. 2B). Among the photochemical experiments initiated with NO and H_2O_2 (Exp 1-4), the average $\Delta\delta^{15}N(HNO_3\text{–}NO_2)$ was consistently high (value XX), while the HONO experiment (Exp. 5) deviated significantly with a much smaller enrichment (value). This difference is somewhat surprising, given that both systems likely involve NO_2 + OH as a major pathway for HNO_3 production. (Freyer et al., 1993)(Fang et al., 2021)Previous work has estimated a wide range of enrichment factors ($^{15}\varepsilon$) for this reaction: Freyer et al. calculated a small inverse isotope effect of -3 ‰ based on reduced mass assumptions, whereas more recent studies suggest a

large positive enrichment up to +40 ‰, attributed to equilibrium partitioning between NO_2 and an excited HNO_3^* intermediate. The low enrichment observed in the HONO experiment is more consistent with the former, while the higher values in the NO/H_2O_2 experiments support the latter interpretation. The cause of this discrepancy remains unclear but may reflect differences in reaction conditions or competing reaction pathways. In the nighttime experiment (Exp. 6), $\Delta\delta^{15}N(HNO_3\text{-}NO_2)$ was also elevated (+22.2 ‰), suggesting that even under nocturnal oxidation conditions, a positive enrichment in ^{15}N occurred. This may be due to isotopic effects associated with the $N_2O_5 \rightleftharpoons NO_2 + NO_3$ equilibrium(Walters and Michalski, 2016b). While N_2O_5 has been estimated to be enriched in ^{15}N by several per mil relative to NO_2, NO_3 is predicted to be depleted relative to NO_2. However, uncertainty remains in quantifying this equilibrium effect due to challenges in accurately modeling NO_3 vibrational frequencies (cite). In contrast, $\Delta\delta^{15}N(pNO_3\text{-}NO_2)$ values were consistently negative, averaging −13.6 ± 6.2 ‰ across experiments. These values suggest that pNO_3 formation involved reactions that preferentially excluded ^{15}N. One likely explanation is the influence of NO_2/NO equilibrium, which enriches NO_2 in ^{15}N relative to NO (Freyer et al., 1993; Li et al., 2020; Walters et al., 2016)(cite), followed by NO reactions with RO_2 to form RO_2NO_2 intermediates that carry a lower $\delta^{15}N$ signature. This kinetic isotope effect pathway likely drives the observed depletion in pNO_3 relative to NO_2.

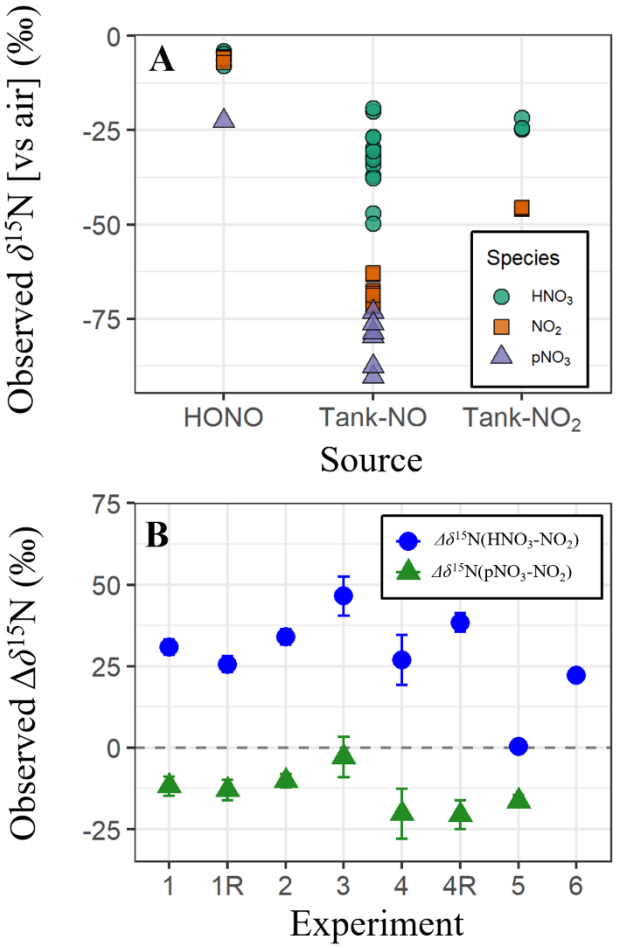

~~(Here talk about Dd15N).~~ ~~The isotope fractionation ($^{15}\alpha$) associated with NO_2 + OH has yet to be directly measured but has been precited in the literature with large differences in the suggested value. For example, $^{15}\alpha(NO_2+OH)$ has been suggested to be 0.997 based on the reduced masses of the transition complex (Freyer, 1991), while it has been predicted to be 1.040 in the i_NRACM mechanism based on the assumption that NO_2 and the excited HNO_3 intermediate formed during the NO_2 + OH reaction achieve isotopic equilibrium prior to collisional deactivation (Fang et al., 2021). The higher precited $^{15}\alpha(NO_2+OH)$ value of 1.040 would be consistent with the trend of elevated ^{15}N in HNO_3 relative to NO_2. The $\delta^{15}N(pNO_3)$ values were lower than $\delta^{15}N(NO_2)$. This difference compared to HNO_3 provides support that the generated pNO_3 did not derive from HNO_3 and~~

~~instead derived from another source such as organic nitrate. Conversely, the hydrolysis of pNO_3 is likely not a main contributor to HNO_3 due to their large $\delta^{15}N$ differences.~~ ~~The low $\delta^{15}N(pNO_3)$ values would reflect the influence of NO_x isotope exchange, which depletes NO in ^{15}N relative to NO_2 (Freyer et al., 1993; Li et al., 2020; Walters et al., 2016). The ^{15}N depleted NO can then react with α-pinene derived peroxy radicals leading to organic nitrate production with a low $\delta^{15}N$ value relative to $\delta^{15}N(NO_2)$. This trend in $\delta^{15}N(NO_y)$ followed all experiments except for the HONO experiments (Exp. 5), in which $\delta^{15}N(NO_2)$ (-5.8±1.8 ‰; n = 4) were insignificantly different from the $\delta^{15}N(HNO_3)$ (-6.2±0.7 ‰; n = 4) ($p>0.05$).~~

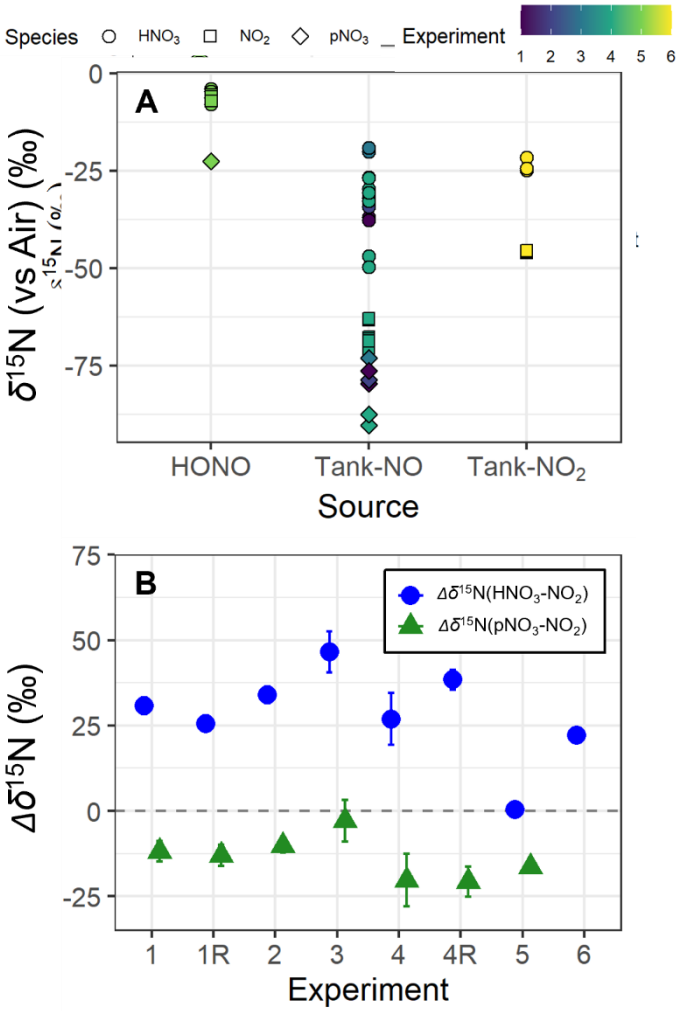

Fig. 2. (A) **The observed $\delta^{15}N$ of various NO_y species (i.e., HNO_3, NO_2, and pNO_3) collected during the various conducted α-pinene/NO_y oxidation experiments. The measured $\delta^{15}N$ were sorted by the various starting NO_y sources, including HONO (~~$\delta^{15}N$ = -5.9±0.5‰~~), tank-NO (~~$\delta^{15}N$ = -70.0±1.4‰~~), and tank-NO_2 (~~$\delta^{15}N$ = -40.9±0.2‰~~).** (B) **Calculated $\Delta\delta^{15}N$ values for each experiment, defined as the $\delta^{15}N$ difference between HNO_3 and NO_2, and between pNO_3 and NO_2. Data represent experiment-specific averages, with error bars reflecting the propagated standard deviation.**

3.2 Particle Nitrate Composition

The generated pNO_3 could have both inorganic (i.e., HNO_3 condensation) and organic (i.e., organic nitrate condensation) contributions. The $\delta^{15}N$ data qualitatively indicates that the pNO_3 derived from a separate source than HNO_3 due to their large $\delta^{15}N$ differences, which would suggest that pNO_3 was derived primarily from organic nitrate. For example, the observed $\delta^{15}N$ difference between HNO_3 and pNO_3 that averaged 46.7 ‰ suggests that these species may originate from distinct sources. Given that inorganic nitrate would typically equilibrate isotopically between HNO_3 and NO_3^- with an expected offset of only ~1–3 ‰, and often slightly enriched in pNO_3 (Bekker et al., 2023), the substantially lower $\delta^{15}N$ values observed in pNO_3 imply that the collected nitrate may originate from organic nitrate species or NO_y formation pathways unique from HNO_3 production.

We utilized the HR-ToF-AMS NO^+ and NO_2^+ data to evaluate the contributions of pNO_3 for the experiments. The $f(pNO_3, Org)$ was calculated according to Eq. 5 for each of the conducted experiments (Table 3). Overall, $f(pNO_3, Org)$ was calculated to have a mean of (1.25 ± 0.04; n=8), indicating that the generated pNO_3 derived from organic nitrate. The calculated $f(pNO_3, Org)$ was higher than 1 even when considering uncertainty estimates. This could be due to calculating R_{ON} values from reported R_{ON}/R_{AN} ratios from previously conducted α-pinene oxidation experimental conditions conducted utilizing substantially lower (~ ×10) initial precursor concentrations (Takeuchi and Ng, 2019). Thus, due to the potential uncertainty in our approach in estimating $f(pNO_3, Org)$, the composition of the generated pNO_3 was also investigated using a qualitative approach involving evaluating the relative change in the molar ratio of NH_4/SO_4 from the HR-ToF-AMS (Fig. S2). For each type of experiment, we found the NH_4/SO_4 molar ratio to be consistently near 1.5. This type of NH_4/SO_4 profile is consistent with the generated pNO_3 deriving from organic nitrate, as the dissolution of HNO_3 into aqueous aerosol followed by neutralization with available NH_3 would be expected to lead to an abrupt increase in the molar ratio of NH_4/SO_4 (Takeuchi and Ng, 2019). Furthermore, the acidic nature of the particles and limited availability of NH_4^+ likely inhibited HNO_3 uptake, suppressing condensation pathways and reinforcing the interpretation that pNO_3 originated predominantly from organic nitrate formation. Overall, both the quantitative and qualitative analysis of pNO_3 composition utilizing the AMS data as well as our $\delta^{15}N$ data indicates that pNO_3 was mainly derived from organic nitrate. Hereafter, we assume that the NO_3^- extracted from the filter collections derived from organic nitrate.

~~The generated pNO_3 could have both inorganic (i.e., HNO_3 condensation) and organic (i.e., organic nitrate condensation) contributions. The $\delta^{15}N$ data would qualitatively indicate that the pNO_3 appeared to derive from a separate source than HNO_3 due to their large $\delta^{15}N$ differences, suggesting that pNO_3 was derived primarily from organic nitrate. For example, the observed $\delta^{15}N$ difference between HNO_3 and pNO_3 that averaged 46.7 ‰ suggests that these species may originate from distinct sources. Given that inorganic nitrate would typically equilibrate isotopically between HNO_3 and NO_3^- with an expected offset of only ~1–3 ‰, and often slightly enriched in pNO_3 (Bekker et al., 2023), the substantially lower $\delta^{15}N$ values observed in pNO_3 imply that the collected nitrate may originate from organic nitrate species or NO_y formation pathways unique from HNO_3 production.~~

~~We also utilized the HR-ToF-AMS NO^+ and NO_2^+ data to evaluate the contributions of pNO_3 for the experiments. The $f(pNO_3, Org)$ was calculated according to Eq. 5 for each of the conducted experiments (Table 2). Overall, $f(pNO_3, Org)$ was calculated to have a mean of (1.25 ± 0.04; n=8), indicating that the generated pNO_3 derived from organic nitrate. The calculated $f(pNO_3, Org)$ was higher than 1 even when considering uncertainty estimates. This could be due to deriving calculating R_{ON} values from previously reported R_{ON}/R_{AN} ratios from previously conducted α pinene oxidation experimental conditions conducted utilizing substantially lower initial precursor concentrations by approximately a factor of 10 (Takeuchi and Ng, 2019). Thus, due to the potential uncertainty in our approach in estimating $f(pNO_3, Org)$, the composition of the generated pNO_3 was also investigated using a qualitative approach involving evaluating the relative change in the molar ratio of NH_4/SO_4 from the HR-ToF-AMS (Fig. S2). For each type of experiment, we found the NH_4/SO_4 molar ratio to be consistently near 1.5. This type of NH_4/SO_4 profile is consistent with the generated pNO_3 deriving from organic nitrate, as the dissolution of HNO_3 into aqueous aerosol followed by neutralization with available NH_3 would be expected to lead to an abrupt increase in the molar ratio of NH_4/SO_4 (Takeuchi and Ng, 2019).~~

~~Overall, both the quantitative and qualitative analysis of pNO_3 composition utilizing the AMS data as well as our $\delta^{15}N$ data indicates that pNO_3 was mainly derived from organic nitrate. Further, while gas-phase organic nitrates (e.g., $RONO_2$, RO_2NO_2) can be present and were detected by CIMS measurements, the strong agreement between filter-based and AMS-based pNO_3 measurements supports that the nitrate extracted from aerosol filters was primarily derived from particle-phase organic nitrate rather than from gas-phase organic nitrate contributions. Hereinafter, we will assume that the NO_3^- extracted from the filter collections derived from organic nitrate.~~

Table 3~~2~~. Summary of the HR-ToF-AMS data including NO^+/NO_2^+ fragmentation data (R_{obs}), calculated $f(pNO_3, Org)$~~,~~ maximum pNO_3 (Max(pNO_3)). Additionally, we quantified the amount of pNO_3 from the PILS (PILS/AMS) and the filter collection relative to the HR-ToF-AMS (Filter/AMS). Uncertainties for pNO_3 quantification and intercomparison ratios are reported in parentheses.

Exp.	R_{obs} ($\bar{x} \pm \sigma$)	$f(pNO_3, Org)$ ($\bar{x} \pm \sigma$)	Max(pNO_3) ($\mu g\ m^{-3}$) (±14 %)	PILS/AMS (%) (±24 %)	Filter/AMS (%) (±~~17~~24 %)
1	3.36 ± 0.30	1.26 ± 0.10	13.8	41.8	97.8
1R	3.16 ± 0.21	1.19 ± 0.08	13.3	37.8	83.5
2	3.36 ± 0.13	1.27 ± 0.05	25.9	33.2	105.3
3	3.32 ± 0.21	1.25 ± 0.09	27.4	NA	80.5
4	3.18 ± 0.32	1.20 ± 0.13	25.5	42.1	75.8
4R	3.40 ± 0.33	1.27 ± 0.14	15.0	NA	76.1

5	3.49 ± 0.25	1.31 ± 0.11	24.7	NA	59.5
6	5.63 ± 0.49	1.25 ± 0.11	38.6	NA	7.6

The pNO_3 measured by the HR-ToF-AMS indicated similar profiles for the various types of conducted experiments, in which pNO_3 concentrations peaked and subsequently decayed due to wall loss and chamber dilution (Fig. 3). Overall, the maximum pNO_3 concentrations ranged from 13.3 to 38.6 $\mu g\ m^{-3}$, depending on the experiment ~~across the various experiments~~ (Table ~~2~~3). The typical measurement uncertainty for pNO_3 quantification using the HR-ToF-AMS is approximately ±14 % (Bahreini et al., 2009; Takeuchi et al., 2024). Given that we assume 100% of the particulate nitrate is organic nitrate (i.e., f(pNO_3, Org) = 1, the uncertainty in pNO_3 concentration is based solely on the AMS nitrate measurement error, estimated at ±14 %. The lowest maximum pNO_3 ~~3~~ corresponded to ~~the~~ experimental conditions with low initial NO_x relative to H_2O_2 and BVOC conditions (i.e., Exp 1). In contrast, the highest maximum pNO_3 occurred during the nighttime oxidation experiments (i.e., Exp 6). The pNO_3 concentrations determined from the HR-ToF-AMS were compared with additional measurement techniques, including the PILS and the filter collections for offline analysis (Fig. 3; Table 2). The PILS pNO_3 measurements were available for 4 out of the 8 conducted experiments and indicated a similar time profile as the HR-ToF-AMS; however, the PILS pNO_3 observations were always lower than the HR-TOF-AMS with the amount of pNO_3 determined from PILS relative to the HR-ToF-AMS (PILS/AMS) ranging between 33.2 % to 53.8 %. The uncertainty associated with pNO_3 quantification by the PILS system is approximately ±20 % (Guo et al., 2016). Accordingly, the propagated uncertainty for the PILS/AMS ratio is approximately 24 ~~‰~~%.

~~.~~The pNO_3 quantified using filter collection and extraction technique was higher than the PILS and in closer agreement with the HR-ToF-AMS ~~for most of the photochemical experiments~~. For the photochemical experiments (Exp. 1-5), the pNO_3 determined using the filter collection relative to the HR-ToF-AMS (Filter/AMS) for the photochemical experiments ranged between 59.5 to 105.3 % and averaged 86.5 ± 12.~~35~~4 % (*n*=7). The filter collection technique has an estimated uncertainty for pNO_3 quantification of approximately ±~~1~~20 %, based on the average ~~relative~~percent difference ~~standard deviations~~ from side-by-side ChemComb filter pack measurements of ambient air using Nylon filters (Blum et al., 2020). Although different filters were used in this study, the same collection system and mass flow controllers were employed, and we therefore expect a comparable difference between system replicates. Accordingly, the propagated uncertainty for the Filter/AMS ratio of ±~~17~~24 %.~~,~~ However, the filter collection resulted in nearly negligible pNO_3 for the nighttime oxidation experiments (i.e., Exp. 6).

~~The pNO_3 concentrations determined using the PILS were always lower than that determined by the HR-ToF-AMS and the offline filter collection technique, which would indicate that that not all the collected pNO_3, which were shown to mainly derive from organic nitrate, were hydrolyzed to $NO_3^-{}_{(aq)}$ within the PILS chamber before quantification via Ion Chromatography. The filter collection and extraction method (i.e., leach in MQ water for 1 week), enabled the successful~~

hydrolysis of the collected pNO_3 to $NO_3^-_{(aq)}$ from the photochemical experiments, an important pre-requisite for subsequent isotope analysis. The filter collection technique, however, resulted in near negligible pNO_3 for the nighttime oxidation experiments, limiting our ability to measure the isotope composition of pNO_3 from this experiment. This difference in the efficacy of the offline filter collection technique for pNO_3 characterization between the photochemical and nighttime oxidation experiments could be related to the type of organic nitrate formed during the conducted experiments. The photochemical α-pinene oxidation experiments have been suggested to result in higher relative production of tertiary organic nitrate, while nighttime oxidation leads to a relatively lower fraction of tertiary organic nitrate with estimated values of 62 % and 15 %, respectively (Zare et al., 2018). Recent work has suggested a hydrolysis lifetime of no more than 30 minutes and a hydrolyzable portion of particulate organic nitrate from α pinene oxidation experiments between 23–32 % and 9–17 % for α pinene + OH and α pinene + NO_3 reactions, respectively (Takeuchi and Ng, 2019).

The offline filter collection and extraction technique follows the observed trend of a greater proportion of pNO_3 hydrolyzed to $NO_3^-_{(aq)}$ in photochemical experiments (82.6 ± 14 %; n = 7) compared to nighttime conditions (7.6 %; n = 1). This is inferred based on the relative amount of quantified $NO_3^-_{(aq)}$ from the filter extraction solution to the total pNO_3 measured by HR-ToF-AMS. However, the filter-based method suggests a higher proportion of potentially hydrolyzable pNO_3 in the photochemical experiments than previously reported estimates The offline filter collection and extraction technique matches the trend in which more pNO_3 hydrolyzed for the photochemical experiments compared to the nighttime; however, the filter technique would indicate a higher proportion of potential hydrolysable pNO_3 from photochemical experiment than these previous estimates, though with a different timescale. From these results and comparisons, we speculate conclude that the pNO_3 offline filter measurements to encompass the hydrolysable portion of pNO_3 within a week (as the filter samples were extracted and leached in MQ for at least one week), while the HR-ToF-AMS measurements represent the total pNO_3, and the PILS measurements correspond to the readily hydrolysable portion of pNO_3. Further, the box model simulations of organic nitrate speciation indicate that the nighttime organic nitrate was dominated by the formation of dimer, pinene dinitrate, as well as secondary hydroxyl nitrate (Fig. S3). If this speciation is correct, the results imply that these organic nitrate compounds are effectively non-hydrolyzable under aqueous conditions. If this speciation is correct, the results would suggest that these types of organic nitrate were not readily hydrolysable.

Our results demonstrate that organic nitrate aerosols ($pRONO_2$) can hydrolyze and contribute to the NO_3^- measured in aerosol extracts. While our chamber experiments were conducted under controlled conditions with relatively low relative humidity (~30 %) and dry aerosol seeds, they highlight the need to consider that NO_3^- collected on filters may originate from both inorganic nitrate (derived from HNO_3 uptake) and hydrolyzed organic nitrate. However, we caution that these findings do not imply that all pNO_3 observed in ambient field measurements is organic in origin. Further, while gas-phase organic nitrates (e.g., $RONO_2$, RO_2NO_2) can be present and were detected by CIMS measurements, the strong agreement between filter-based and AMS-based pNO_3 measurements supports that the nitrate extracted from aerosol filters was primarily derived from

~~particle-phase organic nitrate rather than from gas-phase organic nitrate contributions. (Li et al., 2020; Walters et al., 2016)~~The pNO_3 concentrations determined using the PILS were always lower than that determined by the HR-ToF-AMS and the offline filter collection technique, which would indicate that that not all collected pNO_3, which were shown to mainly derive from organic nitrate, were hydrolyzed to $NO_3^-_{(aq)}$ within the PILS chamber before quantification via Ion Chromatography. The filter collection and extraction method (i.e., leach in MQ water for 1 week), enabled the successful hydrolysis of the collected pNO_3 to $NO_3^-_{(aq)}$ from the photochemical experiments, an important pre-requisite for subsequent isotope analysis. The filter collection technique, however, resulted in near negligible pNO_3 for the nighttime oxidation experiments, limiting our ability to measure the isotope composition of pNO_3 from this experiment. This difference in the efficacy of the offline filter collection technique for pNO_3 characterization between the photochemical and nighttime oxidation experiments could be related to the type of organic nitrate formed during the conducted experiments. The photochemical α-pinene oxidation experiments have been suggested to result in higher relative production of tertiary organic nitrate, while nighttime oxidation leads to a relatively lower fraction of tertiary organic nitrate with estimated values of 62 % and 15 %, respectively (Zare et al., 2018). Recent work has suggested a hydrolysis lifetime of no more than 30 minutes and a hydrolyzable portion of particulate organic nitrate from α-pinene oxidation experiments between 23-32 % and 9-17 % for α-pinene + OH and α-pinene + NO_3 reactions, respectively (Takeuchi and Ng, 2019).

The offline filter collection and extraction technique follows the observed trend of a greater proportion of pNO_3 hydrolyzed to $NO_3^-_{(aq)}$ in photochemical experiments (82.6 ± 14 %; n = 7) compared to nighttime conditions (7.6 %; n = 1). This is inferred based on the relative amount of quantified $NO_3^-_{(aq)}$ from the filter extraction solution to the total pNO_3 measured by HR-ToF-AMS. However, the filter-based method suggested a higher proportion of potentially hydrolyzable pNO_3 in the photochemical experiments than previously reported estimates. From these results and comparisons, we conclude that the pNO_3 offline filter measurements encompass the hydrolysable portion of pNO_3 within 1 week, while the HR-ToF-AMS measurements represent the total pNO_3, and the PILS measurements correspond to the readily hydrolysable portion of pNO_3. Further, the box model simulations (see below) of organic nitrate speciation indicate that the nighttime organic nitrate had a high fraction of dimer and pinene dinitrate (Fig. S3). If this assignment is correct, the results imply that these organic nitrate compounds are effectively non-hydrolyzable under aqueous conditions.

Our results demonstrated that organic nitrate aerosols ($pRONO_2$) can hydrolyze and contribute to the NO_3^- measured in aerosol extracts. While our chamber experiments were conducted under controlled conditions with low relative humidity (~30 %) and dry aerosol seeds, they highlight the need to consider that NO_3^- collected on filters may originate from both inorganic nitrate (derived from HNO_3 uptake) and hydrolyzed organic nitrate. However, we caution that these findings do not imply that all pNO_3 observed in ambient field measurements is organic in origin. The extent to which organic nitrate contributes to pNO_3 in field settings will depend on regional BVOC emissions, which govern precursor availability, as well as environmental factors such as aerosol pH and relative humidity, which influence the lifetime and hydrolysis rates of $pRONO_2$ prior to filter collection.

Further, while gas-phase organic nitrates (e.g., $RONO_2$, RO_2NO_2) can be present and were detected by CIMS measurements during the experiments, the strong agreement between filter-based and AMS-based pNO_3 measurements supports that the nitrate extracted from aerosol filters was primarily derived from particle-phase organic nitrate rather than from gas-phase organic nitrate contributions. Finally, given that the collected pNO_3 was predominantly derived from $RONO_2$, the negative $\Delta\delta^{15}N(pNO_3 - NO_2)$ values (Fig. 2B) suggest a preferential incorporation of ^{14}N into the $RONO_2$ product. This is consistent with a NO_x photochemical equilibrium in which ^{15}N is enriched in NO_2, leaving NO relatively depleted in ^{15}N (Li et al., 2020; Walters et al., 2016). Subsequent reaction of this ^{15}N-depleted NO with RO_2 forms $RONO_2$, thereby transferring the isotopically lighter nitrogen signature into $RONO_2$ that then condenses to the particle phase and is hydrolyzed to NO_3^-.

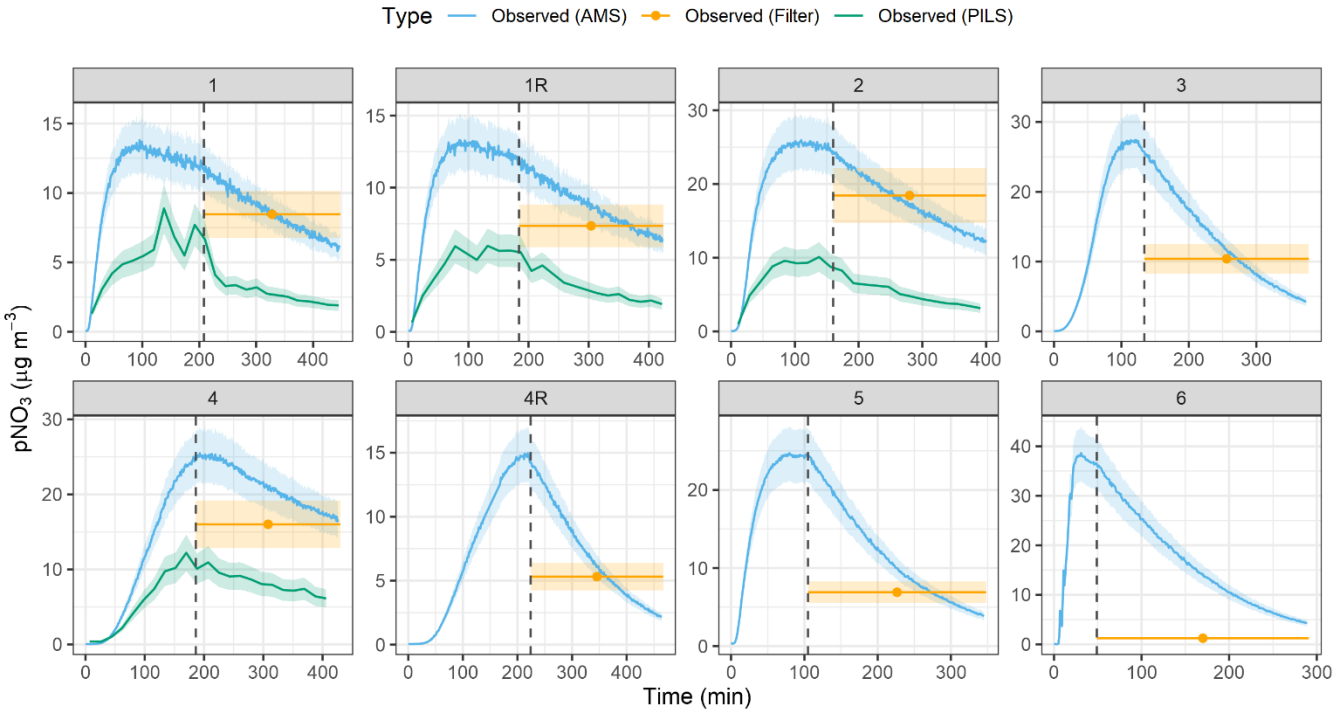

~~The extent of $pRONO_2$ hydrolysis in the atmosphere will depend on environmental factors such as aerosol liquid water content, relative humidity, and aerosol acidity.~~

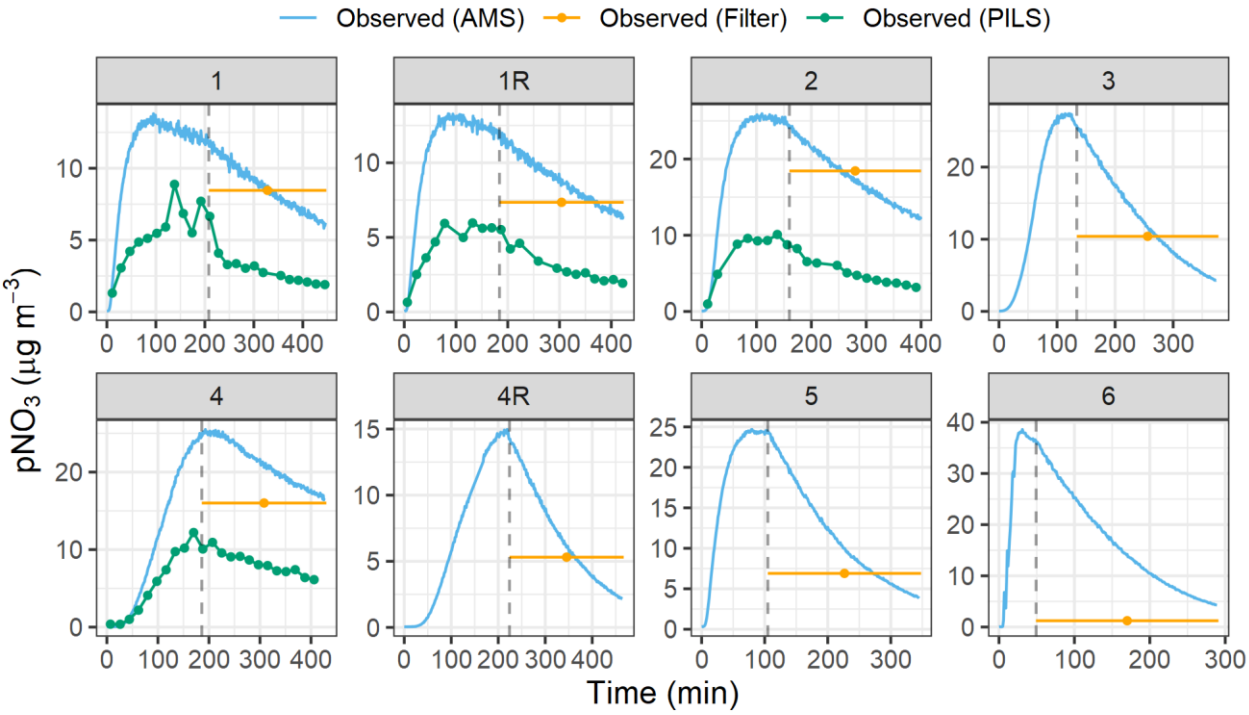
Observed (AMS)
Observed (Filter)
Observed (PILS)
1
1R
2
3
4
4R
5
6
pNO3 (μg m−3)
Time (min)

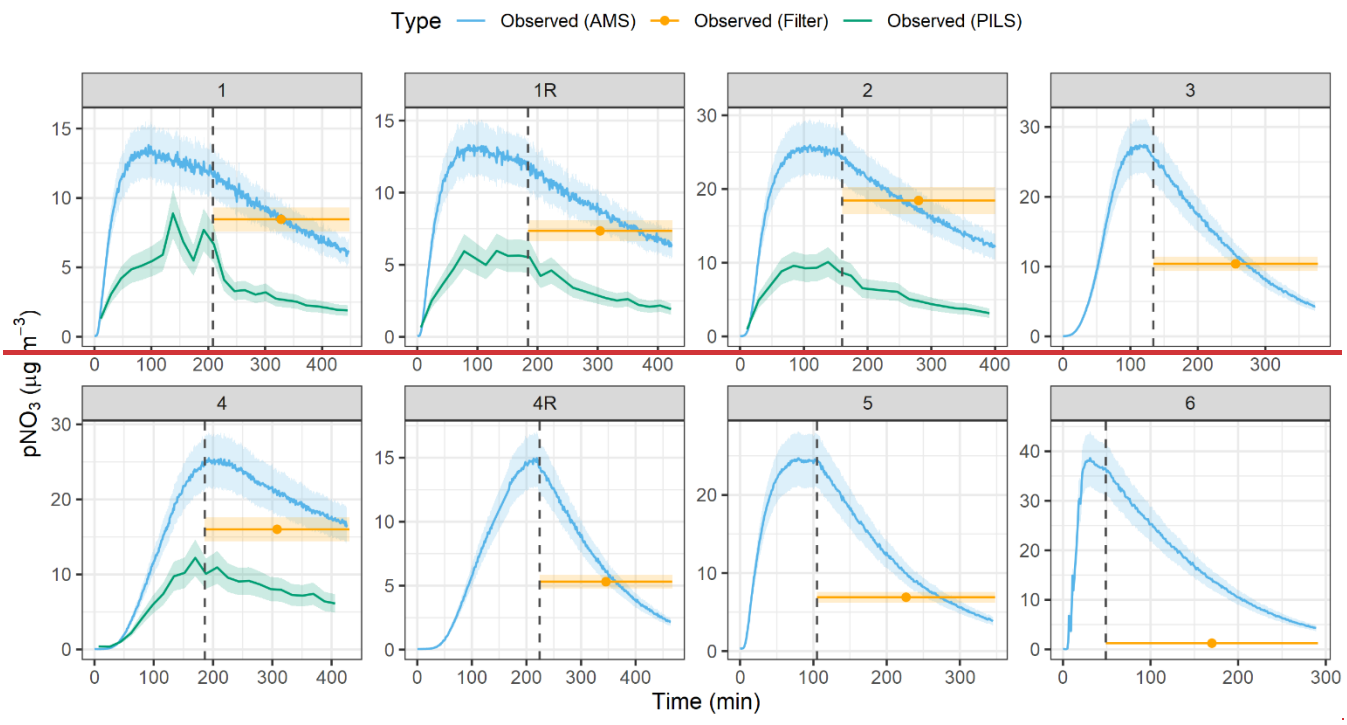
Type
Observed (AMS)
Observed (Filter)
Observed (PILS)
1
1R
2
3
4
4R
5
6
pNO3 (μg m−3)
Time (min)

Fig. 3. The observed pNO_3 concentration data are shown for each of the conducted experiments. Concentrations were determined using a High-Resolution Time-of-Flight Aerosol Mass Spectrometer (HR-ToF-AMS), a particle-into-liquid sampler (PILS), and filter collection (Filter). The start of chamber dilution is indicated by the dashed vertical lines, corresponding to the abrupt decrease in pNO_3. The lighter shaded regions correspond to the measurement uncertainty for the various analytical techniques.

~~The observed pNO_3 concentration data are shown for each of the conducted experiments. Concentrations were determined using a High-Resolution Time-of-Flight Aerosol Mass Spectrometer (HR-ToF-AMS), a particle-into-liquid sampler (PILS), and filter collection (Filter). The start of chamber dilution is indicated by the dashed vertical lines, corresponding to the abrupt decrease in pNO_3. The lighter colored shaded region corresponds to the measurement uncertainty for the various analytical techniques. The observed pNO3 concentrations are faceted by the various experiments conducted. The concentrations were determined using the High-Resolution Time-of-Flight Aerosol Mass Spectrometer (HR-ToF-AMS), particle-into-liquid sampler (PILS), and filter collection (Filter). The start of the chamber dilution is indicated by the dashed vertical lines, corresponding to the abrupt decrease in pNO_3.~~

3.3 Model Simulations

To further interpret the experimental results, we employed a box model to simulate the formation and evolution of NO_y species and their $\Delta^{17}O$ values. We begin by examining the developed gas-phase chemical mechanism (NO_x-API) simulation of the initial aerosol precursor decay including α-pinene and NO. For comparison, simulations were also conducted using established gas-phase chemical mechanisms that included RACM2 and the MCM to evaluate the treatment of α-pinene oxidation and ~~organic nitrate formation~~oxidation chemistry across different chemical frameworks for a range of experimental conditions. Model sensitivity tests were then conducted to assess the impact of key physical parameters that included chamber dilution rate and wall loss rates on simulated $\Delta^{17}O$ values. Finally, we compare the modeled $\Delta^{17}O$ values of NO_y species with experimental observations to evaluate the model's ability to reproduce isotopic values under different photochemical and nighttime oxidation conditions.

3.3.1 Precursor Decay

Box model simulations were conducted to evaluate the oxidation and decay of precursors used in the experiments, ensuring that the correct amount of oxidant was accurately simulated. ~~For all the photochemical experiments, the box model utilizing~~The MCM, RACM2, and NO_x-API chemical ~~the USC API~~ mechanisms were used to ~~was able to well simulate the~~simulate the decay of α-pinene and NO, with results compared against experimental observations (Fig. 4-5). Model performance was evaluated by comparing measured and modeled concentrations of NO and α-pinene using one-to-one plots, with corresponding R^2 values and quantification of model biases (Figs. S4–S5) and Table 4 summarizes these results. ~~The model fit for α-pinene decay using the NO_x-API mechanism had an average R^2 of 0.97±0.03 with an average absolute residual of for all experiments 8.6±3.8 ppb (Fig. SX). For NO decay, the NO_x (Fig. 4-5). ThAPI mechanism had an average R^2 of 0.97±0.03, with an average absolute residual of 9.6 ±10.7 ppb (Fig. SX). Comparatively, the MCM mechanism had slightly lower performance, with an average R^2 of 0.84±0.19 for α-pinene (average absolute residual: 21.7±12.9 ppb) and had an average R^2 of 0.86±0.21 for NO (average absolute residual: 21.2±24.4 ppb). The RACM2 mechanism also showed slightly weaker performance with an average~~

~~R^2 of 0.89±0.16 for α-pinene (average absolute residual: 17.7±13.5 ppb) and had an average R^2 of 0.92±0.03 for NO (average absolute residual: 17.6±23.9 ppb). Experiment 6 (nighttime oxidation) was excluded from the NO model measurement comparison because NO was not used as an initial reactant in that experiment.~~ Overall, the NO_x-API mechanism provided improved model performance, evidenced consistently higher R^2 values (averaging 0.97 ±0.03) and lower absolute residuals for both α-pinene and NO decay compared to the other mechanisms~~y~~. ~~is comparison indicates that the developed mechanism well represents the oxidation of α pinene and formation of oxidants under a wide range of experimental conditions. The simulations using the USC API mechanism was a vast improvement compared to using the RACM2 or the MCM subset for α pinene chemistry for simulating NO and α pinene decay for the photochemical experiments (Exp. 1-5).~~ We attribute this enhanced model performance to the simplified treatment of higher-generation products in the NO_x-API mechanism. Unlike MCM and RACM2, which allow continued gas-phase reactions of all products through extensive reaction propagation, the NO_x-API mechanism terminates the chemistry of these products after a limited number of steps. ~~which allow continued gas-phase reactions of secondary and tertiary products, the NO_x-API mechanism does not propagate these products.~~ Given that the box-model ~~simulates~~simulations do~~es~~ not include an explicit aerosol-phase treatment, continued gas-phase reactivity of condensable species (as implemented in MCM and RACM2) may unrealistically ~~distribute~~disrupt the oxidant budget. Therefore, the NO_x-API mechanism as employed in the box model is better aligned with the experimental design and will be used for subsequent $\Delta^{17}O$ simulations of the chamber experiments.

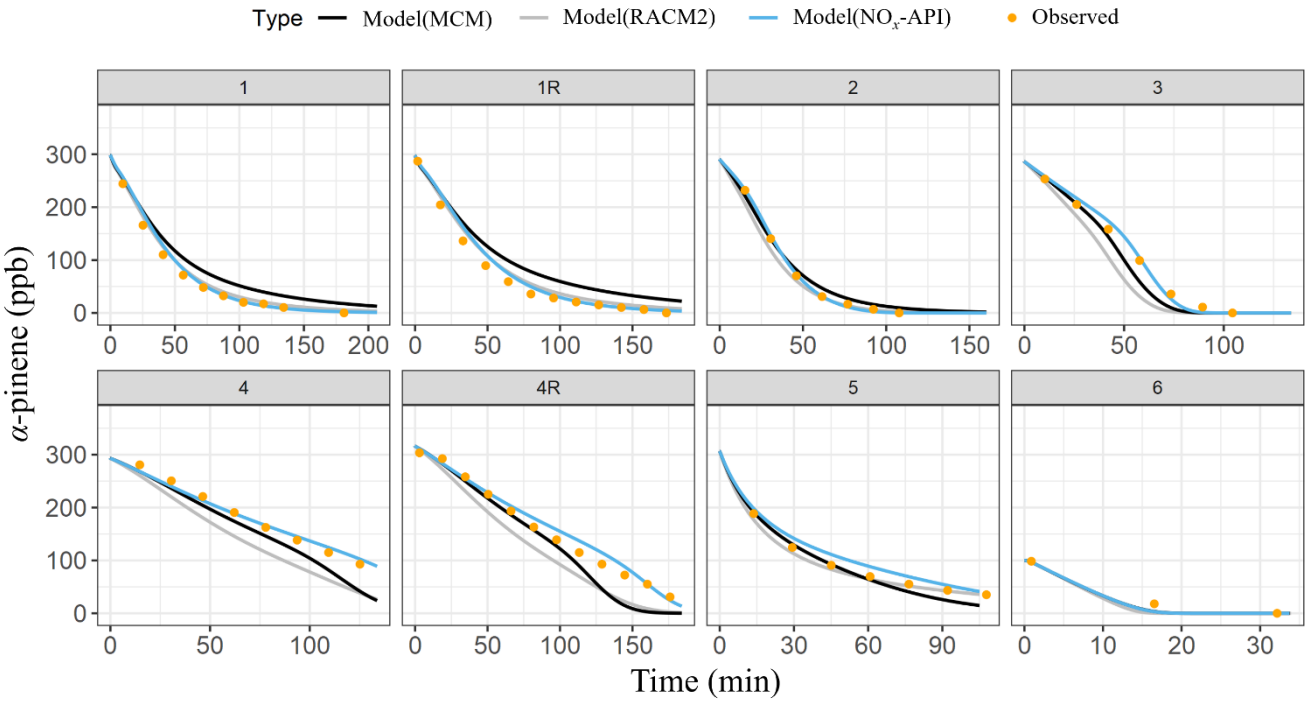
Type
Model(MCM)
Model(RACM2)
Model(NOx-API)
Observed
1
1R
2
3
4
4R
5
6
α-pinene (ppb)
Time (min)

955

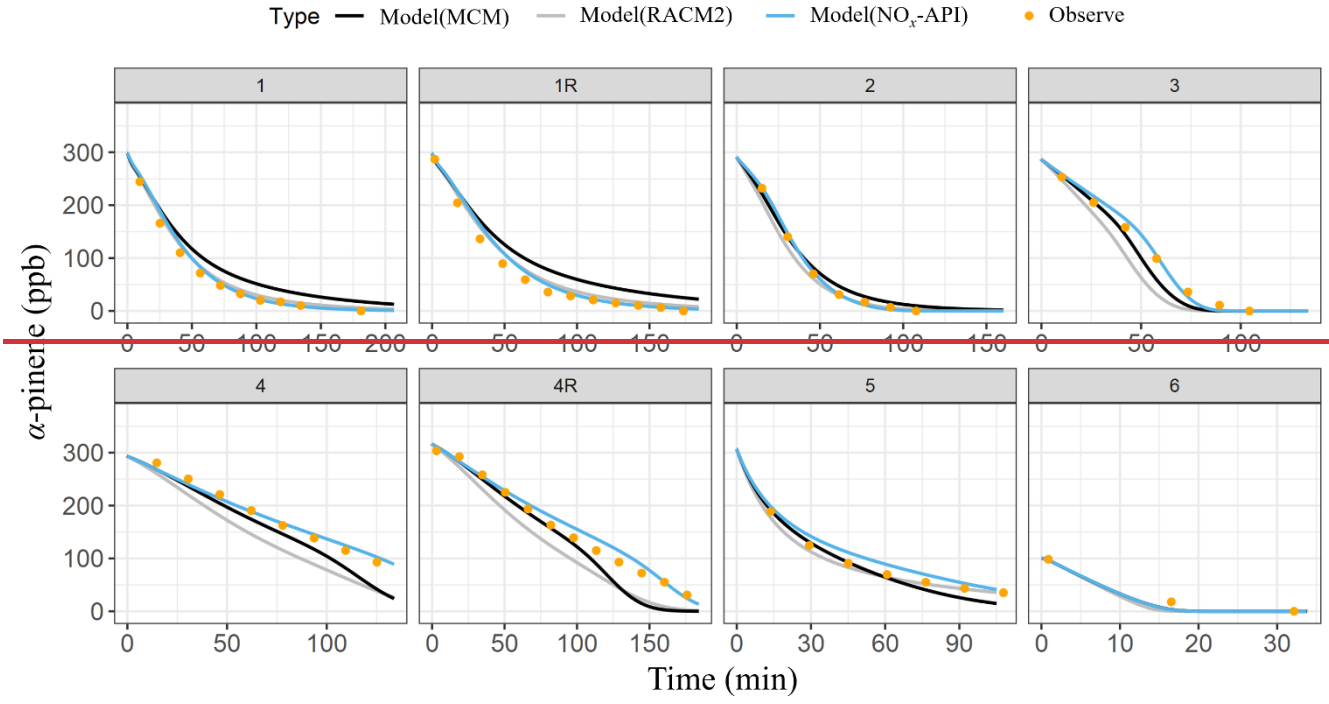
Type
Model(MCM)
Model(RACM2)
Model(NOx-API)
Observe
1
1R
2
3
4
4R
5
6
α-pinene (ppb)
Time (min)

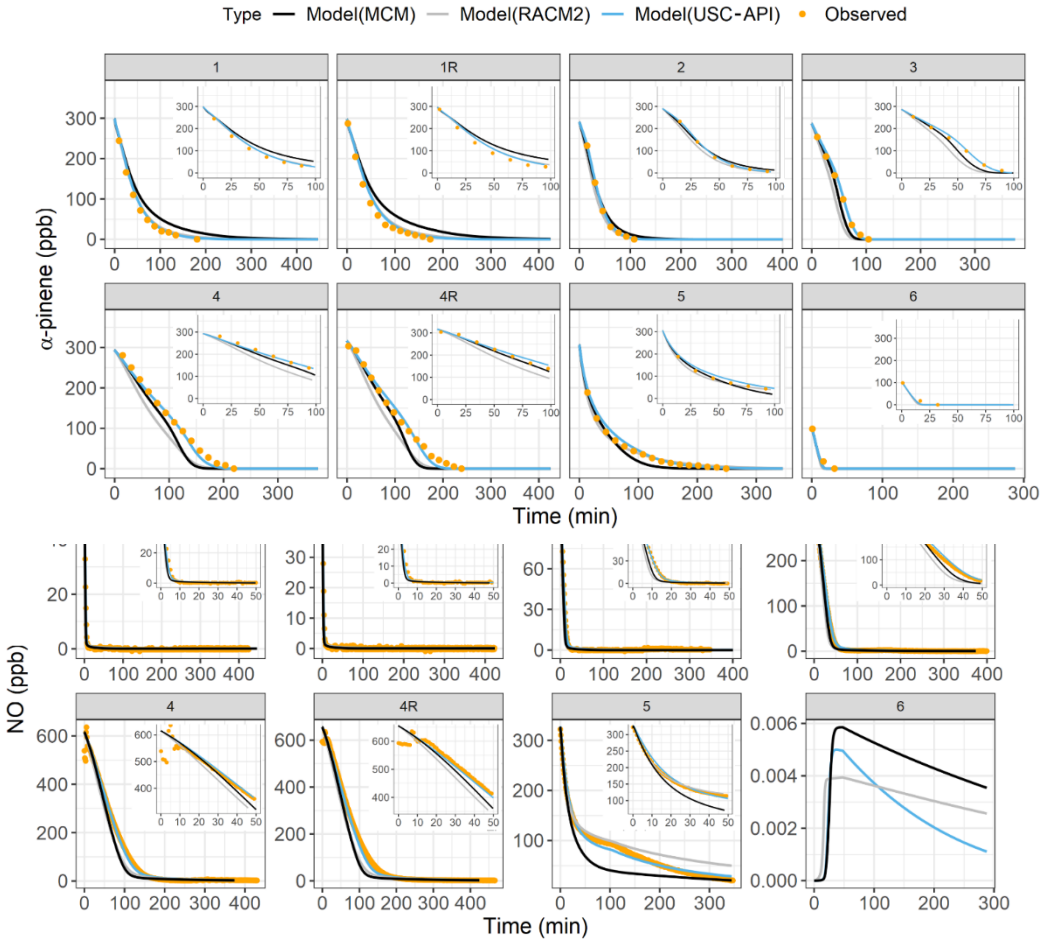

Fig. 4. The observed (orange data points) and the modeled (lines) *α*-pinene decay for the various conducted experiments. The modeled results are based on three chemical mechanisms: MCM (black), RACM2 (grey), and ~~USC~~NO_x-API (light blue). ~~Insets highlight the initial decay period from 0 to 100 minutes.~~

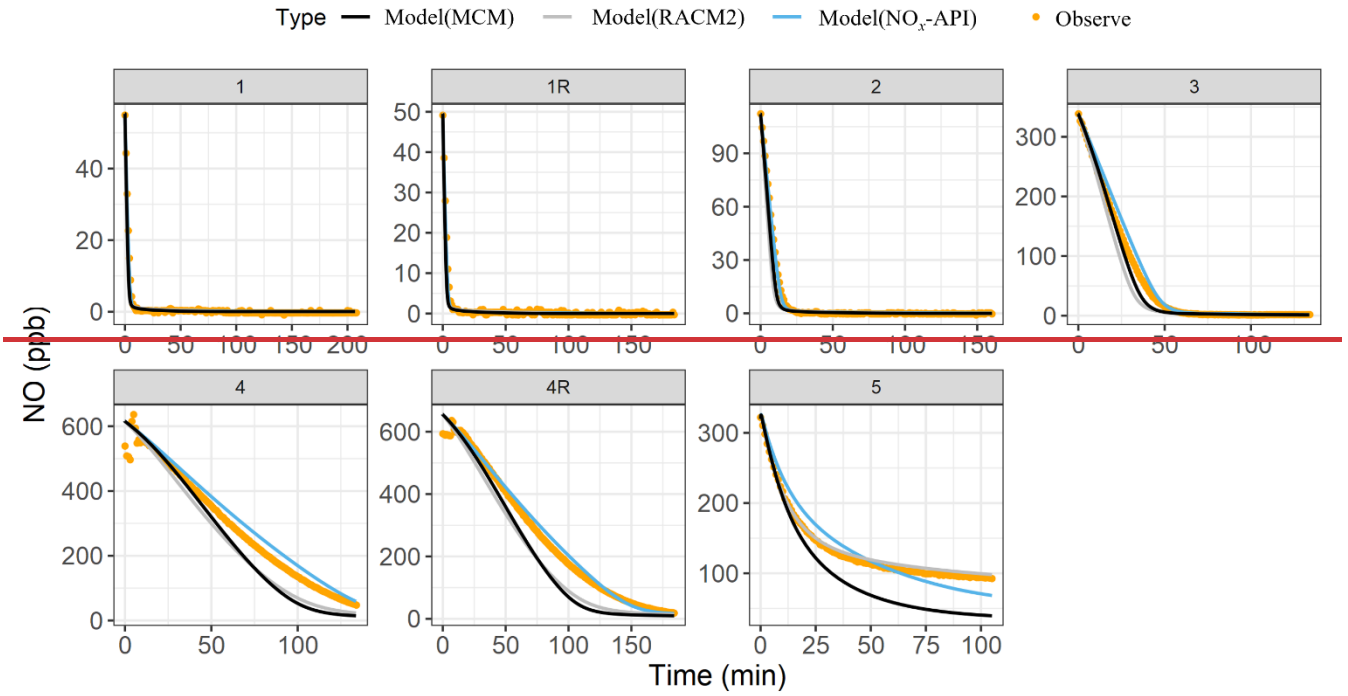
Type
Model(MCM)
Model(RACM2)
Model(NOx-API)
Observe
1
1R
2
3
4
4R
5
NO (ppb)
Time (min)

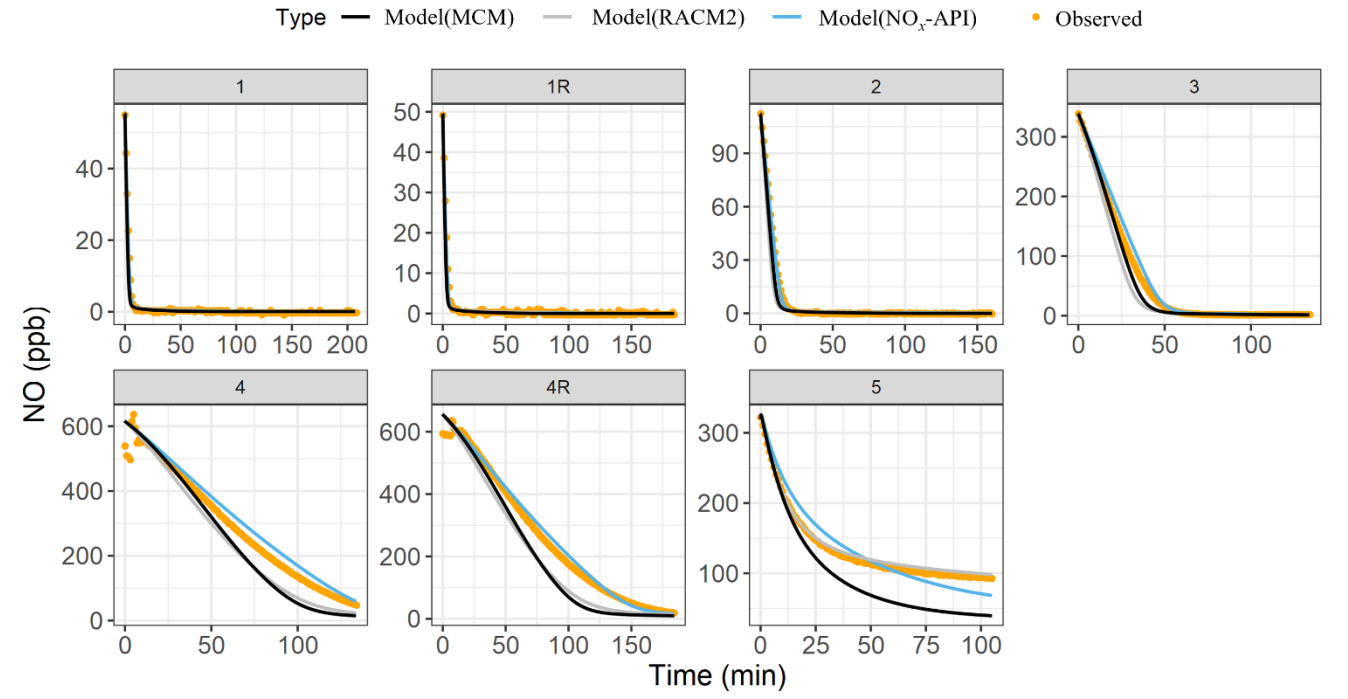
Type
Model(MCM)
Model(RACM2)
Model(NOx-API)
Observed
1
1R
2
3
4
4R
5
NO (ppb)
Time (min)

Fig. 5. The observed (orange data points) and the modeled (lines) NO decay for the various conducted photochemical experiments. ~~The NO observations for Experiment 6 were not available.~~ The modeled results are based on three chemical mechanisms: MCM (black), RACM2 (grey), and ~~USC~~NO$_x$-API (light blue). Experiment 6 (nighttime oxidation) was omitted from the analysis as NO was not among the initial reactants.

~~**Insets highlight the initial decay period from 0 to 50 minutes.**~~

Table 4. Summary of model performance for α-pinene and NO using the NO$_x$-API, RACM2, and MCM mechanisms. Values represent the average coefficient of determination (R^2) and average mean residuals (in ppb) across all experiments, with associated standard deviations.

Mechanism	α-pinene		NO	
	Average R^2	Average Mean Residual (ppb)	Average R^2	Average Mean Residual (ppb)
NO$_x$-API	0.97 ± 0.03	8.6 ± 3.8	0.97 ± 0.03	9.6 ± 10.7
RACM2	0.89 ± 0.16	17.7 ± 13.5	0.92 ± 0.03	17.6 ± 23.9
MCM	0.84 ± 0.19	21.7 ± 12.9	0.86 ± 0.21	21.2 ± 24.4

3.3.2 Δ^{17}O Model Sensitivity to Dilution and Wall Loss~~Model Sensitivity Tests~~

Before comparing modeled Δ^{17}O values to observations, we first evaluated the model's sensitivity to our treatment of key physical parameters, including chamber dilution and wall loss, and their potential impact on the simulated Δ^{17}O (Fig. 6). These sensitivity tests focused on Experiment 1, one of the longest-duration experiment, where dilution and wall loss would be expected to exert the strongest influence on gas-phase chemistry and Δ^{17}O values.

The impact of chamber dilution was assessed using four scenarios: no dilution, and first-order dilution rate constants (k_{dil}) of 1×10^{-5}, 5×10^{-5}, and 1×10^{-4} s^{-1} (Fig. 6A). Dilution was initiated at t = 208 minutes in the model to match the experimental protocol. Across all scenarios, simulated Δ^{17}O of the total organic nitrate (ONIT = ONITa + ONITb + ONITc + ONITOOHa + ONITOOHb + DIMER + PDN) values were minimally impacted by dilution. For instance, Δ^{17}O(ONIT) varied by only 0.06 ‰ between the no-dilution and highest dilution rate constant scenario (k_{dil} = 1×10^{-4} s^{-1}), corresponding to a relative difference of −1.1 %. This insensitivity reflects the fact that organic nitrate chemistry was largely completed by the time dilution began. In contrast, simulated Δ^{17}O values for HNO_3 and NO_2 were more sensitive to the dilution rate. Between the no-dilution and lowest dilution rate constant scenario (k_{dil} = 1×10^{-5} s^{-1}), Δ^{17}O(HNO_3) and Δ^{17}O(NO_2) changed by only -0.01 ‰ (corresponding to a relative difference of −0.2 %) and −0.11 ‰ (-0.7 %), respectively. However, increasing the dilution rate constant from 1

× 10^{-5} to 5 × 10^{-5} s^{-1} led to additional decreases of 0.32 ‰ (−5.0 %) for HNO_3 and 0.88 ‰ (−5.6 %) for NO_2. The most extreme dilution rate constant scenario (k_{dil} = 1 × 10^{-4} s^{-1}) reduced $\Delta^{17}O$ by a total of 0.50 ‰ (−7.9 %) for HNO_3 and 1.62 ‰ (−10.3 %) for NO_2 relative to the no-dilution case. For the main box model simulations, we adopted a dilution rate constant of 3.47 × 10^{-5} s^{-1}, corresponding to a measured flow rate of 25 LPM in a 12 m^3 chamber. Assuming no more than ±20 % uncertainty in the actual flow rate, we estimate that the resulting uncertainty in simulated $\Delta^{17}O$ values due to dilution would be approximately ±2.5 % for HNO_3, ±3 % for NO_2, and less than ±1 % for ONIT. These estimates are based on the observed $\Delta^{17}O$ variation between the 1 × 10^{-5} and 5 × 10^{-5} s^{-1} scenarios.

Next, we evaluated the potential influence of chamber wall loss on the simulated $\Delta^{17}O$ values (Fig. 6B). Three scenarios were tested: (1) no wall loss, (2) a wall loss scenario incorporating NO_y and O_3 loss rates from previous studies (Morales et al., 2021; Wang et al., 2014), and (3) an extreme case in which wall loss rate constants were increased by a factor of 10 (Table S7). In the base comparison between the no-wall-loss and reported wall loss scenario, the effect on modeled $\Delta^{17}O$ values was minimal. Specifically, $\Delta^{17}O$ changed by -0.02 ‰ for HNO_3 (-0.3 %), -0.37 ‰ for NO_2 (-2.3 %), and +0.03 ‰ for ONIT (+0.5 %). These small differences suggest that moderate wall loss rates, consistent with literature values, would not substantially alter the $\Delta^{17}O$ simulations. However, the extreme wall loss scenario revealed a much stronger impact. In this case, $\Delta^{17}O$ decreased by 2.5 ‰ for NO_2 (-15.8 %) and increased by 0.50 ‰ for HNO_3 (+7.8 %) and 0.69 ‰ for ONIT (+11.4 %) relative to the no-wall-loss case. The drop in $\Delta^{17}O(NO_2)$ arises from the altered oxidant concentrations and rapid photochemical cycling of NO_x, which can reset its $\Delta^{17}O$ values on short timescales. Conversely, the rise in $\Delta^{17}O$ for HNO_3 and ONIT reflects preferential removal of early-formed products with lower $\Delta^{17}O$, allowing later-formed, products with higher $\Delta^{17}O$ values to dominate. Because we lacked experimental constraints on wall loss during the chamber experiments, the box model simulations presented in this study did not include wall loss. Based on our sensitivity analysis, omitting wall loss introduces an estimated uncertainty of ±0.3 % for HNO_3, ±2.3 % for NO_2, and ±0.5 % for ONIT assuming moderate wall loss scenario. If actual wall loss rates in the chamber were significantly higher than those reported in the literature, the model is anticipated to overestimate $\Delta^{17}O$ in NO_2 and underestimate it in HNO_3 and ONIT.

~~The impact of the parameterization of physical processed impacting the simulated $\Delta^{17}O$ values were first evaluated from a series of sensitivity test focsed on chamber dilution and wall loss. The impact of dilution rate was assessed through sensitivity tests using three dilution scenarios with varying dilution rate coefficients (k_{dil} = 1×10^{-5} s^{-1}, 5×10^{-5} s^{-1}, and 1×10^{-4} s^{-1}) to evaluate changes $\Delta^{17}O$ values for Exp. 1 conditions (Fig. 6).~~

~~The HNO_3 concentrations exhibiting relative mean biases of +8.6 %, +28.5 %, and +48.9 % for the 1×10^{-5} s^{-1}, 5×10^{-5} s^{-1}, and 1×10^{-4} s^{-1} k_{dil} scenarios relative to X?, respectively (Fig. SX). The maximum relative mean bias for $\Delta^{17}O$ across NO_2, HNO_3, and pNO_3 was +1.8 % at 1×10^{-5} s^{-1}, increasing to +8.0 % at 1×10^{-4} s^{-1} (Fig. SX).~~

~~HNO_3 concentrations were highly sensitive to chamber loss, with relative mean biases of -10 % considering the base wall loss and -49 % under wall loss ×10 scenarios (Fig. SX). The maximum relative mean bias observed for $\Delta^{17}O$ was +2.3 % under base wall loss and +7.2% under wall loss ×10 scenarios (Fig. SX).~~ Overall, based on the results of the model sensitivity tests, we estimate that the propagated uncertainty in the simulated $\Delta^{17}O$ values due to chamber dilution and wall loss is approximately ±2.5 % for HNO_3, ±3.8 % for NO_2, and ±1.1 % for ONIT. These values reflect the combined effects of plausible variation in dilution rate (±20 %) and the difference in simulated $\Delta^{17}O$ values from literature-based estimates of NO_y and O_3 wall loss compared to a case of no wall loss. Further, considering the uncertainty in the measured $\Delta^{17}O(O_3^{term})$ is approximately ±5 % (Vicars and Savarino, 2014), we calculate an overall model uncertainty of $\Delta^{17}O$ of ±5.6 %, ±6.3 %, and ±5.1 % for HNO_3, NO_2, and ONIT, respectively. Clearly, the uncertainty in the $\Delta^{17}O(O_3^{term})$ is expected to be the largest source of uncertainty in the modeled $\Delta^{17}O$ values as opposed to our treatment of dilution and chamber wall loss. Still, we conservatively apply these propagated uncertainty estimates when presenting and interpreting the model results. ~~Overall, while HNO_3 concentrations were highly sensitive to chamber wall loss and dilution, the modeled isotope ratios were more robust. Based on sensitivity tests, the combined model uncertainty is estimated to be approximately ±11 % for $\Delta^{17}O$, reflecting the maximum relative mean biases observed under extreme wall loss and dilution scenarios.~~

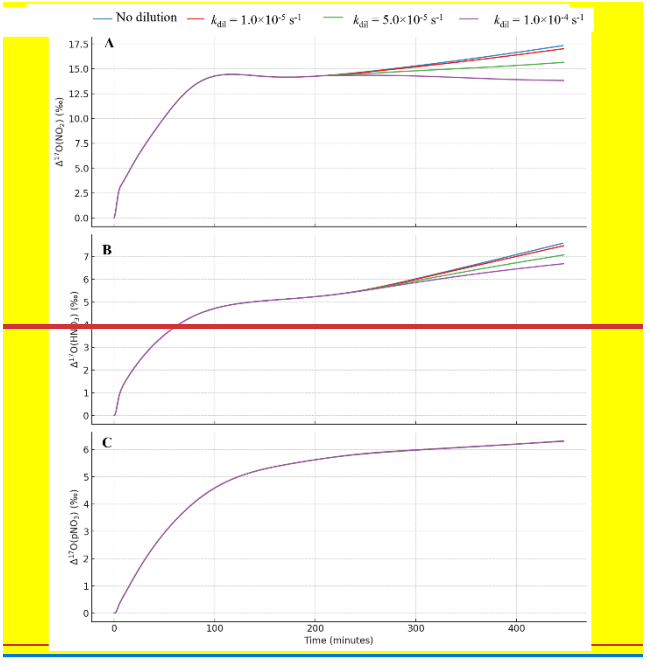

~~**Fig. 6. Dilution Rate Sensitivity= D17O?**~~

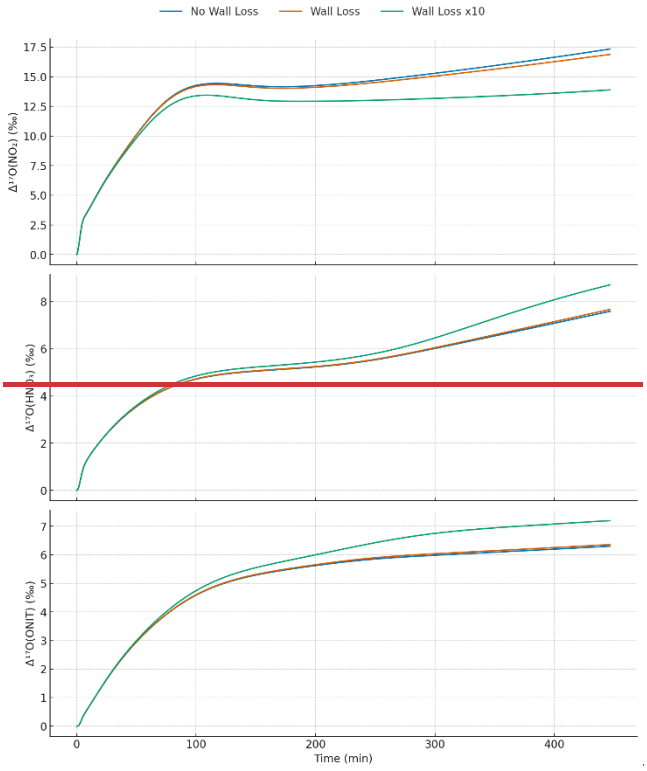

~~Fig. 7: Wall Loss~~

1050

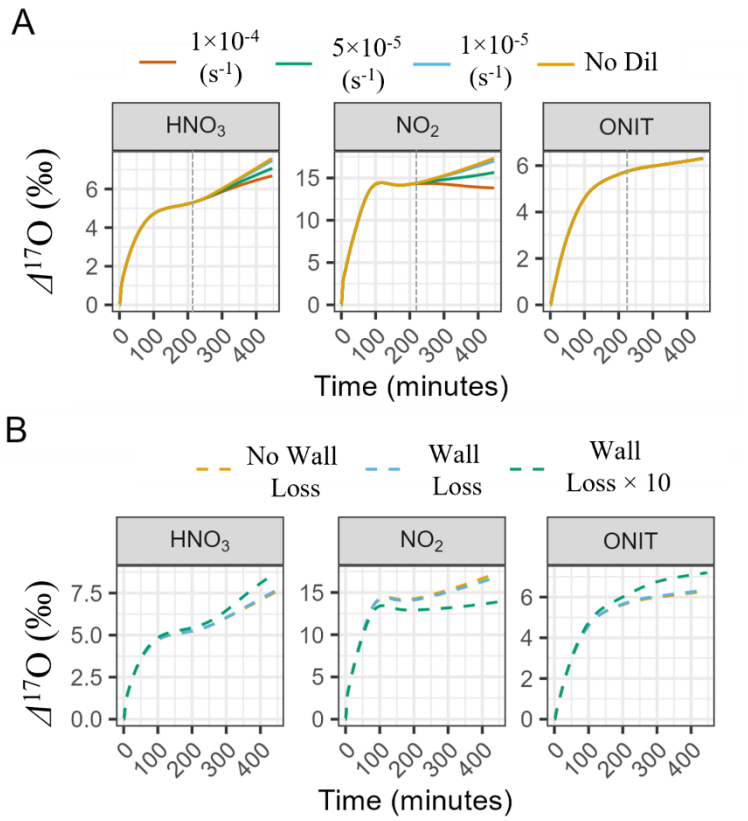

Fig. 6. Modeled $\Delta^{17}O$ sensitivity to physical chamber parameters. (A) Model simulations testing the sensitivity of $\Delta^{17}O$ in NO_2, HNO_3, and ONIT to chamber dilution rates, including scenarios with no dilution and with first-order dilution constants of 1×10^{-5}, 5×10^{-5}, and 1×10^{-4} s^{-1}. (B) Model simulations testing the impact of wall loss, comparing a no-wall-loss case, a wall loss scenario using reaction rates from (Wang et al., 2014) and (Morales et al., 2021), and a high-loss case in which wall loss rates were increased by a factor of 10. All simulations were performed under the conditions of Experiment 1. The gray dashed line in A corresponds to the start of chamber dilution.

3.3.~~2~~ 3 $\Delta^{17}O$ Base Model Simulations

B~~(Better Intro)~~uilding on the results of the sensitivity analyses, we next evaluate the performance of the base box model in simulating the $\Delta^{17}O$ values of key NO_y species, including NO_2, HNO_3, and ONIT under the various experimental conditions. These simulations incorporate the best-estimate physical parameters (e.g., dilution rate) and chemical mechanism inputs, including a representative $\Delta^{17}O(O_3^{term})$ value of 39 ± 2 ‰ (Fig. 7). Overall, t~~T~~he model simulations for the photochemical experiments indicate a substantial temporal change in $\Delta^{17}O$ for all considered NO_y compounds~~(NO_2) (Fig. 6~~8). The $\Delta^{17}O(NO_2)$ initially starts at 0 ‰ and begins to increase due to the production of O_3 that elevate $\Delta^{17}O(NO_2)$ as NO is oxidized by O_3. For the nighttime experiment, the box model predicts $\Delta^{17}O(NO_2)$ to remain steady with a value near 7.6 ‰, due to N_2O_5 thermal equilibrium with NO_2 and NO_3 resulting in the $\Delta^{17}O(NO_2)$ ~~≈~~= $\Delta^{17}O(N_2O_5)$. Generally, the $\Delta^{17}O$ simulation of NO_2 were in excellent agreement with the observations, as indicated by an ~~RMSE~~ average model bias of ~~1.7~~0.9 ± 2.4 ‰ (n = 8; ~~)~~Table 5) and a strong correlation indicated by a regression R^2 value of 0.98 ~~(Table 3)~~. ~~Considering the range of observed $\Delta^{17}O(NO_2)$ values that spanned 34.2‰, the model RMSE value is quite exceptional.~~ This strong agreement indicates that the box model and employed chemical mechanism ~~well represented~~accurately simulated ~~the~~ NO_x photochemical cycling and $NO_2/NO_3/N_2O_5$ thermal equilibrium. The simulation of $\Delta^{17}O(NO_2)$ is inherently sensitive to the assumed value of $\Delta^{17}O(O_3^{term})$, which represents the isotopic signature transferred from the terminal O atom of O_3 to NO_2 during oxidation. The relationship between measured $\Delta^{17}O(NO_2)$ and the mode~~l~~led fraction of O atoms in NO_2 deriving from O_3 (denoted as f(Q)) indicates that $\Delta^{17}O(O_3^{term})$ is 39.4 ± 0.6 ‰ (Fig. S~~X~~6), which is in excellent agreement with recent independent measurements of tropospheric O_3 reporting values of 39 ± 2 ‰ (Ishino et al., 2017; Vicars and Savarino, 2014). ~~Further, our model analysis would indicate that an assumed $\Delta^{17}O(O_3^{term})$ value of 39‰, well simulated the $\Delta^{17}O(NO_2)$ values across a range of experimental conditions. The strong agreement between the model and observations supports the robustness of our chemical mechanism in representing the critical oxidation processes and isotope transfer within the NO_x system. Additionally, the model's capability to simulate $\Delta^{17}O(NO_2)$ under both photochemical and nighttime conditions highlights its effectiveness in capturing the transition between photochemical and thermal equilibrium pathways in NO_x chemistry. For the nighttime experiment, the steady $\Delta^{17}O(NO_2)$ further confirms the model's accurate depiction of the equilibrium between NO_2, NO_3, and N_2O_5, an essential aspect of nighttime NO_x processing. This result indicates that the model is well suited to describe isotope dynamics in environments with varying NO_x levels and oxidant influences.~~

The measured $\Delta^{17}O(pNO_3)$ was compared with the simulated $\Delta^{17}O$ of ~~organic nitrate~~ (ONIT), based on our understanding that pNO_3 was apparently dominated by $RONO_2$ contributions~~(ONIT = ONITa + ONITb + ONITc +ONITOOHa + ONITOOHb + DIMER + PDN).~~

The temporal evolution of the simulated $\Delta^{17}O$(ONIT) closely followed that of $\Delta^{17}O(NO_2)$ but remained lower due to dilution effects associated with the dominant formation pathway of organic nitrates via NO + RO_2 reactions during the photochemical experiments, resulting in ONIT dominated by ONITa, ONITb, and ONITc compounds (Fig. S~~X~~3). During nighttime oxidation experiments, ONIT formation primarily proceeded via ~~R~~α-pinene + NO_3 reactions, leading to ONIT with higher contribution of ~~dominated by~~ DDIMER and PDN compounds ~~(Fig. SX)~~. Due to $NO_2/NO_3/N_2O_5$ thermal equilibrium that resulted in

$\Delta^{17}O(NO_2) \approx \Delta^{17}O(NO_3) \approx \Delta^{17}O(N_2O_5)$, the simulated nighttime $\Delta^{17}O$(ONIT) values were approximately equal to the simulated $\Delta^{17}O(NO_2)$. ~~T~~The simulated $\Delta^{17}O$(~~pNO3~~ONIT) ~~using the base mechanism~~ closely matched the $\Delta^{17}O(pNO_3)$ observations with an average ~~RMSE~~ bias of -1.~~2~~4 ± 2.4 ‰ (n =7), indicating that the relative production routes of organic nitrate (RO_2 + ~~+OH/O2~~NO vs ~~R~~RBVOC + NO_3; Table 1) were correctly simulated for the various experimental conditions~~-~~. The overall correlation was moderate, with R^2 = 0.55.~~(Fig. 7).~~ ~~Oxygen isotope mass balance indicates that the α pinene derived peroxy radical + NO pathway is expected to produce low $\Delta^{17}O$(ONIT) values, since only one oxygen atom in the nitro group of the resulting $RONO_2$ can originate from O_3.~~ ~~Oxygen isotope mass balance indicates that the α pinene derived peroxy radicals + NO pathway would be the expected pathway leaded to a low $\Delta^{17}O(pNO_3)$ value as only one oxygen atom in the nitro group of the generated $RONO_2$ could derive from O_3. In contrast, the α pinene oxidation involving NO_3 leading to organic nitrate would be the pathway leading to a high $\Delta^{17}O$(pNO3ONIT) value as all of the oxygen atoms in the NO_3 group could derive from O_3 (Walters et al., 2024a).~~

The bias for simulated $\Delta^{17}O$(ONIT) compared to the $\Delta^{17}O(pNO_3)$ observations was within 1.4 ‰ for all experiments except Exp. 5, where a substantially higher bias of -7.0 ‰ was observed. Excluding this outlier increased the correlation to R^2 = 0.97. Based on Cook's Distance and the Studentized Residual, Experiment 5 was identified as an outlier in the linear regression analysis. The larger model-data difference for Exp. 5 may reflect different oxidation dynamics or, more likely, uncertainty in the extraction of pNO_3. ~~Specifically, Exp. 5 resulted in the lowest Filter/AMS ratio for the photochemical experiments, suggesting potential under-recovery or sampling issues, such that the measured $\Delta^{17}O(pNO_3)$ from this experiment may not be representative of the pNO_3 formed during the chamber experiment (Table X).~~ Specifically, Experiment 5 yielded the lowest Filter/AMS ratio among the photochemical experiments, with the ratio falling below the quantitative range when accounting for propagated uncertainty. This suggests potential under-recovery or sampling artifacts, indicating that the measured $\Delta^{17}O(pNO_3)$ in this experiment may not accurately represent the pNO_3 formed during the chamber experiment (Table 3). Thus, the larger model-measurement $\Delta^{17}O$(ONIT) disagreement for Exp. 5 likely reflects uncertainty in the extracted NO_3^- rather than model misrepresentation of ONIT formation pathways. The measured $\Delta^{17}O(pNO_3)$ was also evaluated relative to the modeled f(Q) for ONIT formation. A linear regression constrained through the origin, excluding Exp. 5, yielded a slope of 41.7 ± 1.2 ‰ (R^2 = 0.996; Fig. S7~~X~~). This derived $\Delta^{17}O$(Q) value is in close agreement with the assumed $\Delta^{17}O(O_3^{term})$ value of 39 ± 2-‰, and is consistent with the value determined from the measured $\Delta^{17}O(NO_2)$ comparison with the modeled f(Q) of NO_2. ~~The excellent agreement between model and observation indicates that the developed chemical mechanism generally well reproduced organic nitrate formation pathways involving α pinene for the conducted photochemical experiments. Overall, the excellent agreement between model and observation for $\Delta^{17}O(pNO_3)$ provides confidence in the model's representation of organic nitrate formation involving α pinene across diverse photochemical conditions. It suggests that the model's parameterization of α pinene oxidation pathways and the resulting isotope fractionation effects on pNO_3 is well-calibrated, supporting its utility for simulating organic nitrate formation and its impact on aerosol chemistry.~~

The simulated dynamics of $\Delta^{17}O(HNO_3)$ closely follow the temporal evolution of $\Delta^{17}O(NO_2)$, initially starting at 0 ‰ and increasing as O_3 production occurs in the chamber during the photochemical experiments (i.e., Exp 1-5) (Fig. ~~6~~7). The simulated $\Delta^{17}O(HNO_3)$ for the photochemical experiments was always lower than $\Delta^{17}O(NO_2)$ for the photochemical experiments, as the model simulation predicts HNO_3 is predominantly produced through the NO_2 + OH pathway (Fig. S8~~X~~). Based on the conventional oxygen isotope mass-balance calculations, this pathway results in a dilution factor of 2/3 relative to $\Delta^{17}O(NO_2)$ (Table 1). ~~For the nighttime experiment, $\Delta^{17}O(HNO_3)$ is also predicted to be lower than $\Delta^{17}O(NO_2)$, driven by HNO_3 production from N_2O_5 + H_2O(g), with an expected dilution factor of 5/6 relative to $\Delta^{17}O(NO_2)$ (since $\Delta^{17}O(N_2O_5) \approx \Delta^{17}O(NO_2)$ due to thermal equilibrium).~~ For the nighttime experiment (Exp. 6), $\Delta^{17}O(HNO_3)$ is predicted to be slightly lower than $\Delta^{17}O(NO_2)$, primarily due to the contributions from two formation pathways: NO_3 + pinonaldehyde and N_2O_5 + H_2O(g), representing approximately 60 % and 40 % of nighttime HNO_3 production, respectively. Since $\Delta^{17}O(NO_3) \approx \Delta^{17}O(NO_2)$ under nighttime conditions due to rapid thermal equilibrium, the NO_3 + pinonaldehyde should result in $\Delta^{17}O(HNO_3) \approx \Delta^{17}O(NO_2)$. However, the N_2O_5 hydrolysis pathway incorporates one oxygen atom from water, which has $\Delta^{17}O \approx 0$ ‰, resulting in an effective dilution of the product $\Delta^{17}O(HNO_3)$ relative to $\Delta^{17}O(NO_2)$. Overall, the model exhibits poor agreement with observed $\Delta^{17}O(HNO_3)$ values with a model bias that ranged from -11.5 to 7.9 ‰ (Table 4~~X~~) and a weak correlation (R^2 = 0.39).~~-~~ The model underpredicts $\Delta^{17}O(HNO_3)$ for the low-NO_x photochemical experiments (Exp. 1 and 2) and the nighttime oxidation experiment (Exp. 6), but overpredicts $\Delta^{17}O(HNO_3)$ for the high-NO_x photochemical experiments (Exp. 3, 4, and 5). If the isotope mass-balance assumptions are correct, this pattern suggests that a missing or underrepresented source of high-$\Delta^{17}O$ HNO_3 may exist under low-NO_x conditions, and a missing low-$\Delta^{17}O$ HNO_3 source may exist under high-NO_x conditions.

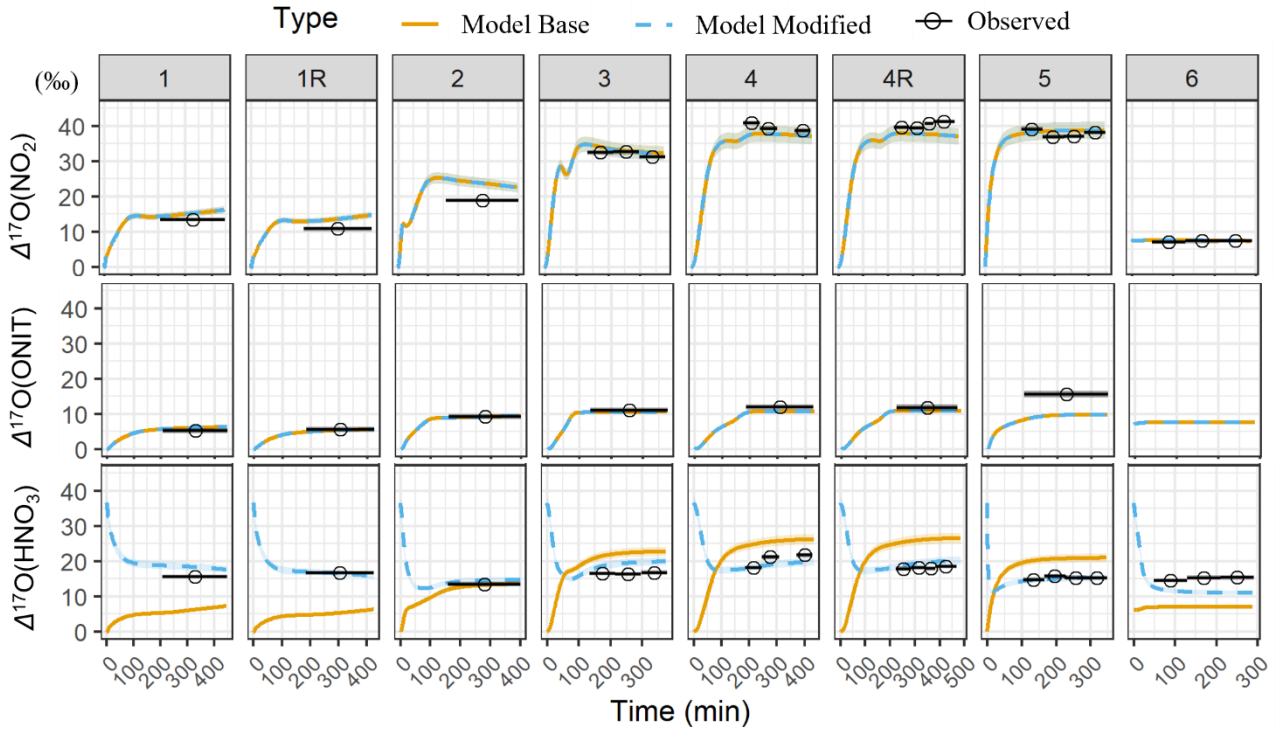

Fig. 7. Comparison between the modeled (base and modified) and observed $\Delta^{17}O(NO_2)$, $\Delta^{17}O(ONIT)$, and $\Delta^{17}O(HNO_3)$ values sorted by the various conducted experiments. The data points represent the average time of each sample collection, and the black line spans the duration of the collection period. The measurement uncertainty (±σ) is included as the shaded region. The modeled $\Delta^{17}O(ONIT)$ is compared to the observed $\Delta^{17}O(pNO_3)$.

Table 5. Summary of the calculated average bias ($\Delta^{17}O(Model) - \Delta^{17}O(Observed)$) for the $\Delta^{17}O$ model simulations using the NO_x–API base and modified (Mod) mechanisms. For experiments with multiple observations, the bias is reported as the mean ± standard deviation.

	NO_2			ONIT			HNO_3		
Exp	**Base**	**Mod**	***n***	**Base**	**Mod**	***n***	**Base**	**Mod**	***n***
1	1.7	1.7	1	0.8	0.8	1	-9.4	2.7	1
1R	2.6	2.6	1	-0.4	-0.4	1	-11.5	0.0	1
2	5.3	5.3	1	-0.1	-0.1	1	-0.7	0.8	1
3	1.2 ± 0.7	1.1 ± 0.8	3	-0.7	-0.7	1	5.5 ± 0.7	2.7 ± 0.7	3

4	-2.1 ± 0.9	-2.1 ± 0.9	3	-1.4	-1.4	1	5.2 ± 1.1	-1.4 ± 1.1	3
4R	-2.6 ± 0.7	-2.6 ± 0.9	4	-1.0	-1.0	1	7.9 ± 0.3	1.4 ± 0.3	4
5	0.7 ± 1.1	0.7 ± 1.3	4	-7.0	-7.0	1	5.3 ± 0.3	-0.3 ± 0.3	4
6	0.2 ± 0.2	0.2 ± 0.2	3	NA	NA	NA	-8.0 ± 0.4	-3.7 ± 0.7	3

3.3.4 $\Delta^{17}O(HNO_3)$ Model Sensitivity Tests

To investigate the causes of the observed discrepancies between modeled and measured $\Delta^{17}O(HNO_3)$ values, we conducted a series of model sensitivity tests focused on modifying HNO_3 formation pathways. These tests aimed to assess whether adjustments to reaction pathways or rate constants could reconcile the overprediction of $\Delta^{17}O(HNO_3)$ during the high-NO_x photochemical experiments (Exp. 3, 4, and 5) and the underprediction during low-NO_x and nighttime experiments. The following sections describe these targeted evaluations and their implications for understanding the $\Delta^{17}O(HNO_3)$ produced under different chemical regimes.

~~(intro statement here).~~ We first investigated the potential causes of the model overprediction in $\Delta^{17}O(HNO_3)$ during the high-NO_x photochemical experiments (Exp. 3, 4, and 5). Two alternative HNO_3 production pathways ~~that~~were identified that could ~~may~~ yield lower $\Delta^{17}O(HNO_3)$ values than the assumed predominant daytime ~~HNO_3~~ production pathway involving NO_2 + OH reactions ~~was evaluated~~ based on oxygen isotope mass-balance assumptions (Table 1). One such pathway is the reaction of NO with HO_2, which can form HNO_3 with a $\Delta^{17}O$ transfer factor of (1/3)$\Delta^{17}O(NO)$ (Alexander et al., 2020; Table 1). However, an underestimation of this pathway in the model is unlikely to account for the observed model–measurement discrepancy across all experiments. For instance, HO_2 concentrations in Exp. 5 are expected to be low due to the absence of significant amount of HO_2 precursors, unlike Exp. 3 ~~2~~ and ~~3~~4, which had elevated HO_2 precursors from the initial injected H_2O_2. Moreover, Exp. 1 and 2, which had the highest initial H_2O_2 concentrations and thus the greatest potential for HO_2 formation, exhibited model $\Delta^{17}O(HNO_3)$ values that were too low, further suggesting that this pathway cannot explain the observed discrepancies. Still, ~~A~~as a sensitivity test, we increased the rate constant for the NO + HO_2 → HNO_3 reaction (R027 in the NO_y-API mechanism; Table S3) by an order of magnitude (Fig. S~~X~~9). Despite this adjustment in the NO + HO_2 → HNO_3 reaction rate constant, the impact on modeled $\Delta^{17}O(HNO_3)$ remained small with a change in $\Delta^{17}O(HNO_3)$ of less than 1.6 ‰, and as little as 0.3 ‰ for Exp. 5. This change in model $\Delta^{17}O(HNO_3)$ is too small to account for the observed model bias of 5.2 to 7.9 ‰ across Exp. 3 to 5 (Table 4).

Next, the hydrolysis of organic nitrates to HNO_3 was evaluated as a potential low-$\Delta^{17}O(HNO_3)$ source, since hydrolysis of photochemically produced $RONO_2$ (R + OH/O_2/NO) could produce HNO_3 with a $\Delta^{17}O$ transfer factor of (1/3)($\Delta^{17}O(NO)$) (Table 1) considering that $\Delta^{17}O(RO_2)$ is presumably 0 ‰. ~~-~~Based on simulation results (Fig. S10~~X~~), 21.8 %, 14.8 %, and 13.4

% of the total NO_y was present as HNO_3 for Exp. 3, 4, and 5, respectively, compared to only 11.0 %, 6.8 %, and 4.0 % as ~~organic nitrates~~$RONO_2$ (defined as ONIT in our model simulations; ONIT = ONITa + ONITb + ONITc + ONITOOHa + ONITOOHb + PDN + DIMER). ~~Thus, it is unlikely that organic nitrate hydrolysis could account for the observed lower $\Delta^{17}O(HNO_3)$ compared to model predictions, unless a large proportion of organic nitrate hydrolyzed to HNO_3 and if the model had a substantial underestimate of organic nitrate production.~~ Nonetheless, as a sensitivity test, we added ~~organic nitrate~~ONIT hydrolysis with an assumed lifetime of 30 minutes (Table S~~7~~8), consistent with recent experimental determinations (Takeuchi and Ng, 2019); however, this study showed that only 23–32 % of organic nitrates derived from α-pinene + OH and 9–17% from α-pinene + NO_3 are susceptible to hydrolysis (Takeuchi and Ng, 2019), suggesting that this sensitivity test should overestimate the impact of ONIT hydrolysis as a production route for HNO_3. The inclusion of ~~organic nitrate~~ONIT hydrolysis in the model reduced $\Delta^{17}O(HNO_3)$ by 1.4–3.4 ‰ relative to the base model, partially improving agreement with observations (Fig. S11~~X~~). However, even under the unrealistic assumption of complete organic nitrate hydrolysis, the bias between the model and observed $\Delta^{17}O(HNO_3)$ values remained between 1.7 ‰ and 4.6 ‰ across experiments, indicating that hydrolysis alone cannot fully explain the model–observation discrepancy. Furthermore, while organic nitrate hydrolysis modestly improved the $\Delta^{17}O(HNO_3)$ comparison, it worsened the agreement for $\Delta^{17}O(ONIT)$ (Fig. S~~X~~12). The bias for the simulated $\Delta^{17}O(ONIT)$ relative to the observed $\Delta^{17}O(pNO_3)$ increased substantially, ranging from 5.1 ‰ to 15.0 ‰. ~~Overall, t~~These results suggest that organic nitrate hydrolysis is unlikely to be the primary cause of the observed lower $\Delta^{17}O(HNO_3)$ values relative to model simulations.

Overall, we were unable to identify a missing or underrepresented HNO_3 production pathway that could reconcile the observed $\Delta^{17}O(HNO_3)$ values within the bounds of ~~our~~the ~~conventional~~assumed $\Delta^{17}O$ mass-balance framework (Table 1). This suggests that current assumptions regarding oxygen atom ~~sources and~~ transfer during HNO_3~~s~~ formation may need to be revisited. For the high-NO_x photochemical experiments (Exp. 3–5), plotting measured $\Delta^{17}O(HNO_3)$ against the modeled fraction of O_3-derived oxygen atoms ($f(O)(HNO_3)$) gave a slope of 28.9 ± 0.5 ‰, representing the $\Delta^{17}O$ of the O_3^{term} (Fig. S13).~~When plotting the fraction of HNO_3 derived from the NO_2 + OH pathway, $f(O)$, against the measured $\Delta^{17}O(HNO_3)$, we observed a slope corresponding to a $\Delta^{17}O(O_3$-term) of 28.9 ± 0.5 ‰ (Fig. SX).~~ This slope is ~~notably~~ lower than the ~39-~~40~~1 ‰ slope obtained from similar analyses of $\Delta^{17}O(NO_2)$ and $\Delta^{17}O(pNO_3)$ (Fig. S6-S7~~X~~), which are more consistent with recent near-surface observations of $\Delta^{17}O(O_3^{term})$ (Ishino et al., 2017; Vicars and Savarino, 2014). The lower slope in the $f(O)$ versus $\Delta^{17}O(HNO_3)$ relationship potentially implies that not all oxygen atoms from NO_2 are retained during HNO_3 formation in the dominant NO_2 + OH reaction under high-NO_x photochemical conditions. Traditionally, it is assumed that two-thirds of the oxygen atoms in HNO_3 are inherited from NO_2 and one-third from OH (with $\Delta^{17}O \sim 0$ ‰) (Table 1), but this oxygen

mass-balance may need adjustment.~~.~~ Adjusting the slope for $\Delta^{17}O(HNO_3)$ versus $f(O)$ to match that for NO_2, would require to adjustment of the oxygen mass-balance in the NO_2 + OH reaction. Specifically, scaling the NO_2 contribution by ~0.74 lowers its O atom fractional contribution in HNO_3 from 66.7 % to ~49 %, resulting in an effective relationship of $\Delta^{17}O(HNO_3) \approx ½\Delta^{17}O(NO_2)$. ~~However, the comparison between slopes for HNO_3 (~28.9 ‰) and NO_2 (~39‰) suggests that this assumption may require scaling. Specifically, a factor of ~0.74 would adjust the NO_2 contribution from 66.7 % to approximately 49 %, yielding an empirical mass-balance relationship of $\Delta^{17}O(HNO_3) \approx (1/2)\Delta^{17}O(NO_2)$.~~ This deviation from the expected 2/3 to an effective 1/2 contribution of $\Delta^{17}O(NO_2)$ may reflect partial oxygen atom exchange or isotopic scrambling during the formation of an excited HNO_3 intermediate, prior to collisional stabilization. Such processes could result in the effective loss or redistribution of the oxygen atoms originally inherited from NO_2 in the HNO_3 product. Indeed, ~~This deviation could reflect partial oxygen atom exchange or isotopic scrambling during the formation of an excited HNO_3 intermediate prior to collisional stabilization, leading to the effective loss or redistribution of approximately one-sixth (~0.167) of the oxygen atoms originally associated with NO_2.~~ previous experimental studies using isotopically labeled ^{18}OH in reactions with NO_2 have demonstrated that the O atoms in the HNO_3 reactive intermediate product can undergo rapid intramolecular scrambling (Donahue et al., 2001). While this specific mechanism alone cannot easily explain the observed loss of approximately one-sixth of the original NO_2-derived oxygen atoms in the final HNO_3 product, it does suggest that interesting O isotope dynamics occur during the NO_2 + OH reaction. ~~Previous experimental work has suggested XXX~~While the exact mechanism that could explain the redistribution of ~1/6 of O atoms derived from NO_2 in the HNO_3 product remains uncertain and warrants further investigation, we conducted a sensitivity test by ~~, Still, as a sensitivity test, we updated~~updating the NO_x-API mechanism to reflect the potential modified mass balance for the NO_2 + OH reaction, assuming $\Delta^{17}O(HNO_3) = ½\Delta^{17}O(NO_2)$ (Fig. S14~~X~~). This adjustment substantially improved the model performance for Exp. 3-5, yielding biases that ranged from –2.6 ‰ to +1.0 ‰ relative to the observations.

Next, we examine the cause of the low model bias in $\Delta^{17}O(HNO_3)$ relative to observations during the nighttime oxidation experiment. In this experiment, the measured $\Delta^{17}O(HNO_3)$ exceeded that of $\Delta^{17}O(NO_2)$, implying greater O_3 incorporation into HNO_3 than is represented in the model. The dominant modeled pathway for HNO_3 formation at night was the reaction of NO_3 with pinaldehyde (Fig. S8~~X~~). However, this route yields $\Delta^{17}O(HNO_3) \approx \Delta^{17}O(NO_3)$, because NO_2, NO_3, and N_2O_5 rapidly equilibrate thermally overnight leading to $\Delta^{17}O(NO_2) \approx \Delta^{17}O(NO_3) \approx \Delta^{17}O(N_2O_5)$. Therefore, this pathway alone cannot account for the elevated observed $\Delta^{17}O(HNO_3)$ relative to the model simulation. To explain this discrepancy, an additional source of high-$\Delta^{17}O$ external to the NO_{xy} reservoir must be involved. One possibility is that the heterogeneous uptake of N_2O_5 on aerosol surfaces could involve incorporation of an oxygen atom from O_3 rather than liquid water. In this case, based on our mass-balance framework (Table 1), the $\Delta^{17}O$ of HNO_3 formed via this pathway can be represented as:

$$\Delta^{17}O(HNO_3) = (5/6) * \Delta^{17}O(N_2O_5) + (1/6) * \Delta^{17}O(O_3^{term}) \quad \text{(Eq. 8~~X~~)}$$

Since $\Delta^{17}O(NO_2) \approx \Delta^{17}O(N_2O_5)$ for our nighttime oxidation experiment conditions, this expression simplifies to:

$$\Delta^{17}O(HNO_3) = (5/6) * \Delta^{17}O(NO_2) + (1/6) * \Delta^{17}O(O_3^{term}) \quad \text{(Eq. 9X)}$$

This mass-balance equation is similar to that assumed for N_2O_5 heterogenous reaction involving particulate Cl^- (Table 1). While, we did not initiate our experiment with a Cl^- source, we must have a source of $\Delta^{17}O(O_3^{term})$ external to NO_x to explain the underestimate of simulated $\Delta^{17}O(HNO_3)$ relative to observations.

To test the potential impact of this mechanism, we incorporated N_2O_5 heterogeneous uptake into the model (Table S9X). The uptake rate coefficient (k_{het}) was estimated assuming an aerosol seed number and volume concentration upon atomization of 2×10^4 cm^{-3} and 2×10^{10} nm^3 cm^{-3}, respectively, which was taken from previously reported values from similarly conducted α-pinene + NO_3 nighttime experiments (Takeuchi and Ng, 2019), and an N_2O_5 uptake coefficient (γ) of 1.5×10^{-4} for organic carbon with RH ≥ 30 % (Escorcia et al., 2010)~~(Holmes et al., 2019)~~. Due to uncertainty in these parameters, we performed a sensitivity analysis across a range of k_{het} values from 0.6×10^{-4} to 6×10^{-4} s^{-1}, corresponding to N_2O_5 lifetimes between approximately 0.46 and 4.6 hours. Model results show that increasing the N_2O_5 heterogeneous reaction rate systematically reduces the $\Delta^{17}O(HNO_3)$ model bias. Specifically, the bias decreased from 8.1 ‰ in the base case (no heterogeneous uptake) to 3.5 ‰ for the highest assumed k_{het} (Fig. S15X). This supports the hypothesis that N_2O_5 heterogeneous reactions incorporating O_3-derived oxygen significantly influence the isotopic composition of HNO_3 produced under nighttime conditions. However, the highest assumed k_{het} rate led to an increase in the overall model bias for $\Delta^{17}O(HNO_3)$ simulations the high-NO_x photochemical experiments (Exp 3-5), shifting from −0.8 ± 1.5 ‰ in the modified mass-balance simulation to +1.8 ± 2.5 ‰ (Fig. S16X). To avoid overcorrection, we selected a k_{het} rate of 9.11×10^{-5} s^{-1}, which improved agreement in the nighttime oxidation experiments without negatively impacting the $\Delta^{17}O(HNO_3)$ predictions under high-NO_x photochemical conditions.

Lastly, we sought to diagnose the potential underprediction of $\Delta^{17}O(HNO_3)$ in the model relative to observations from the low-NO_x photochemical experiments (Exp. 1–2). We observed a relatively large amount of HNO_3 present before the experiments began, ranging from 3.2 to 5.1 ppb, which represented 20.1 %, 18.0 %, and 7.9 % of the maximum HNO_3 concentrations measured during Exp. 1, 1R, and 2, respectively (Table S10; ~~X;~~ Fig. S1X). This suggested the possibility of a substantial chamber blank influencing the $\Delta^{17}O(HNO_3)$ measurements. Unfortunately, we did not directly quantify chamber blanks during these experiments. Thus, to evaluate the potential impact, we conducted a sensitivity analysis by introducing a new model tracer, HNO_3^{blank}, which was initialized using pre-experiment CIMS measurements. This tracer was treated identically to HNO_3 in the model, undergoing the same reactions and loss processes as HNO_3 (Table S11X). We then used an

isotope mass-balance framework to infer the $\Delta^{17}O$ of the blank component required to reproduce the observed $\Delta^{17}O(HNO_3)$ (Eq. 10):

$$\Delta^{17}O(HNO_3^{blank}) = \frac{\Delta^{17}O(HNO_3^{obs}) - (1 - f_{blank})\Delta^{17}O(HNO_3^{prod})}{f_{blank}} \quad \text{(Eq. 10)}$$

where $\Delta^{17}O(HNO_3^{obs})$ is the observed value, $\Delta^{17}O(HNO_3^{prod})$ is the value for photochemically produced HNO_3 in the model, and f_{blank} is the fractional contribution of the chamber blank from the model simulation:

$$f_{blank} = \frac{[HNO_3^{blank}]}{[HNO_3^{blank}] + [HNO_3^{prod}]} \quad \text{(Eq. 11)}$$

Using this approach, we calculated an average $\Delta^{17}O(HNO_3^{blank})$ of 36.1 ± 4.0 ‰ (n = 3). While elevated, this value is plausible if HNO_3 formation occurred predominantly through nighttime N_2O_5 heterogeneous uptake under dark chamber conditions prior to the start of the experiment, and if the precursor NO_2 had a high $\Delta^{17}O$ value. Such conditions could arise from residual NO_2 in the chamber either from previous experiments or background air that underwent oxidation while the chamber remained dark and inactive before the conducted experiments were initiated. ~~While elevated, this value is plausible if HNO_3 formation occurred predominantly through nighttime N_2O_5 heterogeneous uptake under dark chamber conditions before lights were turned on.~~ It is also important to note that the CIMS HNO_3 measurements are subject to a relatively large uncertainty of approximatcely ±20 ‰, which may further influence the inferred blank correction.

Overall, to improve the accuracy of simulated $\Delta^{17}O(HNO_3)$, we implemented a series of modifications to the NO_x-API mechanism based on the conducted sensitivity tests, term NO_x-API (Modified). First, we revised the oxygen mass balance for $\Delta^{17}O(HNO_3)$ formation via the NO_2 + OH reaction, to (1/2)$\Delta^{17}O(NO_2)$. Second, we included a chamber-derived HNO_3 background using a fixed $\Delta^{17}O$ value of 36.1 ‰. This background was initialized in all simulations based on CIMS-derived HNO_3 concentrations prior to photolysis onset (Table S10~~X~~). Finally, we added a heterogeneous N_2O_5 hydrolysis pathway with a first-order loss rate of 9.11 × 10^{-5} s^{-1}, using a $\Delta^{17}O(HNO_3)$ formation mass balance of (5/6) × $\Delta^{17}O(N_2O_5)$ + (1/6) × $\Delta^{17}O(O_3^{term})$. As shown in Fig. 7~~6~~, while these modifications had a minor effect on $\Delta^{17}O(NO_2)$ and $\Delta^{17}O(ONIT)$, in which the base NO_x-API mechanism were already in strong agreement with the observations, they substantially improved the model's performance for $\Delta^{17}O(HNO_3)$. The average absolute bias across all experiments decreased from 6.7 ± 3.3 ‰ in the base mechanism to 1.6 ± 1.3 ‰ in the modified mechanism (Table 5~~X~~) and with an improved correlation (R^2 = 0.48). These results demonstrate the difficulty of accurately simulating $\Delta^{17}O(HNO_3)$ across diverse experimental conditions, highlighting the need for future experiments that more directly constrain oxygen isotope mass-balance assumptions in HNO_3 formation pathways.

At the same time, careful attention to HNO_3 collection methods and blank corrections is essential to ensure meaningful comparisons between models and observations.

~~The simulated $\Delta^{17}O$ of HNO_3 (Fig. 8) begins at 26‰, reflecting the assumed $\Delta^{17}O$ value of an HNO_3 chamber blank. This initial value was not directly measured but was estimated to achieve agreement with the measured $\Delta^{17}O$ of HNO_3 in Exp. 1 and Exp. 2, where HNO_3 production was relatively low (Fig. S1). At the onset of the experiment, $\Delta^{17}O(HNO_3)$ decreases as newly formed HNO_3, which has a $\Delta^{17}O$ lower than the chamber blank value, begins to dominate. For Exp. 1, 2, and 6, $\Delta^{17}O(HNO_3)$ continues to decrease over time, eventually reaching a plateau as HNO_3 production ceases. In contrast, for Exp. 3, 4, and 5, after an initial decline in $\Delta^{17}O(HNO_3)$, the values begin to rise. This increase is driven by the production of HNO_3 with higher $\Delta^{17}O$ values, resulting from elevated $\Delta^{17}O(NO_2)$ associated with the buildup of O_3. Overall, the simulated $\Delta^{17}O(HNO_3)$ is proportional to the maximum $\Delta^{17}O(NO_2)$, reflecting the dilution of $\Delta^{17}O(NO_2)$ in additional NO_y products due to the incorporation of O atoms from oxidants other than O_3. Overall, the model does a poor job of capturing $\Delta^{17}O(HNO_3)$ relative to observations, with an average RMSE of 4.6‰ compared to an observed range of 8.2‰. The model reasonably aligns with observations for the Exp. 1 and 2, where measurements were influenced by a chamber blank or HNO_3 carry-over effect, assumed to have a $\Delta^{17}O(HNO_3)$ value of 26‰. However, for the high initial NO_x concentration experiments (Exp. 3, 4, and 5), the simulated $\Delta^{17}O(HNO_3)$ was consistently too high. In the high HNO_3 production experiments (Exp. 4 and 5), the influence of a potential chamber HNO_3 blank was negligible due to the large amount of HNO_3 produced (Fig. S1). Here, the discrepancies between measured and modeled $\Delta^{17}O(HNO_3)$ suggest a missing or under-accounted HNO_3 production pathway. Based on oxygen isotope mass balance expectations, we identified two potential pathways that could yield a lower $\Delta^{17}O(HNO_3)$ than the dominant NO_2+OH channel, which has a $\Delta^{17}O$ transfer factor of (2/3)($\Delta^{17}O(NO_2)$) (Alexander et al., 2020). First, the NO + HO_2 reaction was considered as a possible source of low $\Delta^{17}O(HNO_3)$, with a $\Delta^{17}O$ transfer factor of (1/3)($\Delta^{17}O(NO)$) (Alexander et al., 2020). However, this reaction is unlikely to explain the model mismatch since HO_2 levels were low in Exp 5. Second, organic nitrate hydrolysis could be a possible source of low $\Delta^{17}O$ HNO_3, especially if derived from +OH/NO reactions with a $\Delta^{17}O$ transfer factor of (1/3)($\Delta^{17}O(NO)$) (Walters et al., 2024a). This source of HNO_3 would not be consistent with the $\delta^{15}N$ data of HNO_3 and pNO_3, which indicated large differences suggesting that these molecules were not related (Fig. 2). Still, to test this hypothesis, we conducted a sensitivity analysis allowing pinene hydroxyl nitrate, pinene carbonyl nitrate, and pinene nitrooxy hydroperoxide to hydrolyze with a lifetime of 2 hours (Table S3). We did not enable the dimer or pinene dinitrate to hydrolyze since these were dominant organic nitrate formed during nighttime oxidation, which we found minimal hydrolysis to occur from the filter extracts (Fig. 3). This modified simulation, "USC_API_Hydro," slightly improved the $\Delta^{17}O(HNO_3)$ agreement for Exp. 3, 4, and 5, reducing the average RMSE from 5.5‰ in the base model to 3.8‰ in the updated model (Table 3). However, for experiments with low-medium initial NO_x concentration (Exp. 1 and 2), organic nitrate hydrolysis resulted in a higher RMSE (6.3‰) compared to the base model (1.9‰). Organic nitrate hydrolysis had minimal impact on $\Delta^{17}O(NO_2)$ but did affect $\Delta^{17}O(pNO_3)$, particularly in high initial NO_x concentration experiments. Specifically, including this pathway decreased model performance for $\Delta^{17}O(pNO_3)$ in Exp. 3 and 4, though it improved the fit~~

for Exp. 5. Overall, despite considering hydrolysis of organic nitrate to HNO_3, the simulated $\Delta^{17}O(HNO_3)$ for Exp. 4 and 5 remained too high to match observations and was not improved by decreasing the hydrolysis lifetime.

Therefore, based on our oxygen isotope mass balance framework, we were unable to identify a suitable missing or under-constrained HNO_3 production source in the model to explain the relatively low observed $\Delta^{17}O(HNO_3)$ in high NO_x experiments. Thus, we speculate that the collected HNO_3 in high initial NO_x experiments (Exp. 4 and 5) may not fully represent HNO_3 produced under experimental conditions. While we would not expect $\Delta^{17}O$ fractionation if HNO_3 were incompletely collected by the denuder system, our results may be biased toward HNO_3 produced earlier in the experiments when $\Delta^{17}O(HNO_3)$ is expected to be lower (Fig. 8). Although our collection method yielded consistent and precise $\Delta^{17}O(HNO_3)$ values across repeat experiments (Blum et al., 2023), the accuracy of these values remains uncertain. These findings suggest that an alternative HNO_3 collection method may be necessary to more accurately characterize $\Delta^{17}O(HNO_3)$ in chamber experiments.

Overall, the results of the $\Delta^{17}O$ model simulations offer detailed insights into the oxidation chemistry dynamics associated with NO_x and α pinene under varied photochemical and nighttime conditions. The model effectively captured the oxidation dynamics associated with NO_2 photochemical cycling and nighttime equilibrium as well as captured the chemistry associated with organic nitrate formation. However, the model displayed limitations in simulating $\Delta^{17}O(HNO_3)$, particularly for experiments with high initial NO_x conditions where the observed values were lower than predicted. Sensitivity analyses suggested that inclusion of additional HNO_3 formation pathways such as organic nitrate hydrolysis could partially improve the model's accuracy though further refinement is necessary and suggesting a potential artifact associated with HNO_3 collection.

Table 3. Summary of the calculated average RMSEaverage bias ($\Delta^{17}O$(Model) – $\Delta^{17}O$(Observed) for the $\Delta^{17}O$ model simulations using the USC API chemistry and inclusion of organic nitrate hydrolysis (USC API Hydro) mechanism.NOx API base and modified mechanisms.

	$\Delta^{17}O(NO_2)$ (‰)			$\Delta^{17}O(pNO_3)$ (‰)			$\Delta^{17}O(HNO_3)$ (‰)		

Exp	USC-API	n	USC-API	n	USC-API	USC-API-Hydro	n
1	1.1	1	0.6	1	1.4	7.0	1
1R	2.0	1	0.8	1	3.7	9.3	1
2	3.9	1	0.4	1	0.5	2.7	1
3	0.6	3	0.6	1	5.5	3.0	3
4	2.5	3	1.2	1	5.0	2.2	3
4R	3.1	4	0.8	1	7.8	5.0	4
5	1.2	4	7.1	1	5.6	3.5	4
6	0.3	3	NA	1	3.1	3.7	3
AVG	**1.8**		**1.6**		**4.1**	**4.6**	

	NO_2			ONIT			HNO_3		
Exp	Base	Mod	n	Base	Mod	n	Base	Mod	n
1	1.7	1.7	1	0.8	0.8	1	-9.4	2.7	1
1R	2.6	2.6	1	-0.4	-0.4	1	-11.5	0.0	1
2	5.3	5.3	1	-0.1	-0.1	1	-0.7	0.8	1
3	1.2±0.7	1.1±0.8	3	-0.7	-0.7	1	5.5±0.7	2.7±0.7	3
4	-2.1±0.9	-2.1±0.9	3	-1.4	-1.4	1	5.2±1.1	-1.4±1.1	3
4R	-2.6±0.7	-2.6±0.9	4	-1.0	-1.0	1	7.9±0.3	1.4±0.3	4
5	0.7±1.1	0.7±1.3	4	-7.0	-7.0	1	5.3±0.3	-0.3±0.3	4
6	0.2±0.2	0.2±0.2	3	NA	NA	NA	-8.0±0.4	-3.7±0.7	3

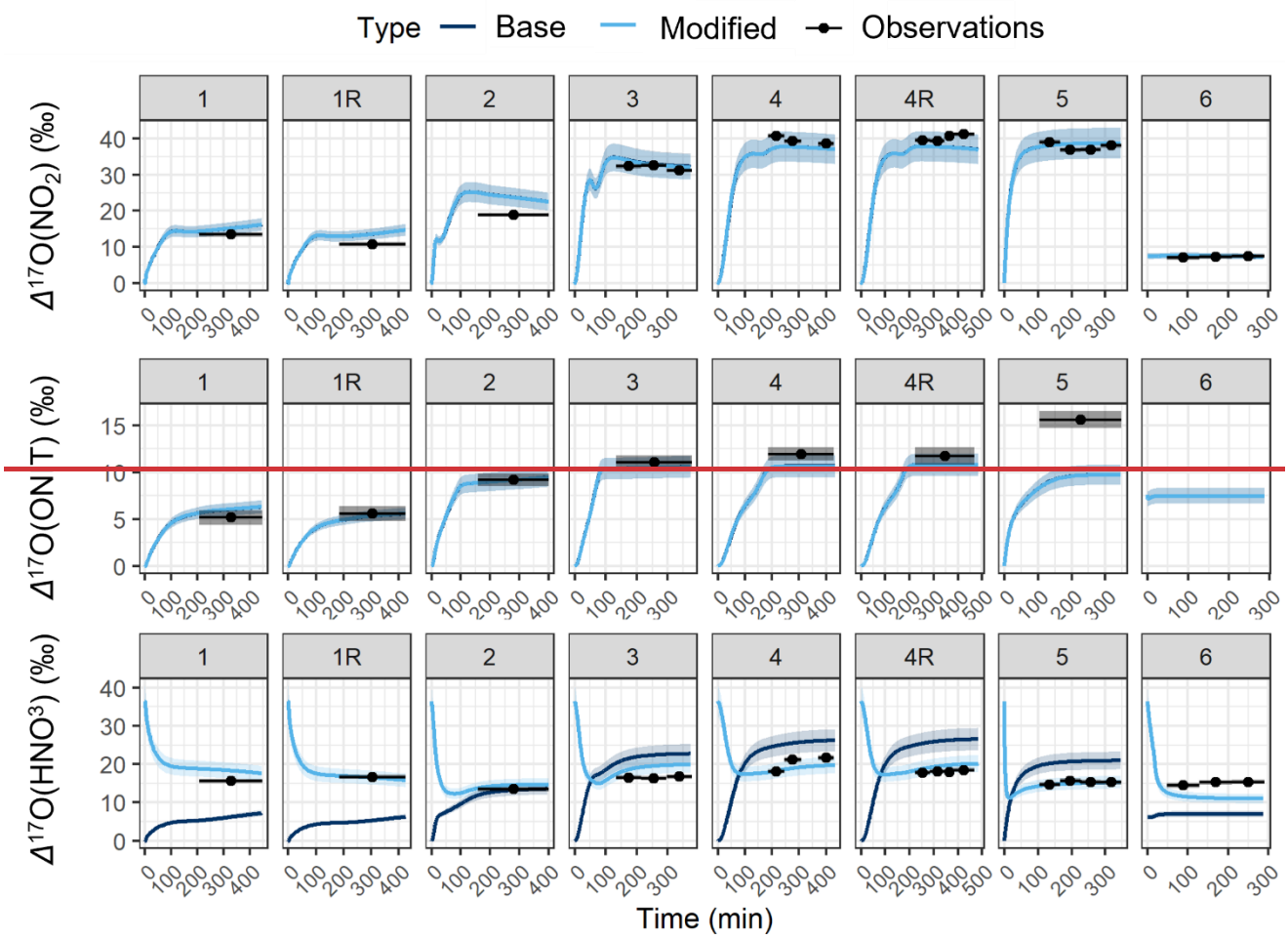
Type
Base
Modified
Observations
1
1R
2
3
4
4R
5
6
Δ17O(NO2) (‰)
Δ17O(ONIT) (‰)
Δ17O(HNO3) (‰)
Time (min)

1385

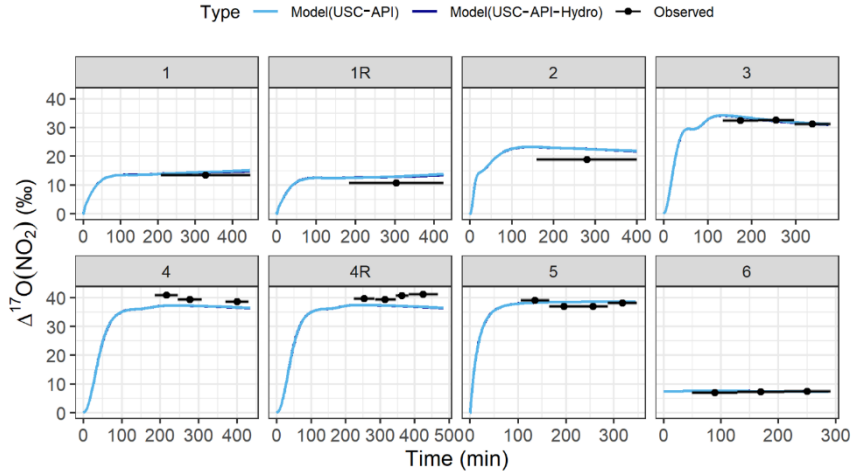

~~Fig. 6. Comparison between the modeled (base and modified) and observed $\Delta^{17}O(NO_2)$, $\Delta^{17}O(ONIT)$, and $\Delta^{17}O(HNO_3)$ values sorted by the various conducted experiments. The data points represent the average time of each sample collection, and the black line spas the duration of the collection period. The data points represent the average experiment time for each denuder collection, with the black line span the collection time range (from start to stop). The measurement uncertainty (±σ) is included as the lighter grey shaded region.shaded region. For the modeled $\Delta^{17}O(ONIT)$ is compared to the observed $\Delta^{17}O(pNO_3)$. The model simulations include both the base model (USC-API) and considering the potential role of organic nitrate hydrolysis (USC-API-Hydro). The inclusion of~~

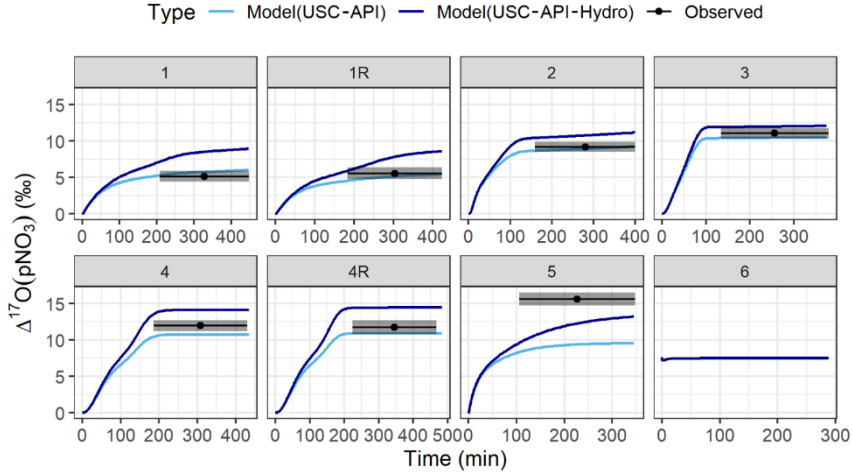

~~organic hydrolysis had a near-negligible impact on $\Delta^{17}O(NO_2)$.~~

~~Fig. 7. Comparison between the modeled and observed $\Delta^{17}O(pNO_3)$ values sorted by the various conducted experiments. The data points represent the average experiment time for each denuder collection, with the black line span the collection time range (from start to stop). The measurement uncertainty (±σ) is included as the lighter grey shaded region. The model simulations include both the base model (USC-API) and considering the potential role of organic nitrate hydrolysis (USC-API-Hydro).~~

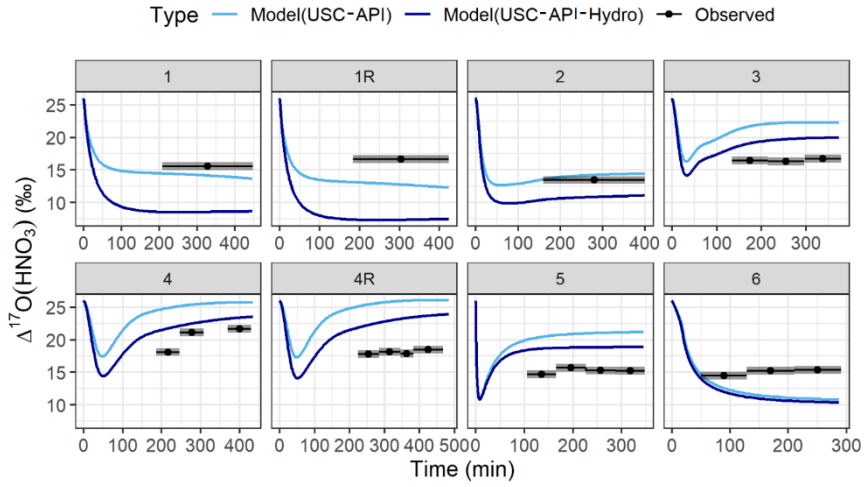

Fig. 8. Comparison between the modeled and observed $\Delta^{17}O(HNO_3)$ values sorted by the various conducted experiments. The data points represent the average experiment time for each denuder collection, with the black line span the collection time range (from start to stop). The measurement uncertainty (±σ) is included as the lighter grey shaded region. The model simulations include both the base model (USC-API) and considering the potential role of organic nitrate hydrolysis (USC-API-Hydro). The $\Delta^{17}O(HNO_3)$ is initially set at 26‰, based on the assumption that the HNO_3 "chamber blank" had this value.

3.3.3 $\delta^{15}N$ Simulation

Future studies should prioritize refining isotopic fractionation factors, especially for reactions involving reactive nitrogen oxides and hydroxyl radicals, to better capture nitrogen isotope variability in photochemical environments. Additionally, advancements in experimental setups to mitigate sampling artifacts could enhance the reliability of $\delta^{15}N$ measurements, thereby improving model accuracy for nitrogen isotopic compositions in complex photochemical systems.

The $\delta^{15}N$ simulations using the base chemistry mechanism indicate intriguing isotope dynamics (Fig. 9). Generally, the simulated $\delta^{15}N(NO_2)$ quickly increases at the start of the experiment due to the NO/NO_2 isotope exchange with a large isotope fractionation factor which preferentially favors the partitioning of ^{15}N into NO_2 relative to NO. For the photochemical experiments, as NO_2 is converted to HNO_3, the $\delta^{15}N(NO_2)$ decreases due to the assumed isotope fractionation associated with the NO_2 + OH reaction of 1.040 (Fang et al., 2021), favoring the preferential transfer of ^{15}N into the HNO_3 product. This also leads to the model predicting higher $\delta^{15}N(HNO_3)$ relative to NO_2, as the NO_2 + OH was the dominant reaction pathway for HNO_3 production in the photochemical experiments. The $\delta^{15}N(pNO_3)$ initially starts near the starting $\delta^{15}N(NO)$ value as α-pinene derived peroxy radicals + NO was the main simulated formation pathway for the photochemical experiments. Due to the NO/NO_2 isotope equilibrium reaction, the $\delta^{15}N(NO)$ decreases relative to $\delta^{15}N(NO_x)$ as ^{15}N preferentially partitions into NO_2. This causes the low $\delta^{15}N$ of the formed pNO_3, which was derived from organic nitrate, relative to the other measured NO_y components.

Overall, the $\delta^{15}N(NO_2)$ simulation using the base chemistry model had decent agreement with the observations with an RMSE of 8.9‰; however, large disagreements were observed for photochemical experiments with elevated initial NO_x (Fig. 9; Table 4). For these experiments (Exp. 3–5), the simulated $\delta^{15}N(NO_2)$ were much lower than observed and the model predicted a substantial decrease in $\delta^{15}N(NO_2)$ as the experiment progresses which was not observed. The photochemical cycling involving NO_x was well simulated using the model chemistry as evidenced by a strong concentration and $\Delta^{17}O$ agreement between observations and model. It is inherently more challenging to model $\delta^{15}N$ compared to $\Delta^{17}O$ of NO_y compounds. This is due to mass dependent fractionation that can have a significant impact on $\delta^{15}N$ values, which is largely assumed in the adapted i_NRACM mechanism (Fang et al., 2021). Therefore, we speculate that the $\delta^{15}N(NO_2)$ model disagreement could be due to inaccurate nitrogen fractionation utilized within i_NRACM. The model simulation predicted a substantial decrease in $\delta^{15}N(NO_2)$ as the experiments progressed due to the large nitrogen isotope fractionation factor or KIE associated with the NO_2 + OH reaction assumed in the i_NRACM mechanism to be 1.040 (Fang et al., 2021), defined as (Eq. 9):

$$KIE = {}^{15}\alpha = \frac{{}^{15}k_{NO_2+OH}}{{}^{14}k_{NO_2+OH}} \quad \text{(Eq. 9)}$$

Previously, the KIE associated with this reaction has been estimated to be 0.997 based on the reduced masses in the transition complex (Freyer, 1991). Therefore, we also conducted additional $\delta^{15}N$ simulations using a KIE (or ${}^{15}\alpha$) for the NO_2 + OH reaction of 0.997 (Fig. 6), noted as the USC_API KIE. The modified $\delta^{15}N(NO_2)$ simulations, using the adjusted NO_2 + OH KIE, resulted in a better agreement with the observations decreasing the RMSE from 8.9 to 2.6 ‰ (Table 4). Considering the large range of $\delta^{15}N(NO_2)$ observations that spanned 72.2‰, the modified $\delta^{15}N(NO_2)$ simulations are in close agreement (within 4%) of the observations. Further, the modified simulations indicated that $\delta^{15}N(NO_2)$ temporal simulation better matched the observations for the photochemical experiments with high initial NO concentrations (Exp 3–5) (Fig. 9). Overall, based on a comparison of measured to simulated $\delta^{15}N(NO_2)$, the NO_2 + OH KIE was best approximated using a value of 0.997, enabling the accurate simulation of $\delta^{15}N(NO_2)$.

Generally, the simulated $\delta^{15}N(pNO_3)$ values were in close agreement with the observations with an RMSE of 5.0‰ for the base simulations (Fig. 10; Table 4), especially considered the measurement uncertainty that was as high as 4.1‰ due to a significant filter NO_2^- blank. The modified $\delta^{15}N$ simulations using the adjusted NO_2 + OH ${}^{15}\alpha$ of 0.997 slightly decreased the RMSE of $\delta^{15}N(pNO_3)$ to 4.5%. The simulated $\delta^{15}N(pNO_3)$ were insensitive to the adjustments for NO_2 + OH KIE because the organic nitrate formed relatively quickly under the experimental conditions before significant influence of the NO_2 + OH isotope effect on the residual $\delta^{15}N(NO_x)$. Overall, this excellent $\delta^{15}N$ comparison indicates that the adapted i_NRACM mechanism well describes the fractionation associated with NO + α pinene derived peroxy radicals. This result validates the mechanism's utility for modeling $\delta^{15}N$ values in similar organic influenced photochemical environments.

In contrast to $\delta^{15}N(NO_2)$ and $\delta^{15}N(pNO_3)$, the model struggled to accurately simulate the $\delta^{15}N(HNO_3)$ observations with an RMSE of 12.5‰ for the base model simulation (Fig. 11; Table 4). The modified $\delta^{15}N$ simulations that included an update to $NO_2 + OH$ $^{15}\alpha$ to 0.997, led to worse agreement between the model and observed $\delta^{15}N(HNO_3)$ values with an RMSE of 24.1‰. Notably, the modified $\delta^{15}N$ model mechanism simulations significantly improved the model $\delta^{15}N(HNO_3)$ agreement with observations for the HONO experiments, which were too high in the base model simulations (Fig. 11). However, the modified mechanism led to a worse agreement between the simulated $\delta^{15}N(HNO_3)$ and observations for the photochemical experiments involving H_2O_2 and NO (Exp 1–4). We speculate that these differences could be due to sampling artifacts or HNO_3 loss on the chamber wall and/or sampling inlets, consistent with our findings for the $\Delta^{17}O(HNO_3)$ simulations. These artifacts highlight the challenges associated with accurately capturing $\delta^{15}N(HNO_3)$ in chamber studies, where wall effects and sampling techniques may interfere with precise isotopic measurements.

Our model comparison highlights the complexity of simulating nitrogen isotope dynamics in atmospheric chamber experiments. The improved $\delta^{15}N(NO_2)$ agreement with an adjusted KIE value for $NO_2 + OH$ highlights the sensitivity of nitrogen isotopes to specific fractionation processes. While $\delta^{15}N(pNO_3)$ simulations were robust to changes in KIE, indicating the stability of iNRACM's treatment of NO + organic peroxy radical interactions, the $\delta^{15}N(HNO_3)$ simulations revealed limitations in both base and modified models. The findings suggest that additional factors, such as chamber wall interactions, may need to be considered to improve $\delta^{15}N(HNO_3)$ model performance. Future studies should prioritize refining isotopic fractionation factors, especially for reactions involving reactive nitrogen oxides and hydroxyl radicals, to better capture nitrogen isotope variability in photochemical environments. Additionally, advancements in experimental setups to mitigate sampling artifacts could enhance the reliability of $\delta^{15}N$ measurements, thereby improving model accuracy for nitrogen isotopic compositions in complex photochemical systems.

Table 4. Summary of the calculated average RMSE for the $\delta^{15}N$ model simulations using the base chemistry (USC-API) and the KIE mechanism (USC-API-KIE), which includes an updated $^{15}\alpha$ for the NO_2+OH reaction of 0.997.

	$\delta^{15}N(NO_2)$ (‰)			$\delta^{15}N(pNO_3)$ (‰)			$\delta^{15}N(HNO_3)$ (‰)		
Exp	USC-API	USC-API-KIE	*n*	USC-API	USC-API-KIE	*n*	USC-API	USC-API-KIE	*n*
1	5.8	0.7	1	1.1	3.2	1	2.0	18.5	1
1R	9.4	3.7	1	2.0	0.1	1	1.1	18.9	1
2	6.1	1.9	1	3.7	0.9	1	5.2	29.5	1
3	15.0	1.6	3	14.9	12.7	1	19.1	44.2	3
4	11.3	1.8	3	4.1	5.9	1	7.8	23.6	3

4R	15.7	2.5	4	0.0	1.7	1	8.1	37.9	4
5	3.0	4.0	4	9.2	6.8	1	38.8	2.2	4
6	4.8	4.8	3	N/A	N/A	1	18.0	18.1	3
AVG	**8.9**	**2.6**		**5.0**	**4.5**		**12.5**	**24.1**	

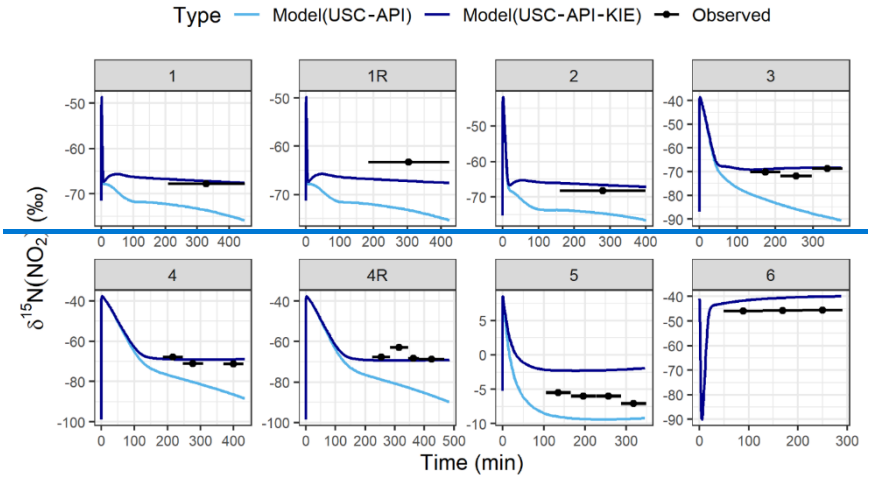

Fig. 9. Comparison between the modeled and observed $\delta^{15}N(NO_2)$ values sorted by the various conducted experiments. The data points represent the average experiment time for each denuder collection, with the black line span the collection time range (from start to stop). The model simulations include both the base model (USC-API) and an update to the NO_2 + OH nitrogen isotope fractionation factor ($^{15}\alpha = 0.997$) (USC-API-KIE) as opposed to the base model with $^{15}\alpha = 1.040$. For Exp. 6, a nighttime experiment, the $\delta^{15}N$ simulation using USC-API and USC-API-KIE were similar due to the limited role of the NO_2+OH reaction under those conditions.

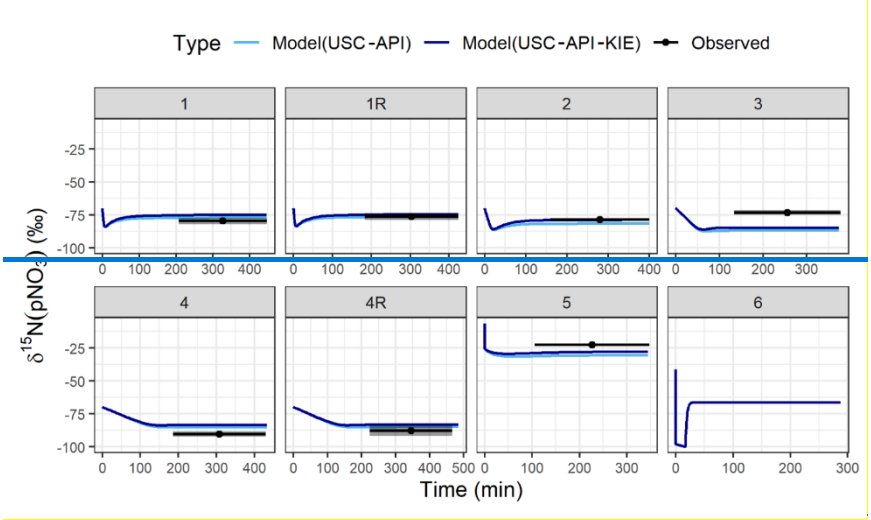

~~Fig. 10. Comparison between the modeled and observed $\delta^{15}N(pNO_3)$ values sorted by the various conducted experiments. The data points represent the average experiment time for each denuder collection, with the black line span the collection time range (from start to stop). The model simulations include both the base model (USC-API) and an update to the NO_2 + OH nitrogen isotope fractionation factor ($^{15}\alpha$ = 0.997) (USC-API-KIE) as opposed to the base model with $^{15}\alpha$ = 1.040. For Exp. 6, a nighttime experiment, the $\delta^{15}N$ simulation using USC-API and USC-API-KIE were similar due to the limited role of the NO_2+OH reaction under those conditions.~~

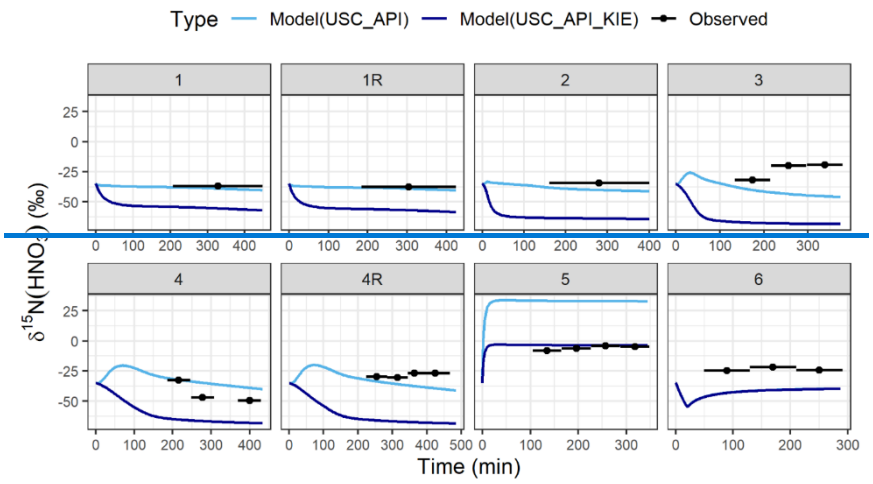

~~Fig. 11. Comparison between the modeled and observed $\delta^{15}N(HNO_3)$ values sorted by the various conducted experiments. The data points represent the average experiment time for each denuder collection, with the black line span the collection time range (from start to stop). The model simulations include both the base model (USC-API) and an update to the NO_2 + OH nitrogen isotope fractionation factor ($^{15}\alpha$ = 0.997) (USC-API-KIE) as opposed to the base model with $^{15}\alpha$ = 1.040. For Exp. 6, a nighttime experiment, the $\delta^{15}N$ simulation using USC-API and USC-API-KIE were similar due to the limited role of the NO_2+OH reaction under those conditions.~~

~~5~~5. Conclusion

This study presents the first chamber experiments combining comprehensive NO_y and α-pinene oxidation chemistry with stable isotope constraints. Using a suite of observations and box model simulations, we demonstrate how multi-isotope analyses of $\Delta^{17}O$, $\delta^{18}O$, and $\delta^{15}N$ can yield novel insights into atmospheric oxidation pathways, including the formation and transformation of gas-phase and pNO_3 species. We observed a strong linear relationship between $\Delta^{17}O$ and $\delta^{18}O$ values across all collected NO_y species. We derived a $\delta^{18}O$ value of 106 ± 5 ‰ for oxygen atoms transferred into NO_y from O_3^{term}, and a value of 11.1 ± 1.0 ‰ for oxygen atoms transferred from other oxidants with an assumed $\Delta^{17}O$ ~0 ‰, such as RO_2, HO_2, and OH. These results provide a new isotopic constraint for disentangling multi-oxidant systems in both chamber and ambient settings.

Nitrogen isotope fractionation was evaluated from the observations, which indicated $\Delta\delta^{15}N(HNO_3 - NO_2)$ values were generally enriched, while $\Delta\delta^{15}N(pNO_3 - NO_2)$ values were negative, reflecting preferential ^{15}N incorporation into HNO_3, and ^{14}N incorporation into pNO_3. However, large differences in the observed $\Delta\delta^{15}N(HNO_3 - NO_2)$ between H_2O_2/NO (33.7 ± 7.1 ‰) and HONO (0.4 ± 1.7 ‰) photochemical experiments remain unresolved, particularly since these experiments should have produced HNO_3 from a similar pathway, namely the NO_2 + OH reaction. These discrepancies make it challenging for us to recommend a fractionation value associated with the NO_2 + OH reaction and indicate the need for future targeted studies of the isotope effects during the NO_2 + OH reaction. Importantly, isotope observations revealed stark differences between HNO_3 (medium-high $\Delta^{17}O$ and high $\delta^{15}N$) and pNO_3 (low $\Delta^{17}O$ and low $\delta^{15}N$), with the later predominately derived from organic nitrate. These isotope differences between HNO_3 and organic nitrate could serve as a useful qualitative constraint to evaluate inorganic and organic nitrate contributions to HNO_3 and pNO_3 budgets.

Model simulations of $\Delta^{17}O$ were conducted and indicated our model captured $\Delta^{17}O(NO_2)$ and $\Delta^{17}O(ONIT)$ (compared with observed $\Delta^{17}O(pNO_3)$ values) well. Simulating $\Delta^{17}O(HNO_3)$, however, proved more challenging. The model tended to overestimate $\Delta^{17}O$ under high-NO_x conditions, underestimate it in low-NO_x experiments, and underpredict nighttime values. A series of sensitivity tests suggest this mismatch likely arises from multiple contributing factors, including potential HNO_3 measurement biases (e.g., chamber blank), missing heterogeneous pathways (e.g., N_2O_5 hydrolysis), and the need to revisit assumptions in the isotopic mass balance of the NO_2 + OH reaction. ~~This study provides a comprehensive investigation of NO_x and BVOC oxidation chemistry using stable isotope analyses and chemical modeling. Through $\Delta^{17}O$ and $\delta^{15}N$ observations compared to model simulation, we gained critical insights into $\Delta^{17}O$ transfer dynamics involved NO_x oxidation chemistry and nitrogen isotope fractionation. By adopting a $\Delta^{17}O$ value for O_3^{term} of 39 ‰, our model utilizing a recently developed $\Delta^{17}O$ transfer framework successfully reproduced $\Delta^{17}O$ values for NO_2 across diverse environmental conditions, affirming the robustness of the photochemical understanding of $\Delta^{17}O$ transfer dynamics. Furthermore, under the experimental conditions, we derived a $\delta^{18}O$ value of 106±5 ‰ for oxygen atoms transferred into NO_x from the O_3^{term}, and a value of 11.8±1.0 ‰ for oxygen atoms transferred from other oxidants, such as RO_2, HO_2, and OH. Moreover, we found that the recently developed I_NRACM model framework for simulating $\delta^{15}N$ was significantly improved by adopting a $^{15}\alpha$ = 0.997 for the NO_2+OH reaction, leading to better agreement with $\delta^{15}N(NO_2)$. This result highlights the importance of refining fractionation assumptions in isotope based chemical mechanisms. However, the updated fractionation factor introduced challenges in accurately simulating $\delta^{15}N$ values for HNO_3, highlighting persistent uncertainties in the sampling and modeling of HNO_3 under the experimental conditions.~~

From these experiments, it is evident that we have a solid understanding of oxygen isotope transfer associated with NO_x photochemical cycling, and the formation of organic nitrates. However, our understanding of the oxygen and nitrogen isotope dynamics of HNO_3 remains more uncertain. Our findings indicate the need for future experiments specifically designed to probe the formation pathways of HNO_3 and their associated isotope dynamics. This includes chamber studies that isolate individual pathways as well as targeted flow tube experiments. Such efforts are essential to refine oxygen isotope mass-balance

assumptions and are critical if $\Delta^{17}O$ and $\delta^{15}N$ is to be used quantitatively to track HNO_3 chemistry in both laboratory and ambient environments.

Our development of the USC-API mechanism marked a substantial advancement over existing frameworks such as RACM2 and MCM for describing NO_x and BVOC oxidation. This mechanism not only captured NO_x photochemical cycling and α-pinene decay dynamics but also provided accurate simulations of organic nitrate production. One of the major implications of this mechanism is that the weighted branching ratio of α-pinene+OH+NO leading to organic nitrate versus NO_2 production was set to 0.222 based on the MCM, which led to the correct photochemical dynamics involving NO_x, which was evaluated using $\Delta^{17}O$. The mechanism further clarified the roles of daytime α-pinene+OH+NO reactions versus nighttime α-pinene+NO_3 reactions contributing to organic nitrate production. Our model and result comparisons indicate instances where the α-pinene+NO_3+ HO_2 pathway significantly contributed to organic nitrate production during photochemical experiments. This nuanced understanding of organic nitrate formation has implications for atmospheric NO_x budgets and SOA production.

Isotope observations and model simulation revealed stark differences between HNO_3 (medium-high $\Delta^{17}O$ and high $\delta^{15}N$) and particulate nitrate (pNO_3; low $\Delta^{17}O$ and low $\delta^{15}N$), indicating distinct formation pathways. Our findings strongly suggest that pNO_3 in these experiments originated exclusively from organic nitrate, a conclusion supported by online AMS data. Furthermore, the $\Delta^{17}O$ and $\delta^{15}N$ evidence demonstrated that organic nitrate hydrolysis was not a major source of HNO_3 under the studied conditions, which predominantly involved low relative humidity. These insights offer new opportunities to probe pNO_3 hydrolysis and its implications for nitrate chemistry under varying environmental conditions. Despite these advances, limitations in accurately modeling $\Delta^{17}O$ and $\delta^{15}N$ values for HNO_3 highlighting the need for improved collection methodologies. Experimental artifacts, potentially linked to the use of long sampling lines and HNO_3 losses in chamber experiments, may have biased the collected data. These methodological challenges indicate the importance of refining sampling techniques for HNO_3 in chamber experiments to ensure representative measurements in future studies.

The implications of this work extend beyond the laboratory setting. Stable isotope techniques demonstrated their potential as powerful tools for probing complex NO_x and BVOC interactions and atmospheric oxidation chemistry. Future research should aim to expand these methodologies to other BVOC systems under a wider array of conditions, including variations in relative humidity, aerosol seed composition, and oxidant availability. Furthermore, integrating isotope techniques into field campaigns could provide invaluable constraints on NO_x oxidation and organic nitrate formation processes in real-world atmospheric environments. Overall, this study not only advances our understanding of the oxygen and nitrogen stable isotope dynamics involved in NO_x oxidation chemistry, but also provide insights into NO_x and BVOC chemistry. Addressing the limitations identified here and applying these techniques across broader contexts will enhance the predictive power of atmospheric chemistry models, aiding in the development of more effective air quality management strategies and climate policies.

Code and Data availability. The box model simulations, including model mechanisms, input files, and output files have been made publicly available at: 10.5281/zenodo.15615851~~https://zenodo.org/records/14241585~~. The experimental data and figure ~~codes~~ scripts have been made publicly available at: ~~–~~10.5281/zenodo.15616525~~https://zenodo.org/records/14241591~~. The chemical mechanism and isotope data are provided in the Supplementary Material.

Author contributions. WWW, MT, NLN, MGH designed the conducted experiments. WWW, MT, DEB, GE, PT, WX, JR, FL, GH, JBM conducted the experiments. WWW and DEB conducted the offline data analysis. WWW conducted the chamber simulations with input from MGH, MT and NLN. WWW wrote the manuscript with input from all authors. WWW and MGH secured funding.

Competing interests. The contact author has declared that none of the authors has any competing interests.

Acknowledgements. We thank Ruby Ho for laboratory assistance.

Financial Support. This research has been supported by NOAA's Climate Program Office's Atmospheric Chemistry, Carbon Cycle, and Climate Program (NOAA AC4 NA18OAR4310118).

References

Albertin, S., Savarino, J., Bekki, S., Barbero, A., and Caillon, N.: Measurement report: Nitrogen isotopes ($\delta^{15}N$) and first quantification of oxygen isotope anomalies ($\Delta^{17}O$, $\delta^{18}O$) in atmospheric nitrogen dioxide, Atmospheric Chemistry and Physics, 21, 10477–10497, https://doi.org/10.5194/acp-21-10477-2021, 2021.

Alexander, B., Sherwen, T., Holmes, C. D., Fisher, J. A., Chen, Q., Evans, M. J., and Kasibhatla, P.: Global inorganic nitrate production mechanisms: comparison of a global model with nitrate isotope observations, Atmospheric Chemistry and Physics, 20, 3859–3877, https://doi.org/10.5194/acp-20-3859-2020, 2020.

Bahreini, R., Ervens, B., Middlebrook, A. M., Warneke, C., de Gouw, J. A., DeCarlo, P. F., Jimenez, J. L., Brock, C. A., Neuman, J. A., Ryerson, T. B., Stark, H., Atlas, E., Brioude, J., Fried, A., Holloway, J. S., Peischl, J., Richter, D., Walega, J., Weibring, P., Wollny, A. G., and Fehsenfeld, F. C.: Organic aerosol formation in urban and industrial plumes near Houston and Dallas, Texas, Journal of Geophysical Research: Atmospheres, 114, https://doi.org/10.1029/2008JD011493, 2009.

Bates, K. H., Burke, G. J., Cope, J. D., and Nguyen, T. B.: Secondary organic aerosol and organic nitrogen yields from the nitrate radical (NO_3) oxidation of alpha-pinene from various RO_2 fates, Atmospheric Chemistry and Physics, 22, 1467–1482, https://doi.org/10.5194/acp-22-1467-2022, 2022.

Beaver, M. R., Clair, J. S., Paulot, F., Spencer, K. M., Crounse, J. D., LaFranchi, B. W., Min, K. E., Pusede, S. E., Wooldridge, P. J., and Schade, G. W.: Importance of biogenic precursors to the budget of organic nitrates: observations of multifunctional organic nitrates by CIMS and TD-LIF during BEARPEX 2009, Atmospheric Chemistry and Physics, 12, 5773–5785, https://doi.org/10.5194/acp-12-5773-2012, 2012.

Bekker, C., Walters, W. W., Murray, L. T., and Hastings, M. G.: Nitrate chemistry in the northeast US – Part 1: Nitrogen isotope seasonality tracks nitrate formation chemistry, Atmospheric Chemistry and Physics, 23, 4185–4201, https://doi.org/10.5194/acp-23-4185-2023, 2023.

Berhanu, T. A., Savarino, J., Bhattacharya, S. K., and Vicars, W. C.: 17O excess transfer during the $NO_2 + O_3 \rightarrow NO_3 + O_2$ reaction, The Journal of Chemical Physics, 136, 044311, https://doi.org/10.1063/1.3666852, 2012.

Blum, D. E., Walters, W. W., and Hastings, M. G.: Speciated Collection of Nitric Acid and Fine Particulate Nitrate for Nitrogen and Oxygen Stable Isotope Determination, Anal. Chem., 92, 16079–16088, https://doi.org/10.1021/acs.analchem.0c03696, 2020.

Blum, D. E., Walters, W. W., Eris, G., Takeuchi, M., Huey, L. G., Tanner, D., Xu, W., Rivera-Rios, J. C., Liu, F., Ng, N. L., and Hastings, M. G.: Collection of Nitrogen Dioxide for Nitrogen and Oxygen Isotope Determination─Laboratory and Environmental Chamber Evaluation, Anal. Chem., 95, 3371–3378, https://doi.org/10.1021/acs.analchem.2c04672, 2023.

Böhlke, J. K., Mroczkowski, S. J., and Coplen, T. B.: Oxygen isotopes in nitrate: New reference materials for ^{18}O: ^{17}O: ^{16}O measurements and observations on nitrate-water equilibration, Rapid Communications in Mass Spectrometry, 17, 1835–1846, https://doi.org/10.1002/rcm.1123, 2003.

Böhlke, J. K., Smith, R. L., and Hannon, J. E.: Isotopic analysis of N and O in nitrite and nitrate by sequential selective bacterial reduction to N_2O, Analytical chemistry, 79, 5888–5895, https://doi.org/10.1021/ac070176k, 2007.

Boyd, C. M., Sanchez, J., Xu, L., Eugene, A. J., Nah, T., Tuet, W. Y., Guzman, M. I., and Ng, N. L.: Secondary organic aerosol formation from the β-pinene+ NO_3 system: effect of humidity and peroxy radical fate, Atmospheric Chemistry and Physics, 15, 7497–7522, https://doi.org/10.5194/acp-15-7497-2015, 2015.

Browne, E. C. and Cohen, R. C.: Effects of biogenic nitrate chemistry on the NO_x lifetime in remote continental regions, Atmospheric Chemistry and Physics, 12, 11917–11932, https://doi.org/10.5194/acp-12-11917-2012, 2012.

Browne, E. C., Wooldridge, P. J., Min, K.-E., and Cohen, R. C.: On the role of monoterpene chemistry in the remote continental boundary layer, Atmospheric Chemistry and Physics, 14, 1225–1238, https://doi.org/10.5194/acp-14-1225-2014, 2014.

Casciotti, K. L., Sigman, D. M., Hastings, M. G., Böhlke, J. K., and Hilkert, A.: Measurement of the oxygen isotopic composition of nitrate in seawater and freshwater using the denitrifier method, Analytical Chemistry, 74, 4905–4912, https://doi.org/10.1021/ac020113w, 2002.

Chai, J. and Hastings, M. G.: Collection Method for Isotopic Analysis of Gaseous Nitrous Acid, Anal. Chem., 90, 830–838, https://doi.org/10.1021/acs.analchem.7b03561, 2018.

Craig, H.: Isotopic standards for carbon and oxygen and correction factors for mass-spectrometric analysis of carbon dioxide, Geochimica et Cosmochimica Acta, 12, 133–149, https://doi.org/10.1016/0016-7037(57)90024-8, 1957.

DeCarlo, P. F., Kimmel, J. R., Trimborn, A., Northway, M. J., Jayne, J. T., Aiken, A. C., Gonin, M., Fuhrer, K., Horvath, T., and Docherty, K. S.: Field-deployable, high-resolution, time-of-flight aerosol mass spectrometer, Analytical chemistry, 78, 8281–8289, https://doi.org/10.1021/ac061249n, 2006.

Donahue, N. M., Mohrschladt, R., Dransfield, T. J., Anderson, J. G., and Dubey, M. K.: Constraining the Mechanism of OH + NO_2 Using Isotopically Labeled Reactants: Experimental Evidence for HOONO Formation, The Journal of Physical Chemistry A, 105, 1515–1520, https://doi.org/10.1021/jp0035582, 2001.

Dubey, M. K., Mohrschladt, R., Donahue, N. M., and Anderson, J. G.: Isotope specific kinetics of hydroxyl radical (OH) with water (H_2O): Testing models of reactivity and atmospheric fractionation, The Journal of Physical Chemistry A, 101, 1494–1500, https://doi.org/10.1021/jp962332p, 1997.

Elliott, E. M., Yu, Z., Cole, A. S., and Coughlin, J. G.: Isotopic advances in understanding reactive nitrogen deposition and atmospheric processing, Science of The Total Environment, 662, 393–403, https://doi.org/10.1016/j.scitotenv.2018.12.177, 2019.

Escorcia, E. N., Sjostedt, S. J., and Abbatt, J. P. D.: Kinetics of N2O5 Hydrolysis on Secondary Organic Aerosol and Mixed Ammonium Bisulfate−Secondary Organic Aerosol Particles, J. Phys. Chem. A, 114, 13113–13121, https://doi.org/10.1021/jp107721v, 2010.

Fang, H., Walters, W. W., Mase, D., and Michalski, G.: i_NRACM: incorporating ^{15}N into the Regional Atmospheric Chemistry Mechanism (RACM) for assessing the role photochemistry plays in controlling the isotopic composition of NO_x, NO_y, and atmospheric nitrate, Geoscientific Model Development, 14, 5001–5022, https://doi.org/10.5194/gmd-14-5001-2021, 2021.

Farmer, D. K., Matsunaga, A., Docherty, K. S., Surratt, J. D., Seinfeld, J. H., Ziemann, P. J., and Jimenez, J. L.: Response of an aerosol mass spectrometer to organonitrates and organosulfates and implications for atmospheric chemistry, Proceedings of the National Academy of Sciences, 107, 6670–6675, https://doi.org/10.1073/pnas.0912340107, 2010.

Fibiger, D. L., Hastings, M. G., Lew, A. F., and Peltier, R. E.: Collection of NO and NO_2 for Isotopic Analysis of NO_x Emissions, Analytical Chemistry, 86, 12115–12121, https://doi.org/10.1021/ac502968e, 2014.

Fisher, J. A., Jacob, D. J., Travis, K. R., Kim, P. S., Marais, E. A., Chan Miller, C., Yu, K., Zhu, L., Yantosca, R. M., Sulprizio, M. P., and others: Organic nitrate chemistry and its implications for nitrogen budgets in an isoprene-and monoterpene-rich atmosphere: constraints from aircraft (SEAC4 RS) and ground-based (SOAS) observations in the Southeast US, Atmospheric Chemistry and Physics, 16, 5969–5991, https://doi.org/10.5194/acp-16-5969-2016, 2016.

Freyer, H. D., Kley, D., Volz-Thomas, A., and Kobel, K.: On the interaction of isotopic exchange processes with photochemical reactions in atmospheric oxides of nitrogen, Journal of Geophysical Research, 98, 14791–14796, https://doi.org/10.1029/93JD00874, 1993.

Fry, J. L., Kiendler-Scharr, A., Rollins, A. W., Wooldridge, P. J., Brown, S. S., Fuchs, H., Dubé, W., Mensah, A., Dal Maso, M., and Tillmann, R.: Organic nitrate and secondary organic aerosol yield from NO_3 oxidation of β-pinene evaluated using a gas-phase kinetics/aerosol partitioning model, Atmospheric Chemistry and Physics, 9, 1431–1449, https://doi.org/10.5194/acp-9-1431-2009, 2009.

Goliff, W. S., Stockwell, W. R., and Lawson, C. V.: The regional atmospheric chemistry mechanism, version 2, Atmospheric Environment, 68, 174–185, https://doi.org/10.1016/j.atmosenv.2012.11.038, 2013.

Guo, H., Sullivan, A. P., Campuzano-Jost, P., Schroder, J. C., Lopez-Hilfiker, F. D., Dibb, J. E., Jimenez, J. L., Thornton, J. A., Brown, S. S., Nenes, A., and Weber, R. J.: Fine particle pH and the partitioning of nitric acid during winter in the northeastern United States, Journal of Geophysical Research: Atmospheres, 121, 10,355-10,376, https://doi.org/10.1002/2016JD025311, 2016.

Hastings, M. G., Sigman, D. M., and Lipschultz, F.: Isotopic evidence for source changes of nitrate in rain at Bermuda, Journal of Geophysical Research: Atmospheres, 108, https://doi.org/10.1029/2003JD003789, 2003.

Hastings, M. G., Casciotti, K. L., and Elliott, E. M.: Stable isotopes as tracers of anthropogenic nitrogen sources, deposition, and impacts, Elements, 9, 339–344, https://doi.org/10.2113/gselements.9.5.339, 2013.

Hoyle, C. R., Boy, M., Donahue, N. M., Fry, J. L., Glasius, M., Guenther, A., Hallar, A. G., Huff Hartz, K., Petters, M. D., and Petäjä, T.: A review of the anthropogenic influence on biogenic secondary organic aerosol, Atmospheric Chemistry and Physics, 11, 321–343, https://doi.org/10.5194/acp-11-321-2011, 2011.

Huey, L. G., Dunlea, E. J., Lovejoy, E. R., Hanson, D. R., Norton, R. B., Fehsenfeld, F. C., and Howard, C. J.: Fast time response measurements of HNO_3 in air with a chemical ionization mass spectrometer, Journal of Geophysical Research: Atmospheres, 103, 3355–3360, https://doi.org/10.1029/97JD02214, 1998.

Ishino, S., Hattori, S., Savarino, J., Jourdain, B., Preunkert, S., Legrand, M., Caillon, N., Barbero, A., Kuribayashi, K., and Yoshida, N.: Seasonal variations of triple oxygen isotopic compositions of atmospheric sulfate, nitrate, and ozone at Dumont d'Urville, coastal Antarctica, Atmos. Chem. Phys., 17, 3713–3727, https://doi.org/10.5194/acp-17-3713-2017, 2017.

Jenkin, M. E., Saunders, S. M., and Pilling, M. J.: The tropospheric degradation of volatile organic compounds: a protocol for mechanism development, Atmospheric Environment, 31, 81–104, https://doi.org/10.1016/S1352-2310(96)00105-7, 1997.

Kaiser, J., Hastings, M. G., Houlton, B. Z., Röckmann, T., and Sigman, D. M.: Triple Oxygen Isotope Analysis of Nitrate Using the Denitrifier Method and Thermal Decomposition of N_2O, Anal. Chem., 79, 599–607, https://doi.org/10.1021/ac061022s, 2007.

Kiendler-Scharr, A., Mensah, A. A., Friese, E., Topping, D., Nemitz, E., Prévôt, A. S., Äijälä, M., Allan, J., Canonaco, F., and Canagaratna, M.: Ubiquity of organic nitrates from nighttime chemistry in the European submicron aerosol, Geophysical research letters, 43, 7735–7744, https://doi.org/10.1002/2016GL069239, 2016.

Kim, H., Walters, W. W., Bekker, C., Murray, L. T., and Hastings, M. G.: Nitrate Chemistry in the Northeast US Part II: Oxygen Isotopes Reveal Differences in Particulate and Gas Phase Formation, Atmospheric Chemistry and Physics Discussions, 2022, 1–33, https://doi.org/10.5194/acp-2022-622, 2022.

Kroll, J. H., Ng, N. L., Murphy, S. M., Flagan, R. C., and Seinfeld, J. H.: Secondary organic aerosol formation from isoprene photooxidation under high-NO_x conditions, Geophysical Research Letters, 32, https://doi.org/10.1021/es0524301, 2005.

Li, J., Zhang, X., Orlando, J., Tyndall, G., and Michalski, G.: Quantifying the nitrogen isotope effects during photochemical equilibrium between NO and NO_2: implications for $\delta^{15}N$ in tropospheric reactive nitrogen, Atmospheric Chemistry and Physics, 20, 9805–9819, https://doi.org/10.5194/acp-20-9805-2020, 2020.

Li, J., Davy, P., Harvey, M., Katzman, T., Mitchell, T., and Michalski, G.: Nitrogen isotopes in nitrate aerosols collected in the remote marine boundary layer: Implications for nitrogen isotopic fractionations among atmospheric reactive nitrogen species, Atmospheric Environment, 245, 118028, https://doi.org/10.1016/j.atmosenv.2020.118028, 2021.

Lopez-Hilfiker, F. D., Mohr, C., Ehn, M., Rubach, F., Kleist, E., Wildt, J., Mentel, T. F., Lutz, A., Hallquist, M., and Worsnop, D.: A novel method for online analysis of gas and particle composition: description and evaluation of a Filter Inlet for Gases and AEROsols (FIGAERO), Atmospheric Measurement Techniques, 7, 983–1001, https://doi.org/10.5194/amt-7-983-2014, 2014.

Lyons, J. R.: Transfer of mass-independent fractionation in ozone to other oxygen-containing radicals in the atmosphere, Geophysical Research Letters, 28, 3231–3234, https://doi.org/10.1029/2000GL012791, 2001.

McIlvin, M. R. and Altabet, M. A.: Chemical Conversion of Nitrate and Nitrite to Nitrous Oxide for Nitrogen and Oxygen Isotopic Analysis in Freshwater and Seawater, Anal. Chem., 77, 5589–5595, https://doi.org/10.1021/ac050528s, 2005.

Michalski, G., Scott, Z., Kabiling, M., and Thiemens, M. H.: First measurements and modeling of $\Delta^{17}O$ in atmospheric nitrate, Geophys. Res. Lett., 30, 1870, https://doi.org/10.1029/2003GL017015, 2003.

Michalski, G., Bhattacharya, S. K., and Mase, D. F.: Oxygen isotope dynamics of atmospheric nitrate and its precursor molecules, in: Handbook of environmental isotope geochemistry, Springer, New York, 613–635, 2012.

Michalski, G., Bhattacharya, S. K., and Girsch, G.: NOx cycle and the tropospheric ozone isotope anomaly: an experimental investigation, Atmospheric Chemistry and Physics, 14, 4935–4953, https://doi.org/10.5194/acp-14-4935-2014, 2014.

Morales, A. C., Jayarathne, T., Slade, J. H., Laskin, A., and Shepson, P. B.: The production and hydrolysis of organic nitrates from OH radical oxidation of β-ocimene, Atmospheric Chemistry and Physics, 21, 129–145, https://doi.org/10.5194/acp-21-129-2021, 2021.

Morin, S., Sander, R., and Savarino, J.: Simulation of the diurnal variations of the oxygen isotope anomaly (Δ^{17}O) of reactive atmospheric species, Atmospheric Chemistry and Physics, 11, 3653–3671, https://doi.org/10.5194/acp-11-3653-2011, 2011.

Nah, T., Sanchez, J., Boyd, C. M., and Ng, N. L.: Photochemical Aging of α-pinene and β-pinene Secondary Organic Aerosol formed from Nitrate Radical Oxidation, Environ. Sci. Technol., 50, 222–231, https://doi.org/10.1021/acs.est.5b04594, 2016.

Ng, N. L., Brown, S. S., Archibald, A. T., Atlas, E., Cohen, R. C., Crowley, J. N., Day, D. A., Donahue, N. M., Fry, J. L., Fuchs, H., Griffin, R. J., Guzman, M. I., Herrmann, H., Hodzic, A., Iinuma, Y., Jimenez, J. L., Kiendler-Scharr, A., Lee, B. H., Luecken, D. J., Mao, J., McLaren, R., Mutzel, A., Osthoff, H. D., Ouyang, B., Picquet-Varrault, B., Platt, U., Pye, H. O. T., Rudich, Y., Schwantes, R. H., Shiraiwa, M., Stutz, J., Thornton, J. A., Tilgner, A., Williams, B. J., and Zaveri, R. A.: Nitrate radicals and biogenic volatile organic compounds: oxidation, mechanisms, and organic aerosol, Atmos. Chem. Phys., 17, 2103–2162, https://doi.org/10.5194/acp-17-2103-2017, 2017.

Orsini, D. A., Ma, Y., Sullivan, A., Sierau, B., Baumann, K., and Weber, R. J.: Refinements to the particle-into-liquid sampler (PILS) for ground and airborne measurements of water soluble aerosol composition, Atmospheric Environment, 37, 1243–1259, https://doi.org/10.1016/S1352-2310(02)01015-4, 2003.

Rindelaub, J. D., McAvey, K. M., and Shepson, P. B.: The photochemical production of organic nitrates from α-pinene and loss via acid-dependent particle phase hydrolysis, Atmospheric Environment, 100, 193–201, http://dx.doi.org/10.1016/j.atmosenv.2014.11.010, 2015.

Rindelaub, J. D., Borca, C. H., Hostetler, M. A., Slade, J. H., Lipton, M. A., Slipchenko, L. V., and Shepson, P. B.: The acid-catalyzed hydrolysis of an α-pinene-derived organic nitrate: kinetics, products, reaction mechanisms, and atmospheric impact, Atmospheric Chemistry and Physics, 16, 15425–15432, https://doi.org/10.5194/acp-16-15425-2016, 2016.

Romer, P. S., Duffey, K. C., Wooldridge, P. J., Allen, H. M., Ayres, B. R., Brown, S. S., Brune, W. H., Crounse, J. D., De Gouw, J., and Draper, D. C.: The lifetime of nitrogen oxides in an isoprene-dominated forest, Atmospheric Chemistry and Physics, 16, 7623–7637, https://doi.org/10.5194/acp-16-7623-2016, 2016.

Sato, K., Ikemori, F., Ramasamy, S., Iijima, A., Kumagai, K., Fushimi, A., Fujitani, Y., Chatani, S., Tanabe, K., and Takami, A.: Formation of secondary organic aerosol tracers from anthropogenic and biogenic volatile organic compounds under varied NO_x and oxidant conditions, Atmospheric Environment: X, 14, 100169, https://doi.org/10.1016/j.aeaoa.2022.100169, 2022.

Saunders, S. M., Jenkin, M. E., Derwent, R. G., and Pilling, M. J.: Protocol for the development of the Master Chemical Mechanism, MCM v3 (Part A): tropospheric degradation of non-aromatic volatile organic compounds, Atmospheric Chemistry and Physics, 3, 161–180, https://doi.org/10.5194/acp-3-161-2003, 2003.

Savarino, J., Bhattacharya, S. K., Morin, S., Baroni, M., and Doussin, J.-F.: The NO+ O_3 reaction: A triple oxygen isotope perspective on the reaction dynamics and atmospheric implications for the transfer of the ozone isotope anomaly, The Journal of chemical physics, 128, 194303, https://doi.org/10.1063/1.2917581, 2008.

Savarino, J., Morin, S., Erbland, J., Grannec, F., Patey, M. D., Vicars, W., Alexander, B., and Achterberg, E. P.: Isotopic composition of atmospheric nitrate in a tropical marine boundary layer, PNAS, 110, 17668–17673, https://doi.org/10.1073/pnas.1216639110, 2013.

Sharp, Z.: Principles of Stable Isotope Geochemistry, 2nd Edition, Open Textbooks, https://doi.org/ https://doi.org/10.25844/h9q1-0p82 , 2017.

Sigman, D. M., Casciotti, K. L., Andreani, M., Barford, C., Galanter, M., and Böhlke, J. K.: A bacterial method for the nitrogen isotopic analysis of nitrate in seawater and freshwater, Analytical chemistry, 73, 4145–4153, https://doi.org/10.1021/ac010088e, 2001.

Takeuchi, M. and Ng, N. L.: Chemical composition and hydrolysis of organic nitrate aerosol formed from hydroxyl and nitrate radical oxidation of α-pinene and β-pinene, Atmospheric Chemistry and Physics, 19, 12749–12766, https://doi.org/10.5194/acp-19-12749-2019, 2019.

Takeuchi, M., Berkemeier, T., Eris, G., and Ng, N. L.: Non-linear effects of secondary organic aerosol formation and properties in multi-precursor systems, Nat Commun, 13, 7883, https://doi.org/10.1038/s41467-022-35546-1, 2022.

Takeuchi, M., Wang ,Yuchen, Nault ,Benjamin A., Chen ,Yunle, Canagaratna, Manjula R., and and Ng, N. L.: Evaluating the response of the Aerodyne aerosol mass spectrometer to monoterpene- and isoprene-derived organic nitrate standards, Aerosol Science and Technology, 58, 1371–1388, https://doi.org/10.1080/02786826.2024.2389183, 2024.

Tuet, W. Y., Chen, Y., Xu, L., Fok, S., Gao, D., Weber, R. J., and Ng, N. L.: Chemical oxidative potential of secondary organic aerosol (SOA) generated from the photooxidation of biogenic and anthropogenic volatile organic compounds, Atmospheric Chemistry and Physics, 17, 839–853, https://doi.org/10.5194/acp-17-839-2017, 2017.

Vicars, W. C. and Savarino, J.: Quantitative constraints on the 17 O-excess (Δ^{17}O) signature of surface ozone: Ambient measurements from 50° N to 50° S using the nitrite-coated filter technique, Geochimica et Cosmochimica Acta, 135, 270–287, http://dx.doi.org/10.1016/j.gca.2014.03.023, 2014.

Walters, W. W. and Hastings, M. G.: Triple oxygen stable isotope analysis of nitrite measured using continuous flow isotope ratio mass spectrometry, MethodsX, 11, 102413, https://doi.org/10.1016/j.mex.2023.102413, 2023.

Walters, W. W. and Michalski, G.: Theoretical calculation of nitrogen isotope equilibrium exchange fractionation factors for various NO_y molecules, Geochimica et Cosmochimica Acta, 164, 284–297, https://doi.org/10.1016/j.gca.2015.05.029, 2015.

Walters, W. W. and Michalski, G.: Ab initio study of nitrogen and position-specific oxygen kinetic isotope effects in the NO + O_3 reaction, The Journal of Chemical Physics, 145, 224311, https://doi.org/10.1063/1.4968562, 2016a.

Walters, W. W. and Michalski, G.: Theoretical calculation of oxygen equilibrium isotope fractionation factors involving various NO_y molecules, OH, and H_2O and its implications for isotope variations in atmospheric nitrate, Geochimica et Cosmochimica Acta, 191, 89–101, https://doi.org/10.1016/j.gca.2016.06.039, 2016b.

Walters, W. W., Simonini, D. S., and Michalski, G.: Nitrogen isotope exchange between NO and NO_2 and its implications for $\delta^{15}N$ variations in tropospheric NO_x and atmospheric nitrate, Geophys. Res. Lett., 43, 2015GL066438, https://doi.org/10.1002/2015GL066438, 2016.

Walters, W. W., Fang, H., and Michalski, G.: Summertime diurnal variations in the isotopic composition of atmospheric nitrogen dioxide at a small midwestern United States city, Atmospheric Environment, 179, 1–11, https://doi.org/10.1016/j.atmosenv.2018.01.047, 2018.

Walters, W. W., Takeuchi, M., Ng, N. L., and Hastings, M. G.: Incorporating Oxygen Isotopes of Oxidized Reactive Nitrogen in the Regional Atmospheric Chemistry Mechanism, version 2 (ICOIN-RACM2), Geoscientific Model Development, 17, 4673–4687, https://doi.org/10.5194/gmd-17-4673-2024, 2024a.

Walters, W. W., Pye, H. O. T., Kim, H., and Hastings, M. G.: Modeling the Oxygen Isotope Anomaly ($\Delta^{17}O$) of Reactive Nitrogen in the Community Multiscale Air Quality Model: Insights into Nitrogen Oxide Chemistry in the Northeastern United States, ACS EST Air, https://doi.org/10.1021/acsestair.3c00056, 2024b.

Wang, X., Liu, T., Bernard, F., Ding, X., Wen, S., Zhang, Y., Zhang, Z., He, Q., Lü, S., and Chen, J.: Design and characterization of a smog chamber for studying gas-phase chemical mechanisms and aerosol formation, Atmospheric Measurement Techniques, 7, 301–313, https://doi.org/10.5194/amt-7-301-2014, 2014.

Wang, Y., Piletic, I., Takeuchi, M., Xu, T., France, S., and Ng, N. L.: Synthesis and hydrolysis of atmospherically relevant monoterpene-derived organic nitrates, Environ Sci Technol, 55, 14595–14606, https://doi.org/10.1021/acs.est.1c05310, 2021.

Wang, Y., Takeuchi, M., Wang, S., Nizkorodov, S. A., France, S., Eris, G., and Ng, N. L.: Photolysis of Gas-Phase Atmospherically Relevant Monoterpene-Derived Organic Nitrates, J. Phys. Chem. A, 127, 987–999, https://doi.org/10.1021/acs.jpca.2c04307, 2023.

Wolfe, G. M., Marvin, M. R., Roberts, S. J., Travis, K. R., and Liao, J.: The Framework for 0-D Atmospheric Modeling (F0AM) v3.1, Geoscientific Model Development, 9, 3309–3319, https://doi.org/10.5194/gmd-9-3309-2016, 2016.

Xu, L., Suresh, S., Guo, H., Weber, R. J., and Ng, N. L.: Aerosol characterization over the southeastern United States using high-resolution aerosol mass spectrometry: spatial and seasonal variation of aerosol composition and sources with a focus on organic nitrates, Atmospheric Chemistry and Physics, 15, 7307–7336, https://doi.org/10.5194/acp-15-7307-2015, 2015a.

Xu, L., Guo, H., Boyd, C. M., Klein, M., Bougiatioti, A., Cerully, K. M., Hite, J. R., Isaacman-VanWertz, G., Kreisberg, N. M., Knote, C., and others: Effects of anthropogenic emissions on aerosol formation from isoprene and monoterpenes in the southeastern United States (vol 112, pg 37, 2015), PROCEEDINGS OF THE NATIONAL ACADEMY OF SCIENCES OF THE UNITED STATES OF AMERICA, 112, E4509–E4509, https://doi.org/10.1073/pnas.1417609112, 2015b.

Xu, L., Tsona, N. T., You, B., Zhang, Y., Wang, S., Yang, Z., Xue, L., and Du, L.: NO_x enhances secondary organic aerosol formation from nighttime γ-terpinene ozonolysis, Atmospheric Environment, 225, 117375, https://doi.org/10.1016/j.atmosenv.2020.1173752020.

Young, E. D., Galy, A., and Nagahara, H.: Kinetic and equilibrium mass-dependent isotope fractionation laws in nature and their geochemical and cosmochemical significance, Geochimica et Cosmochimica Acta, 66, 1095–1104, https://doi.org/10.1016/S0016-7037(01)00832-8, 2002.

Zare, A., Romer, P. S., Nguyen, T., Keutsch, F. N., Skog, K., and Cohen, R. C.: A comprehensive organic nitrate chemistry: insights into the lifetime of atmospheric organic nitrates, Atmospheric Chemistry and Physics, 18, 15419–15436, https://doi.org/10.5194/acp-18-15419-2018, 2018.